# Design of efficient magnetocaloric materials for energy conversion

You, X.

**DOI**
[10.4233/uuid:49700510-47b3-4450-85da-c99b4d14878f](10.4233/uuid:49700510-47b3-4450-85da-c99b4d14878f)

**Publication date**
2020

**Document Version**
Final published version

**Important note**
To cite this publication, please use the final published version (if applicable).
Please check the document version above.

# Design of efficient Magnetocaloric materials for energy conversion

**Xinmin You**

尤欣敏

**TU**Delft

# DESIGN OF EFFICIENT MAGNETOCALORIC MATERIALS FOR ENERGY CONVERSION

# DESIGN OF EFFICIENT MAGNETOCALORIC MATERIALS FOR ENERGY CONVERSION

## Proefschrift

ter verkrijging van de graad van doctor
aan de Technische Universiteit Delft,
op gezag van de Rector Magnificus Prof. dr. ir. T. H. J. J. van der Hagen;
voorzitter van het College voor Promoties,
in het openbaar te verdedigen op
woensdag 11 November 2020 om 15.00 uur

door

## Xinmin YOU

Master of Materials Science and Engineering,
Nanjing Tech University, Nanjing, China
geboren te Nanjing, China

Dit proefschrift is goedgekeurd door de promotoren.
  Prof. dr. E. H. Brück en Dr. ir. N. H. van Dijk

Samenstelling promotiecommissie:
  Rector magnificus,                     voorzitter

  Prof. dr. E. H. Brück            Technische Universiteit Delft, promotor
  Dr. ir. N. H. van Dijk           Technische Universiteit Delft, promotor

  *Onafhankelijke leden:*
  Prof. dr. Bernard Dam            Technische Universiteit Delft
  Prof. dr. Pieter Dorenbos        Technische Universiteit Delft
  Dr. Carlos Infante Ferreira      Technische Universiteit Delft
  Prof. dr. ir. Theo van der Meer  Universiteit Twente
  Prof. dr. Jack Zhao              Jiangsu Provincial Hydrogen Fuel Cell R&D
                                   Center, China

*Dedicated to my family*

献给我的家人

# CONTENTS

# 7. Ball milling synthesis of magnetocaloric Ni-Mn-Sn Heusler compounds   87

# 8. Conclusion and Recommendations   97

# SUMMARY

The magnetocaloric effect (MCE) is a magneto-thermodynamic phenomenon in which a temperature change of a material is caused by exposing the material to a changing magnetic field under adiabatic conditions. There are two main applications based on the MCE. One application is magnetic refrigeration, which can expel heat in a magnetic field cycle. Another application is magnetic energy conversion in thermomagnetic motors/generators, which can transfer waste heat into kinetic/electric energy.

Gadolinium metal is the standard reference material for the application of the MCE. However, it has a limited MCE with a second-order magnetic transition. Several intermetallic material systems with first-order magnetic transition resulting in a giant MCE have been discovered, including $La(Fe,Si)_{13}$ based alloys, MnFeP(As, Ge, Si) alloys and Ni-Mn-based Heusler alloys.

To design a magnetocaloric material that is suitable for applications, first of all, requires an estimated recipe, which can be obtained from the phase diagram. Secondly, an appropriate synthesis route should be chosen. Thirdly, the stoichiometry of the material should be optimised to avoid impurity phases. For the energy conversion applications, the desired material should preferentially be in the vicinity of the border between a first-order magnetic phase transition (FOMT) and a second-order magnetic phase transition (SOMT). If it is a FOMT or SOMT, the formula can be adjusted by changing the heat treatment, the element ratios and introducing new elements, until the transition is close to the critical point (CP). Finally, the transition temperature needs to be checked to see it is in the designed working temperature range. If not, the recipe needs to be adjusted until an optimised material is found.

Experimental diagrams of the ferromagnetic transition temperature ($T_C$) and the thermal hysteresis as a function of composition were constructed in the $(Mn,Fe)_2(P,Si)$ system as a guide to estimate suitable compositions for applications. The structure change across the magnetic phase transition is coupled with the thermal hysteresis of the magnetic transition in the experimental diagram. Both Mn-rich samples and Fe-rich samples with a low Si concentration were found to show a low hysteresis that can form promising candidates for applications in a thermomagnetic motor.

The effect of V substitution for Fe is investigating in the $Mn_{0.7}Fe_{x-z}V_zP_{0.6}Si_{0.4}$ alloys. The $(Mn,Fe)_{1.91}(P,Si)$ stoichiometry was chosen as a starting point to obtain the smallest impurity content. For an increasing V content the $a$ axis expands and the $c$ axis shrinks (together with the $c/a$ ratio), whereas the unit-cell volume remains about constant. The ferromagnetic transition temperature $T_C$ decreases with increasing V content. In the $Mn_{0.7}Fe_{1.18}V_{0.03}P_{0.6}Si_{0.4}$ compounds, 93% of saturation magnetisation at 5 K was reached in an applied magnetic field of 0.5 T, which makes this compound a promising candidate for low-field applications. The heat treatment clearly affects the amount of the impurity phase, and thereby the composition of the main phase. In this case, oven-cooled samples contain a larger impurity phase fraction than the quenched samples, which results in a lower transition temperature.

The currently applied methods to classify FOMT and SOMT materials were applied and compared using a series of samples $Mn_{1.3}Fe_{0.7}P_{1-y}Si_y$ ($y = 0.4$, 0.5 and 0.6). The FOMT samples are easy to categorise. Every criterion shows that $y = 0.4$ and 0.5 sample is FOMT materials. However, the SOMT and CP samples are problematic. In this thesis, different criteria were found to result in different conclusions for the $y = 0.6$ sample. From the latent heat, the $y = 0.6$ is predicted to undergo a FOMT. From the XRD data and the field dependence of $T_C$, the $y = 0.6$ sample is right on the CP. However, based on the Arrott plots, the gradual field dependence of the entropy change and the newly proposed field exponent $n$, the $y = 0.6$ sample is a SOMT material (but in close proximity to the CP).

The structural, magnetic and electronic properties of $LaFe_{11.8-b}Co_bSi_{1.2}$ ($b = 0.25$, 0.69 and 1.13) compounds are studied. With increasing Co content, the material is tuned from a FOMT towards a SOMT, $T_C$ increases, and the thermal hysteresis remains neglectable. In the unit cell, the most remarkable change in bond length is between the $8b$ and $96i$ sites and for one of the bonds between two neighbouring $96i$ sites. The negative thermal expansion across the transition correlates with the angle change in the orientation of the cage formed by the atoms on the $96i$ sites within the cubic unit cell. The experimental electron density maps reveal how the cage rotates within the cubic primitive cell. The samples with a smaller Co content show a larger change in the electron density compared to the sample with the highest Co content when $T_C$ is crossed.

The choice of synthesis method plays an important role in the physical properties of the prepared materials. For lab-scale samples, the most common way to synthesise $(Mn,Fe)_2(P,Si)$ compounds is ball milling. For Ni-Mn based Heusler

alloys, the most common synthesis route is arc-melting. In this thesis, ball milling was applied to synthesise Ni-Mn based Heusler alloys. The advantage of ball milling is that the annealing time can be shortened. Based on the optimised sample fabrication, the maximum magnetisation can be tuned by adjusting the Ni/Mn and Mn/Sn ratios. Introducing small amounts of cobalt and aluminium leads to a significant increase in the magnetisation.

# SAMENVATTING

Het magnetocalorisch effect (MCE) is een magnetisch-thermodynamisch fenomeen, waarbij een temperatuurverandering van een materiaal wordt veroorzaakt door het materiaal bloot te stellen aan een veranderend magneetveld onder adiabatische condities. Er zijn twee hoofdtoepassingen die gebaseerd zijn op het MCE. Eén toepassing is magnetisch koelen, waarbij warmte kan worden afgevoerd in een cyclisch proces waarin het magnetische veld wordt gevarieerd. Een andere toepassing is magnetische energieconversie in thermomagnetische motoren/generatoren, die restwarmte om kunnen zetten in kinetische/elektrische energie.

Gadolinium metaal is het standaard referentiemateriaal voor de toepassing van het MCE. Echter, dit materiaal vertoont een beperkt MCE met een tweede-orde magnetische faseovergang. Verschillende intermetallische materiaalklassen met een eerste-orde magnetische faseovergang, welke een zeer groot MCE tot gevolg heeft, zijn tot nu toe ontdekt, waaronder $La(Fe,Si)_{13}$ legeringen, $MnFeP(As, Ge, Si)$ legeringen en Ni-Mn Heusler legeringen.

Om een magnetocalorisch materiaal te ontwerpen dat geschikt is voor toepassingen is in de eerste plaats een inschatting van de gewenste samenstelling vereist, welke kan worden verkregen uit het fasediagram. Ten tweede moet er een geschikte route voor de synthese worden gekozen. Ten derde moet de stoichiometrie van de samenstelling worden geoptimaliseerd om de vorming van onzuiverheidsfasen te voorkomen. Voor toepassingen op het terrein van energieconversie, moet het gewenste materiaal een magnetische faseovergang vertonen die bij voorkeur gepositioneerd is in de buurt van de overgang tussen een eerste-orde magnetische faseovergang (FOMT) en een tweede-orde magnetische faseovergang (SOMT). Als de faseovergang een FOMT of SOMT is, dan kan de warmtebehandeling worden aangepast, de samenstelling worden veranderd, of kunnen er nieuwe elementen geïntroduceerd, totdat de magnetische faseovergang in de buurt van het kritische punt (CP) is gebracht. Tenslotte, moet gecontroleerd worden of magnetische overgang in het bereik van de beoogde werktemperatuur ligt. Zo niet, dan moet de samenstelling en de synthese worden aangepast totdat een optimaal materiaal is gevonden.

Experimentele diagrammen van de ferromagnetische overgangstemperatuur ($T_C$) en de thermische hysterese als functie van de samenstelling zijn geconstrueerd voor

het (Mn,Fe)$_2$(P,Si) system en dienen als richtlijn om geschikte samenstellingen voor de toepassingen te bepalen. De structuurverandering bij het passeren van de magnetische faseovergang is gerelateerd aan de thermische hysterese van de magnetische faseovergang, die experimenteel bepaald is in een van de diagrammen. Er is gevonden dat zowel Mn-rijke samples als Fe-rijke samples met een lage Si concentratie een lage hysterese laten zien, waardoor deze materialen veelbelovende kandidaten vormen voor toepassingen in een thermomagnetische motor.

Het effect van V substitutie voor Fe is onderzocht in de Mn$_{0.7}$Fe$_{x-z}$V$_z$P$_{0.6}$Si$_{0.4}$ legeringen. De (Mn,Fe)$_{1.91}$(P,Si) stoichiometrie was gekozen als startpunt om een zo laag mogelijke concentratie van onzuiverheidsfasen te krijgen. Voor een toenemende V concentratie zet de $a$ as uit en krimpt de $c$ as (samen met de $c/a$ ratio), terwijl het volume van de eenheidscel ongeveer gelijk blijft. De ferromagnetische overgangstemperatuur $T_C$ neemt af voor een toename in de V concentratie. In de Mn$_{0.7}$Fe$_{1.18}$V$_{0.03}$P$_{0.6}$Si$_{0.4}$ legeringen, 93% van de verzadigingsmagnetisatie was bereikt in een aangelegd magnetisch veld van 0.5 T bij een temperatuur van 5 K, wat deze legering een veelbelovende kandidaat maakt voor toepassingen in lage magneetvelden. De warmtebehandeling is duidelijk van invloed op de hoeveelheid onzuiverheidsfasen die zich vormt, en als gevolg daarvan op de samenstelling van de beoogde fase. In dit geval bevatten samples die gekoeld zijn in de oven een grotere fractie aan onzuiverheidsfasen dan de samples die een temperatuur quenching hebben ondergaan, wat leidt tot een lagere magnetische overgangstemperatuur.

De huidige methoden die gebruikt worden on de FOMT en SOMT materialen te classificeren zijn toegepast en vergeleken voor een reeks Mn$_{1.3}$Fe$_{0.7}$P$_{1-y}$Si$_y$ ($y$ = 0.4, 0.5 en 0.6) samples. De FOMT samples zijn eenvoudig te herkennen. Elk van de criteria laat zien dat de $y$ = 0.4 en 0.5 samples een FOMT materiaal zijn. Echter, de SOMT en CP samples zijn problematischer om te onderscheiden. In dit proefschrift is gevonden dat verschillende criteria tot verschillende conclusies leidt voor het $y$ = 0.6 sample. Op basis van de latente warmte, komt het $y$ = 0.6 sample overeen met een FOMT. Op basis van de XRD data en de veldafhankelijkheid van $T_C$, is het $y$ = 0.6 sample te classificeren als precies op het CP. Echter, op basis van de Arrott plots, de geleidelijke afhankelijkheid van de entropieverandering met het magnetische veld en de nieuw voorgestelde $n$, komt het $y$ = 0.6 sample overeen met een SOMT (maar dicht in de buurt van het CP).

De structurele, magnetische en elektronische eigenschappen van LaFe$_{11.8-b}$Co$_b$Si$_{1.2}$ ($b$ = 0.25, 0.69 en 1.13) legeringen zijn bestudeerd. Voor een toenemende Co

concentratie verschuift het materiaal van FOMT naar een SOMT, neemt $T_C$ toe en blijft de thermische hysterese verwaarloosbaar. Binnen de eenheidscel is het belangrijkste gevolg een verandering in de bindingsafstand tussen de *8b* en *96i* posities en een verandering in de bindingsafstand van één van de naburige *96i* posities. De negatieve thermische uitzetting wanneer de faseovergang wordt gepasseerd gaat samen met een hoekverdraaiing voor de oriëntatie van de kooi die gevormd wordt door de atomen op de 96*i* posities binnen de kubische eenheidscel. Het experimentele diagram van de elektronendichtheid laat zien hoe de kooi roteert binnen de primitieve cel. De samples met een lagere Co concentratie geven een grotere verandering in de elektronendichtheid dan het sample met de hoogste Co concentratie wanneer $T_C$ is gepasseerd.

De keuze van de synthesetechniek speelt een belangrijke rol in de fysische eigenschappen van de vervaardigde materialen. Voor laboratoriumschaal samples de meest gebruikte methode om $(Mn,Fe)_2(P,Si)$ legeringen te maken is kogelmalen. Voor Ni-Mn Heusler legeringen is de meest gebruikte synthesetechniek boogsmelten. In dit proefschrift kogelmalen is als synthesetechniek gebruikt om Ni-Mn Heusler legeringen te maken. Het voordeel van kogelmalen is dat de tijd van de warmtebehandeling kan worden ingekort. Op basis van de optimale sample preparatie kan de maximale magnetisatie worden gecontroleerd door de Ni/Mn en Mn/Sn ratio aan te passen. Het introduceren van kleine hoeveelheden van kobalt en aluminium leidt tot een significante toename in de magnetisatie.

# INTRODUCTION

**1**
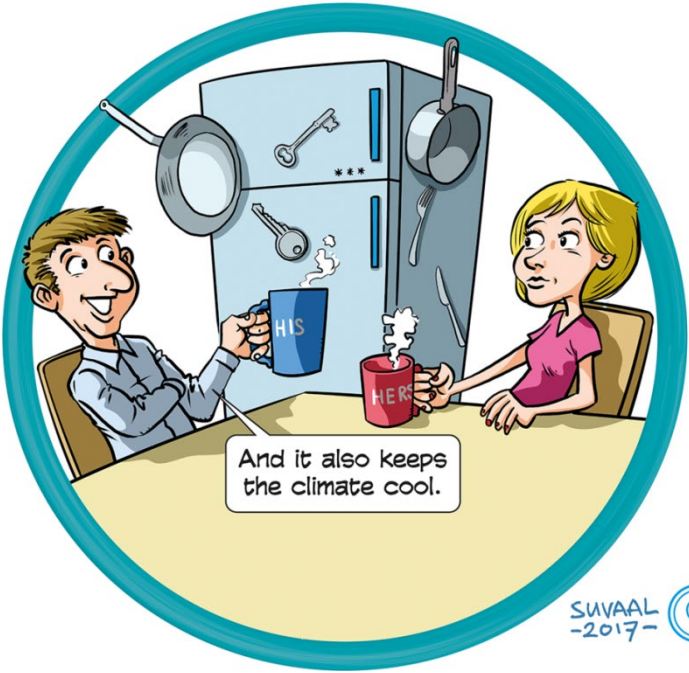
## 1.1 Magnetocaloric effect

The magnetocaloric effect (MCE) is a magneto-thermodynamic phenomenon in which a temperature change of a material is caused by exposing the material to a changing magnetic under adiabatic conditions. This effect was first observed by in 1917 by Weiss and A. Piccard [1, 2] who reported a discovery that nickel has a temperature rise of 0.7 ℃ in a 1.5 T applied field near its Curie temperature (354 ℃). Weiss and Piccard called their discovery a 'novel magnetocaloric phenomenon' [3].

By the middle of the 1920s, P. Debye [4] and Giauque [5] had independently realised that using adiabatic demagnetisation of paramagnetic salts can attain very low temperature. The physics behind it is similar to that of the magnetocaloric effect for ferromagnets. By magnetising the salt, while it is in thermal contact with a liquid helium bath, subsequent insulating the magnetised material, and then removing the magnetic field, temperatures below 1 K can be achieved. This was first experimentally demonstrated by Giauque and MacDougall in 1933 [6]. Due to his contributions in the field of chemical thermodynamics, particularly concerning the behaviour of substances at extremely low temperatures, Giauque was awarded the Nobel Prize in Chemistry in 1949 [7].

In 1997 Pecharsky and Gschneidner [8] reported the discovery of the so-called giant MCE close to room temperature in the first-order magnetic transition material $Gd_5Si_2Ge_2$. The giant MCE, observed at a transition temperature of 276 K, was much higher than that of other known MCMs at that time. This discovery initiated the renewed interest in research on magnetic refrigeration near room temperature. In the next year, Zimm [9] reported magnetic refrigeration using a 5 T field produces cooling powers exceeding 500 W.

Another significant milestone in magnetic refrigeration happened in 2002 when Brück, Tegus and colleges found a new giant MCE system [10, 11] in $Fe_2P$-type magnetocaloric materials. This $(Mn,Fe)_2(P,As)$ materials, have a large MCE, and the operating temperature can be tuned from 150 to 335 K by tuning the P/As ratio. Further progress was made by replacing the toxic element As to the non-toxic element Si, while the giant MCE is preserved [12-16].

In 2015, Haier, Astronautics, and BASF presented the first prototype of a magnetocaloric wine cooler at the International Consumer Electronics Show in Las Vegas. [17] This prototype is using $Fe_2P$-type materials as magnetocaloric

refrigerant for huge MCE and non-toxic, earth-abundant and affordable element compositions.

## 1.2 Applications of magnetocaloric effect

There are two main applications based on MCE. One is magnetic refrigeration, which can expel heat in a magnetic field cycle. Another one is thermomagnetic motors/generators, which can transfer waste heat into kinetic/electric energy.

### 1.2.1 Magnetic refrigeration

Figure 1.1 demonstrates the principle of magnetic refrigeration. In the initial stage, the magnetic moments are randomly oriented. When a magnetic field is applied, the magnetic moments align, resulting in heating of the magnetic material. This heat is removed from the material to the surroundings by heat transfer. When the field is removed, the magnetic moments randomise, which leads to cooling of the material. The heat from the system to be cooled can then be extracted using a heat-transfer medium. The heat-transfer medium may be water (with antifreeze) near room temperature, and for very low temperatures, helium. Magnetic refrigeration is an environmentally friendly cooling technology. It does not use ozone-depleting chemicals (CFCs), hazardous chemicals ($NH_3$) or greenhouse gases (HCFCs and HFCs). Another key difference between vapour-cycle refrigerators and magnetic refrigerators is the efficiency of energy conversion during the refrigeration cycle.
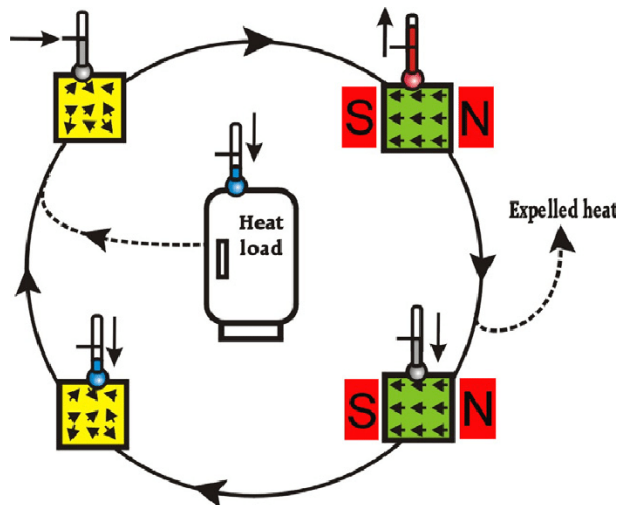


***Figure 1.1*:** Schematic graph of a magnetic refrigeration cycle. [18]

**1**
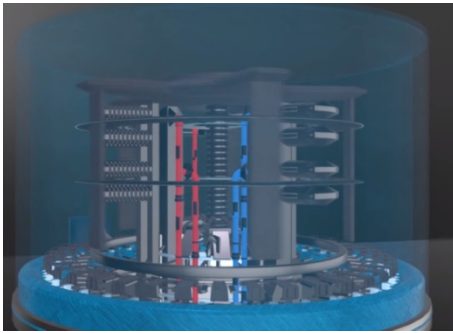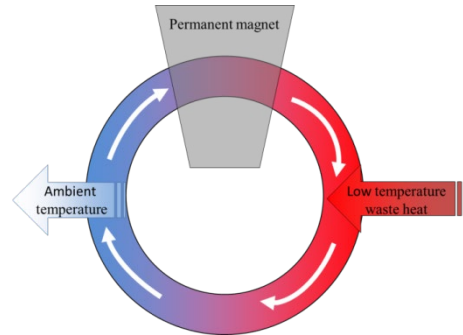


<center>(a)                                 (b)</center>

***Figure 1.2***: Schematic graph of (a) the thermomagnetic motor based on the Swiss-Blue Energy design prototype. (b) the working principle of the thermomagnetic motor.

### 1.2.2 Thermomagnetic motor

In the 19th century, Nikola Tesla [19, 20] and Thomas Alva Edison [21] patented concepts for thermomagnetic motors. A thermomagnetic motor consists of a permanent magnet and a rotatable ring of magnetocaloric material (MCM). The motor rotates because it undergoes a thermodynamic cycle. In the initial stage, the cold ferromagnetic MCM is attracted by the permanent magnet. The integral gain of mechanical energy is associated with this torque. Then the MCM is heated up by low-temperature waste heat and thereby transforms into the paramagnetic state. Thus, the MCM ring leaves the permanent magnet. A prototype build by the Swiss Blue Energy company using gadolinium as MCM has reached a power output of 1.4 kW.[22]

## 1.3 Magnetocaloric materials

Pecharsky and Gschneidner at Ames Lab discovered a giant magnetocaloric effect in $Gd_5Si_2Ge_2$ [8, 23] alloys near ambient temperature. This large MCE was due to coupled magnetic and structural transitions, which are of first-order, which could be induced by applying a magnetic field. Before this time gadolinium metal was the main candidate material, but it has a smaller MCE with a second-order magnetic transition.
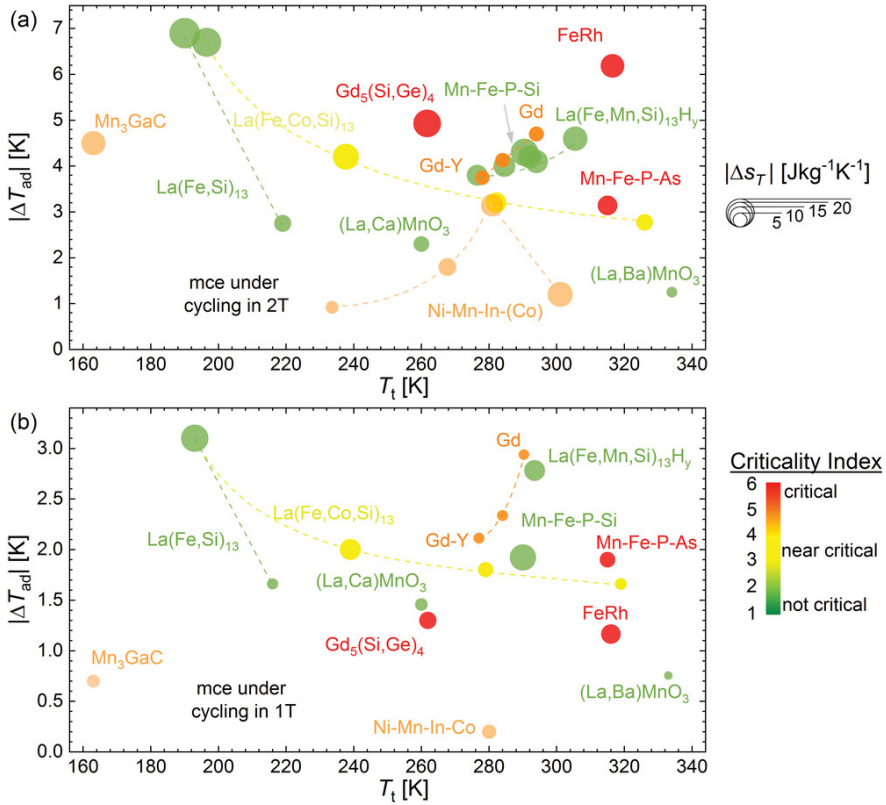
***Figure 1.3***: Ashby-like diagrams of magnetocaloric materials. These plots show both the reversible adiabatic temperature change ΔTad and the isothermal entropy change ΔST (illustrated by the area of the spots) versus the operating temperature Tt in a magnetic field change of a) 2 T and b) 1 T. The criticality of the respective compounds is represented by the colour of the data points. Every data point stands for a single material. [24]

Since that time, several intermetallic material systems with a giant MCE have been discovered and developed, including La(Fe, Si)$_{13}$-based [25, 26] alloys, MnFeP(As, Ge, Si) [10, 27, 28] alloys, and Ni–Mn-based Heusler alloys. [29]

The performance of magnetocaloric materials depends mainly on two parameters: the adiabatic temperature change ($\varDelta T_{ad}$) and the entropy change ($\varDelta S_T$) under isothermal conditions. A promising candidate should have large values for both parameters. A comparison of magnetocaloric properties ($\varDelta T_{ad}$ and $\varDelta S_T$) for near-room temperature magnetic refrigerants is shown in figure 1.3

**1**
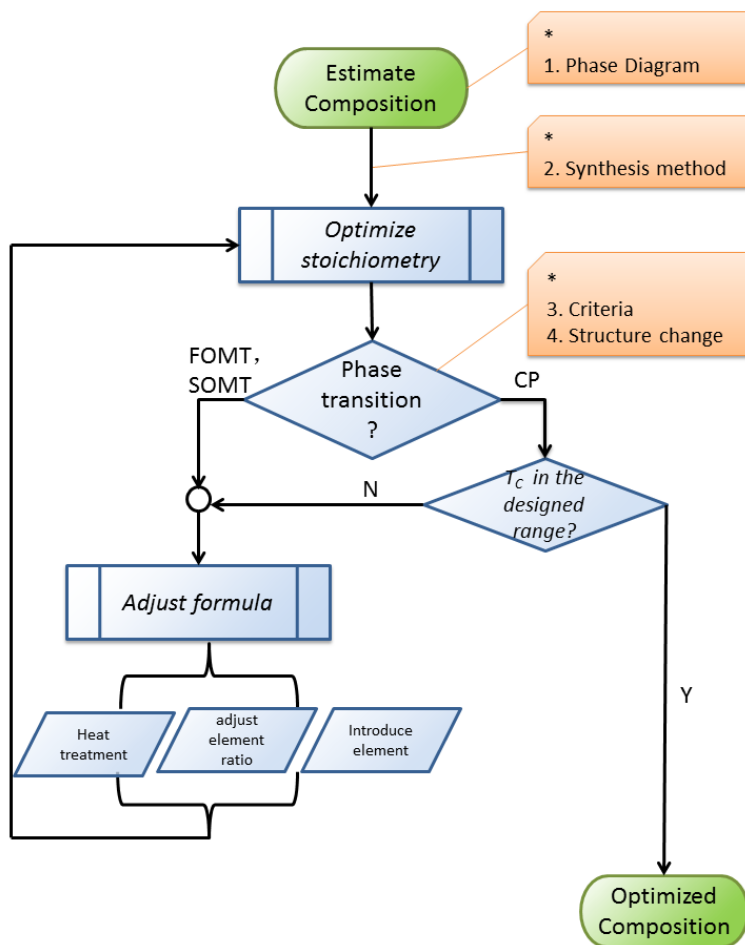


**Figure 1.4**: Flowchart for the design of magnetocaloric materials.

## 1.4 Thesis outline

The design process of magnetocaloric materials is shown in figure 1.4. First of all, we should have an estimated recipe, which can be obtained from the phase diagram. Secondly, a proper synthesis route should be chosen. Thirdly, the stoichiometry material should be optimised to avoid impurity phases. Then, the desired material should be on the border between a first-order phase transition (FOMT) and a second-order phase transition (SOMT). [30] If it is a FOMT or SOMT, the formula will be adjusted by changing the heat treatment, the element ratio and introducing

new elements, until the transition is close to the critical point (CP). Here, questions arise, how to determine the order of the transition, and how to determine the structure. From a fundamental point of view, how the electron density changes across the transition. Finally, the transition temperature needs to be checked to see it is in the designed working temperature range. If not, the recipe needs to be adjusted until we get an optimised composition.

In this thesis, I focus on answering the questions shown in the flowchart.

*Chapter 2* aims to provide some theoretical aspects of thermodynamic and Landau theory. Additionally, details of the sample preparation and characterisation are presented in this chapter. The influence of the heat treatment in $(Mn,Fe)_2(P,Si)$ compounds is also shown in this chapter.

*Chapter 3* to *chapter 5* report on **$(Mn,Fe)_2(P,Si)$** compounds.

*In Chapter 3*, the phase diagram was constructed as a guidance to estimate suitable compositions for applications (*question 1* in the flow chart). The structure change is coupled to thermal hysteresis of the magnetic transition in the phase diagram. An example is given to illustrate the usage of the phase diagram.

In *Chapter 4*, the way of optimising the stoichiometry before introducing a new element is discussed. The element vanadium is introduced to suit a small driving field in the applications.

In *Chapter 5*, The different criteria (*question 3* in the flow chart) are subsequently evaluated. For the typical FOMT and SOMT sample, it is easy to distinguish the nature of the transition. However, for the CP and SOMT sample, different criteria leads to different results.

*Chapter 6* reports on the charge distribution in **$La(Fe,Co,Si)_{13}$** compounds using synchrotron X-ray diffraction (*question 4* in the flow chart). Based on the temperature-dependent X-ray diffraction data, the electron density map is drawn to reveal charge redistributions when the sample crosses the transition.

*Chapter 7* shows the influence of different synthesis methods (*question 2* in the flow chart). A unique synthesis method is applied in the **NiMnSn** compounds. The comparison of different synthesis methods provides a concept of choosing an appropriate synthesis method.

*Chapter 8* describes the main conclusions of this thesis., followed by some recommendations for further research.

## References

1. Weiss, P. and A. Piccard, *Le phénomène magnétocalorique.* J. Phys. Theor. Appl., 1917. **7**: p. 103 - 109.

2. Smith, A., *Who discovered the magnetocaloric effect?* The European Physical Journal H, 2013. **38**: p. 507-517.

3. Weiss, P. and A. Piccard, *Sur un nouveau phénomène magnétocalorique.* Comptes Rendus, 1918. **166**: p. 352-354.

4. Debye, P., *Einige bemerkungen zur magnetisierung bei tiefer temperatur.* Annalen der Physik, 1926. **386**: p. 1154-1160.

5. Giauque, W., *A thermodynamic treatment of certain magnetic effects. A proposed method of producing temperatures considerably below 1 absolute.* Journal of the American Chemical Society, 1927. **49**: p. 1864-1870.

6. Giauque, W. and D. MacDougall, *Attainment of Temperatures Below 1° Absolute by Demagnetization of $Gd_2(SO_4)_3 \cdot 8H_2O$.* Physical Review, 1933. **43**.

7. *https://www.nobelprize.org/prizes/chemistry/1949/summary/.*

8. V. K. Pecharsky, K.A.G., Jr., *Giant Magnetocaloric Effect in $Gd_5(Si_2Ge_2)$.* Physical Review Letters, 1997. **78**: p. 4.

9. Zimm, C., et al., *Description and performance of a near-room temperature magnetic refrigerator*, in *Advances in cryogenic engineering.* 1998, Springer. p. 1759-1766.

10. Tegus, O., et al., *Transition-metal-based magnetic refrigerants for room-temperature applications.* Nature, 2002. **415**: p. 150-152.

11. Bruck, E., et al., *Magnetic refrigeration towards room-temperature applications.* Physica B-Condensed Matter, 2003. **327**: p. 431-437.

12. Albertini, F., et al., *Phase transitions and magnetic entropy change in Mn-rich Ni2MnGa alloys.* Journal of Applied Physics, 2006. **100**.

13. Thanh, D.T.C., et al., *Structure, magnetism, and magnetocaloric properties of $MnFeP_{1-x}Si_x$ compounds.* Journal of Applied Physics, 2008. **103**.

14. Dung, N.H., et al., *From first-order magneto-elastic to magneto-structural transition in $(Mn,Fe)_{1.95}P_{0.50}Si_{0.50}$ compounds.* Applied Physics Letters, 2011. **99**.

15. Dung, N.H., et al., *Mixed Magnetism for Refrigeration and Energy Conversion.* Advanced Energy Materials, 2011. **1**: p. 1215-1219.

16. Guillou, F., et al., *Taming the First-Order Transition in Giant Magnetocaloric Materials.* Advanced Materials, 2014. **26**: p. 2671-2675.

17. *https://www.basf.com/global/en/media/news-releases/2015/01/p-15-100.html.*

18. Brück, E., *Developments in magnetocaloric refrigeration.* Journal of Physics D: Applied Physics, 2005. **38**: p. 381-391.

19. Tesla, N., *Thermo-magnetic motor*, U.S. PATENT, 1889.

20. Tesla, N., *Pyromagneto-electric generator*, U.S. PATENT, 1890.

21. Edison, T., *Pyromagnetic Motor*, U.S. PATENT, 1888.

22. *http://www.swiss-blue-energy.ch/.*

23. Pecharsky, V.K. and K.A. Gschneidner, *Tunable magnetic regenerator alloys with a giant magnetocaloric effect for magnetic refrigeration from ~ 20 to ~ 290 K.* Applied Physics Letters, 1997. **70**: p. 3299-3301.

24. Gottschall, T., et al., *Making a Cool Choice: The Materials Library of Magnetic Refrigeration.* Advanced Energy Materials, 2019. **9**.

25. Hu, F., et al., *Influence of negative lattice expansion and metamagnetic transition on magnetic entropy change in the compound $LaFe_{11.4}Si_{1.6}$.* Applied Physics Letters, 2001. **78**: p. 3675-3677.

26. Fujieda, S., A. Fujita, and K. Fukamichi, *Large magnetocaloric effect in La $(Fe_xSi_{1-x})_{13}$ itinerant-electron metamagnetic compounds.* Applied Physics Letters, 2002. **81**: p. 1276-1278.

27. Trung, N.T., et al., *Tunable thermal hysteresis in MnFe(P,Ge) compounds.* Applied Physics Letters, 2009. **94**.

28. Nguyen H. Dung, et al., *Mixed Magnetism for Refrigeration and Energy Conversion.* Advanced Energy Materials, 2011. **1**: p. 5.

29. Krenke, T., et al., *Martensitic transitions and the nature of ferromagnetism in the austenitic and martensitic states of Ni−Mn−Sn alloys.* Physical Review B, 2005. **72**.

30. Singh, S., et al., *Large Magnetisation and Reversible Magnetocaloric Effect at the Second-Order Magnetic Transition in Heusler Materials.* Advanced Materials, 2016.

# THEORY, EXPERIMENTAL AND TECHNIQUE

# 2

The experiment is the sole criterion for testing theory.

-inspired by Mao Zedong

实践是检验真理的唯一标准。

—毛泽东

## 2.1 Theoretical aspects

### 2.1.1 Thermodynamic and Maxwell equation

The Gibbs free energy of a magnetic material with a magnetisation $M$ in an external magnetic field $\mu_0 H$ is defined as: [1-3]

$$G = U - TS + PV - \mu_0 HM \tag{2.1}$$

where $U$ represents the internal energy, $T$ the absolute temperature, $S$ the total energy, $P$ the pressure and $V$ the volume.

Implementing the potential for a magnetic material in an external field into the First law of thermodynamics, the total differential of internal energy $U = U(S, V, M)$ can be written as:

$$dU = TdS - PdV + \mu_0 HdM \tag{2.2}$$

Correspondingly, the differential of the Gibbs free energy can be expressed by combining equation (2.1) in equation (2.2):

$$dG = -SdT + VdP - Md(\mu_0 H) \tag{2.3}$$

In a solid system under constant atmospheric pressure, the total differential of the Gibbs free energy can be written as:

$$dG(T, \mu_0 H) = \left(\frac{\partial G}{\partial T}\right)_{\mu_0 H} dT + \left(\frac{\partial G}{\partial \mu_0 H}\right)_T d(\mu_0 H) \tag{2.4}$$

The second derivatives of $G$ are equal:

$$\left(\frac{\partial}{\partial \mu_0 H}\left(\frac{\partial G}{\partial T}\right)_{\mu_0 H}\right)_T = \left(\frac{\partial}{\partial T}\left(\frac{\partial G}{\partial \mu_0 H}\right)_T\right)_{\mu_0 H} \tag{2.5}$$

Hence, we obtain:

$$S(T, \mu_0 H, P) = -\left(\frac{\partial G}{\partial T}\right)_{\mu_0 H, P} \tag{2.6}$$

$$V(T, \mu_0 H, P) = \left(\frac{\partial G}{\partial P}\right)_{T, \mu_0 H} \tag{2.7}$$

$$M(T, \mu_0 H, P) = -\left(\frac{\partial G}{\partial \mu_0 H}\right)_{T, P} \tag{2.8}$$

Combining of equation (2.5), (2.6), (2.7) and (2.8) leads to the following Maxwell relation:

$$\left(\frac{\partial S}{\partial \mu_0 H}\right)_T = \left(\frac{\partial M}{\partial T}\right)_{\mu_0 H} \tag{2.9}$$

The most common way to derive the total entropy change based on magnetisation data is to integrate the Maxwell relation (2.9). The isothermal entropy change induced by an applied magnetic field change from $\mu_0 H_0$ to $\mu_0 H_1$ corresponds to:

$$\Delta S(T, \Delta B) = \int_{\mu_0 H_0}^{\mu_0 H_1} \left(\frac{\partial M(T, \mu_0 H)}{\partial T}\right)_{\mu_0 H} d(\mu_0 H) \tag{2.10}$$

### 2.1.2 Landau theory

The Landau model provides an approach to explain the Gibbs free energy change near the Curie temperature $T_C$. In this model, the change in Gibbs free energy $\Delta G$ from unordered paramagnetic state to ordered ferromagnetic state is described in terms of the magnetisation $M$: [4, 5]

$$\Delta G = \frac{\alpha}{2} M^2 + \frac{\beta}{4} M^4 + \frac{\gamma}{6} M^6 + \cdots - \mu_0 H M \tag{2.11}$$

The Landau theory can be used to characterise the transition temperature and the order of the transition. The coefficient $\alpha = \alpha_0 (T - T_0)$ depends on temperature. Minimisation with respect to the magnetisation $M$ leads to the equation of state:

$$\alpha + \beta M^2 + \gamma M^4 = \frac{\mu_0 H}{M} \tag{2.12}$$

The nature of the magnetic transition described by equation 2.12 can be evaluated by the Arrott plot showing which is $M^2$ versus $(\mu_0 H)/M$. Three different cases can be distinguished:

(i)    $\beta < 0$: First-order phase transition (FOMT) with a discontinuous change in the entropy ($\Delta S$), magnetisation ($\Delta M$), and volume ($\Delta V$).

(ii)    $\beta > 0$: Second-order phase transition (SOMT) with continuous change in the entropy ($\Delta S$), magnetisation ($\Delta M$), and volume ($\Delta V$).

(iii)   $\beta = 0$: Critical point (CP) on the border between the FOMT and SOMT.

Further discussion on distinguishing the different types of the magnetic phase transition is presented in chapter 5 for first and second-order phase transitions in $(Mn,Fe)_2(P,Si)$ compounds.

## 2.2 Experimental Techniques

Different families of magnetocaloric materials were prepared and characterised. The preparation was performed with several different synthesis methods. Each method has its advantages and disadvantages. The heat treatment has an effect on the forming of the desired phase. A variety of characterisations were applied to reveal the structure and magnetic properties across the phase transition. Figure 2.1 shows the fabrication methods and the main characterisation techniques used in this thesis.

**Fabrication**
- **Synthesis**
  - Ball milling
  - Arc melting
  - Melt spinning
- **Heat treatment**
  - Temperature
  - Time

**Characterisation**
- **Structural analysis**
  - SEM
  - XRD     Crystal structure, phase fractions
- **Thermal analysis**
  - DSC     Latent heat
- **Magnetisation**
  - SQUID ( 5 - 370 K)     $T_C$, $\Delta T_{hys}$, $\Delta S_m$, n factor, …
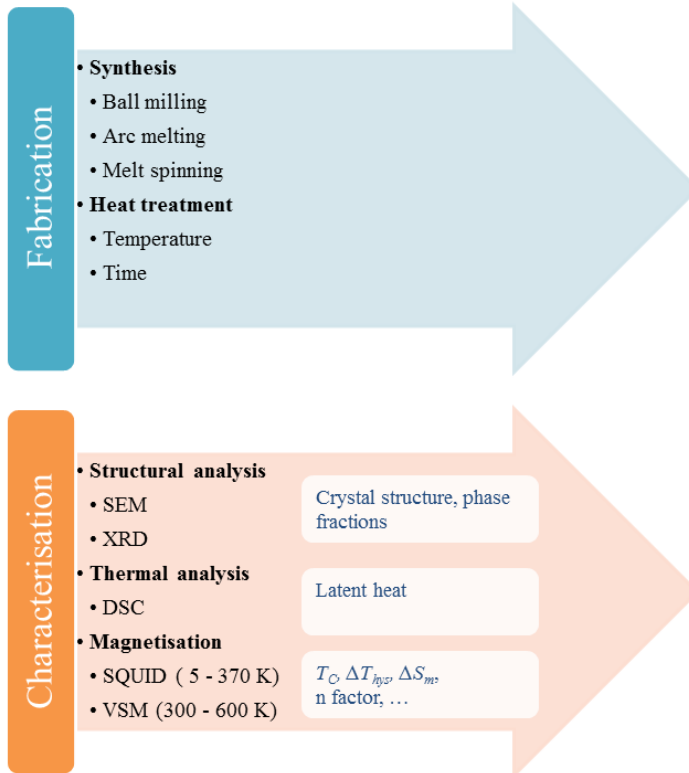  - VSM (300 - 600 K)

**Figure 2.1:** Flowchart showing the sample preparation and experimental techniques for the sample.
\* exponent $n$, $\Delta S(H) \propto H^n$

### 2.2.1 Sample fabrication

### 2.2.1.1 Synthesis methods

The most common methods for lab-scale alloy synthesis are ball milling, arc-melting and melt spinning.

### 2.2.1.1.1 Ball milling

Ball milling is a widely used technology for grinding, mixing and mechanical alloying of materials. A schematic drawing of a planetary ball milling machine is shown in figure 2.2. The materials and grinding balls were sealed in grinding jar under argon atmosphere to avoid introducing moisture and oxygen. Figure 2.2 shows that the rotation direction of the planetary disk is in the opposite direction of the grinding jars (Figure 2.2(a)). The motion between the grinding balls and powders produces shear and centrifugal forces, which release a high dynamic energy to alloy the materials (Figure 2.2(b)).

The polycrystalline samples were prepared by a ball-milling method using a Fritsch Pulverisette 5. Typically, an amount of 10 g of raw starting materials were placed in the grinding jar with 15 grinding balls (10 mm diameter, 4 gram). Based on previous research [6], the ball milling time for $(Mn,Fe)_2(P,Si)$ compounds is chosen to be 10 hours. For $(Mn,Fe)_2(P,Si)$, the starting materials are Fe (99.9%), Mn (99.9%), red-P (99.7%), and Si (99.9%) powder. The rotation speed is 350 rounds per minute (rpm). For NiMnSn compounds, the starting materials are Ni(99.8%), Mn (99.7%), Co( 99.8%) and Al (99.97%) powder and Sn shots (8 – 20 mesh, 99.8%). Ball milling is performed for 10 hours with a rotation speed of 190 rounds per minute (rpm). The powder is stuck on the wall during ball milling when we use 350 rpm for synthesis NiMnSn compounds. The as-milled powder was pressed into pellets.

The advantage of ball milling is that it is easy to control the composition of the final material. The disadvantage is that the preparation time is relatively long and that it is not easy to reproduce large amounts of material.
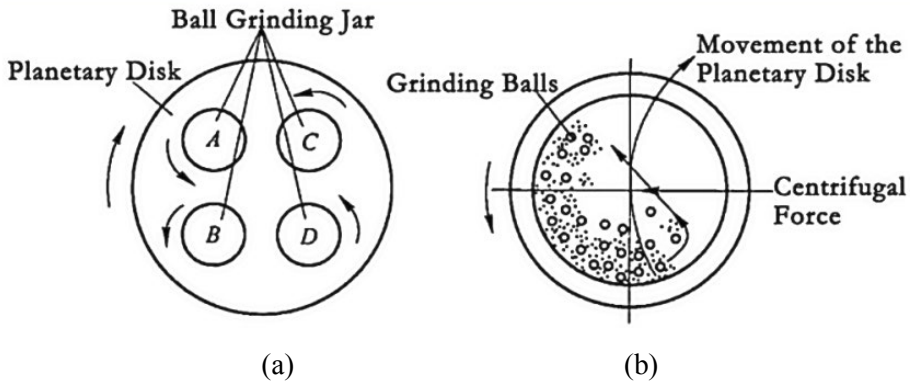
*Figure 2.2:* Schematic drawing of a planetary ball mill with (a) the overall layout of planetary disk and (b) horizontal section of grinding jar. [7]

### 2.2.1.1.2 Arc-melting

Arc-melting is a melting process to produce metal ingots. The arc-melting setup was built in-house to ensure high-quality samples. Figure 2.3 is a schematic graph of the arc-melting technique. The sample chamber was first evacuated to $10^{-7}$ mbar vacuum and then flushed with argon. The melting process was performed in argon atmosphere. Heating is performed from an electric arc between a tungsten electrode and raw materials placed in the copper crucible. The details of the arc-melting machine were described by Boeije. [8]
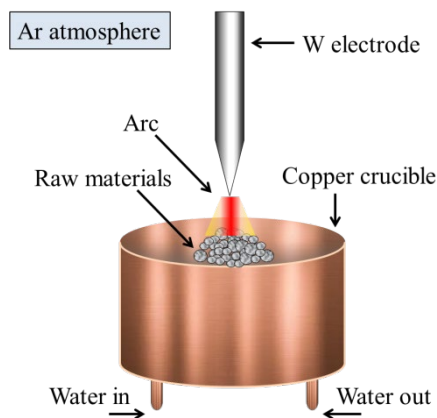


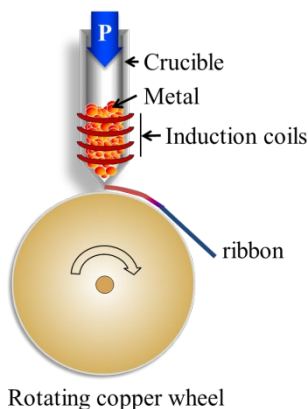*Figure 2.3:* Schematic drawing of the electric arc melting device.

**Figure 2.4:** Schematic drawing of melt-spinning process.

### 2.2.1.1.3 Melt spinning

Melt spinning is a rapid solidification technique that is typically used to form ribbons. As illustrated in figure 2.4, the metal is melted by induction coils. To obtain homogeneity, the sample is melted several times. The molten metal is pushed by gas pressure (P) through a small nozzle in the crucible onto a rotating copper wheel, where the liquid metal is rapidly cooled to form a solid ribbon.

The advantages of melt spinning are that it is a direct and simple process with a high production speed, which makes it easy scale up to mass production. The disadvantage of melt spinning is that it can only be applied for starting materials with a small variation in melting points.

In this work, the melt spinning method is used for the synthesis NiMnSn alloys. The melt spinner used in the study is produced by Edmund Buhler GmbH. The surface velocity of the copper wheel was about 45 m/s. Approximately 5 g of samples can be obtained in a single run.

### 2.2.1.2 Heat treatment

To get homogeneous samples, a heat treatment is applied to the as-prepared samples. The as-prepared samples were sealed in quartz ampoules in an argon atmosphere of 200 mbar. The heat treatment is different for different compounds. The heat treatment for NiMnSn compounds will be discussed in chapter 6. The heat treatment for $(Mn,Fe)_2(P,Si)$ compounds is presented in the following.
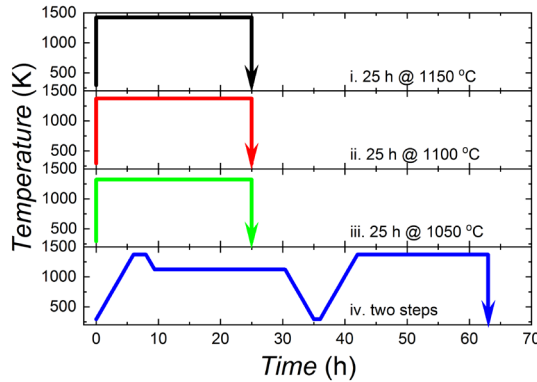
**2**



*Figure 2.5:* Schematic graph of the applied heat treatments.

Four different heat treatments are performed and compared. Figure 2.5 shows these different heat treatment. The first three heat treatments are to first heat the empty oven to 1050, 1100 or 1150 $^{\circ}$C, then put the cold sample directly in the preheated oven and quench it into water after 25 hours of heat treatment. Method iv is to put the sample in the cold oven. The sample is sintered at 1100 $^{\circ}$C for 2 hours, annealed at 800 $^{\circ}$C for 20 hours and then oven cooled to room temperature. After that the annealed sample was heated up to 1100 $^{\circ}$C again and kept for 20 hours before quenching into water.

Figure 2.6 (a) shows the temperature dependence of magnetisation for different heat treatments. The lowest magnetisation value at 180 K is found for sample 'iii', which also shows the lowest $T_C$. The other samples show almost the same trend. Figure 2.6 (b) shows the first derivative of the *M-T* curves. The higher the value the steeper the transition. It is clear that sample 'i' has the sharpest transition; samples 'i' and 'iii' show almost the same trend. However, sample 'iv' has a higher magnetisation value at 180 K than sample 'i'. Considering the impurity phase fractions, shown in figure 2.6 (c), sample 'iv' is the best sample with the highest magnetisation value, the highest – *dM/dT* value and the lowest impurity phase fraction. In contrast, sample 'iii' shows the worst properties among all heat treatments. The impurity fractions of samples 'i', 'ii' and 'iv' are comparable. The desired magnetocaloric material should be on the border of the FOMT and SOMT.

**2**
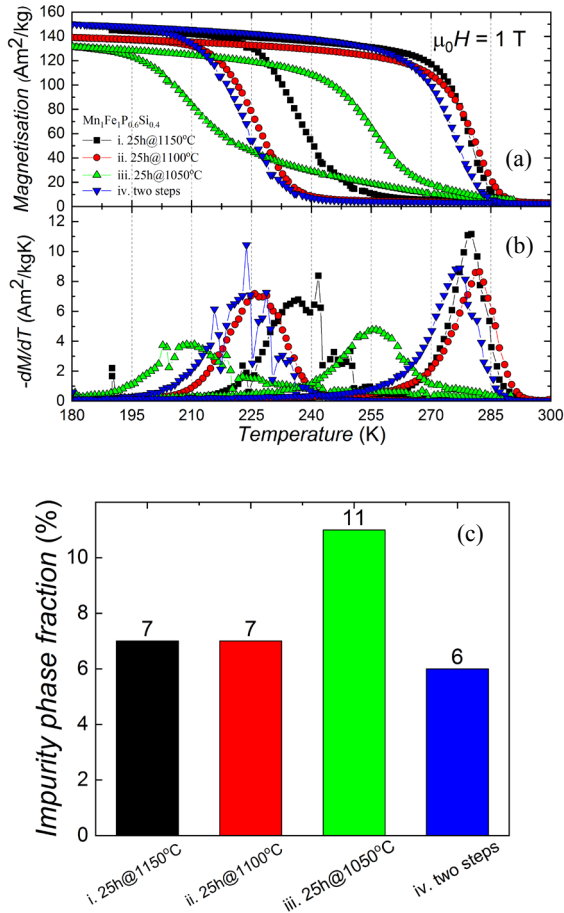
**Figure 2.6:** Temperature dependence of magnetisation of MnFeP$_{0.6}$Si$_{0.4}$ with different heat treatments measured in a field of $\mu_0 H = 1$ T (a). Together with the first derivative of M-T curves (b). (c) Phase fraction of the impurity phase analysed from X-ray powder diffraction data.

Therefore, sample 'i' was eliminated. Sample 'ii' has a shorter heat treatment time compared to the sample 'iv'. From the energy-saving aspect, heat treatment 'ii', with a preheated oven to 1100°C, and a cold sample put directly into the oven and quenched into water after 25 hours heat treatment, was chosen in the following (Mn,Fe)$_2$(P,Si) synthesis procedure.

**2.2.2 Sample characterisation**

**2.2.2.1 Structural analysis**

**2.2.2.1.1 Powder X-ray Diffraction**

X-ray powder diffraction patterns were collected in a PANalytical X-pert Pro diffractometer using Cu $K_\alpha$ radiation. The lattice parameters and the impurity phases are obtained by a full Rietveld refinement of the X-ray diffraction data using the FULLPROF package [9].

**2.2.2.1.2 High-resolution X-ray diffraction**

High-resolution X-ray diffraction (XRD) was performed on the BM01A beamline at the European Synchrotron Radiation Facility (ESRF) using a wavelength of 0.69264 Å and an energy of 17 keV. The covered temperature range is from 150 to 500 K in steps of 2 K. The temperature was controlled by a Nitrogen Cryosteam. The powder samples were placed in capillaries with a 0.5 mm diameter that were spun during exposure. Figure 2.7 shows the experimental set-up for the high-resolution X-ray diffraction.

The powder X-ray diffraction data were analysed by a Rietveld refinement using the FULLPROF package [9]. The electron densities were calculated from the fitted structure factors using VESTA [10]. The electron density at two different temperatures can be constructed by measuring the electron density at different temperatures.
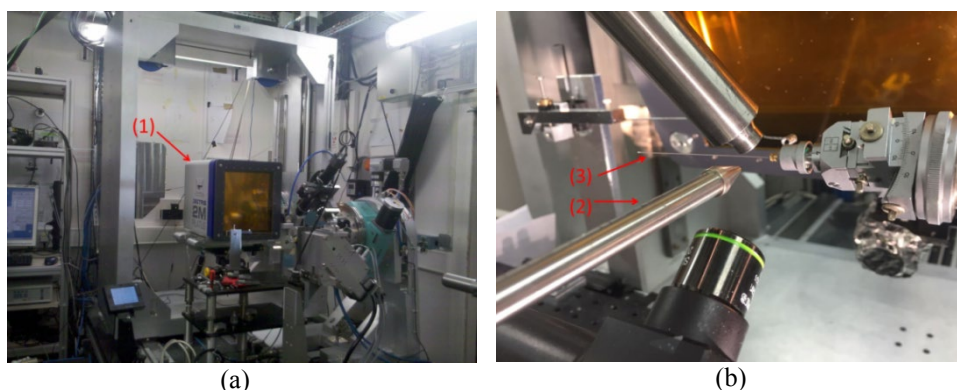


<div align="center">(a)        (b)</div>

*Figure 2.7:* Experimental set-up for the high-resolution X-ray diffraction. (a) photo of the set-up, (b) sample cell indicated are. (1) the detector, (2) the beam (3) samples placed in the capillary.

The electron density difference can be visualised by comparing and plotting the electron density difference at different temperatures. This electron density difference plots is complicated by the fact that the thermal motion of atoms changes the diffracted intensity. High temperature increases the thermal diffuse scattering and decreases the intensity at the diffraction peaks. However, the total scattered intensity should remain constant (neglecting absorption). Therefore, the sum of the structure factors over all lattice planes should be a constant. This constant was used as a scale factor in the electron density plots, considering that the integral over the electron density is equal to the number of electrons in the unit cell.

### 2.2.2.1.3 Scanning Electron Microscopy

Microstructures of the samples were analysed with a scanning electron microscope (JEOL JSM 6500F) equipped with an Autrata back-scattered electron (BSE) detector and coupled with energy disperse X-ray spectroscopy (EDS). Micrographs were taken with an electron beam energy of 15 keV. The phase fraction (area fraction) was obtained by ImageJ [11, 12].

### 2.2.2.1.4 Mössbauer spectroscopy

Transmission $^{57}$Fe Mössbauer spectra were collected at 400 K with a conventional constant-acceleration spectrometer and at 4.2 K with a sinusoidal velocity spectrometer, using a $^{57}$Co(Rh) source. A velocity calibration was carried out using an α-Fe foil at room temperature. The source and the absorbing sample were kept at the same temperature of 4.2 K during the measurements. The Mössbauer spectra were fitted using the Mosswinn 4.0 program [13] with a binomial distribution model, as previously described for the analysis of the Mossbauer spectra of $FeMnP_{1-x}As_x$ compounds [14].

### 2.2.2.2 Differential scanning calorimetry

Differential scanning calorimetry (DSC) is a thermal analytical technique used to study the thermal properties of materials. The measurements were carried out using a TA-Q2000 DSC, which uses liquid nitrogen to cool the system. The heat flow can be determined by measuring the temperature difference between a reference and the sample. The sample and the reference were placed in pans with lids. The outcome of the DSC measurements can be provide the heat capacity and the latent heat (by the integral area of the peak at the phase transition).

**2**

In this work, the aluminium pans and lids were used to place the sample, and the empty pan and lid were used as a reference. The temperature range for the aluminium pan and lid is -180 $^{\circ}$C to 600 $^{\circ}$C. The sweeping rate was 10 K/min (cooling and heating).

### 2.2.2.3 Magnetisation measurements

Magnetic properties were measured in a SQUID (Superconducting Quantum Interface Device) magnetometer using the RSO mode with temperature range of 5 - 370 K and in a VSM (vibrating sample magnetometer) with a temperature range of 300 – 600 K.

In this thesis, isofield magnetisation measurements (*M-T* curves) were measured with a sweep rate of 2 K/min upon cooling and heating. From a *M-T* curve, the magnetic transition temperature $T_C$ and the thermal hysteresis $\Delta T_{hys}$ can be calculated. In this work, $T_C$ and $\Delta T_{hys}$ were determined in an applied field of 0.01 T, where $T_C$ was defined by the heating curve. The magnetic entropy change *($\Delta S_m$)* for a field change is calculated from *M-T* curves in increasing field from 0.6 T to 2 T in steps of 0.2 T ( in chapter 3, we compare the different criteria for phase transitions where applied fields up to 5 T were applied).

### References

1.  Swalin, R., *Thermodynamics of solids* New York. 1962: John Wiley and Sons.

2.  Kuz'min, M. and A. Tishin, *Magnetocaloric effect. Part 1: An introduction to various aspects of theory and practice.* Cryogenics, 1992. **32**(6): p. 545-558.

3.  Tishin, A. and Y. Spichkin, *The magnetocaloric effect and its applications. Institute of Physics Publishing.* Bristol and Philadelphia, 2003.

4.  Uzunov, D.I., *Introduction to the theory of critical phenomena: mean field, fluctuations and renormalisation*. 1993: World Scientific.

5.  Carvalho, A.M.G., et al., *Investigation of the first-order metamagnetic transitions and the colossal magnetocaloric effect using a Landau expansion applied to MnAs compound.* The European Physical Journal B, 2009. **68**: p. 67-72.

6.  DŨNG, N.H., *Moment formation and giant magnetocaloric effects in hexagonal Mn-Fe-P-Si compounds*. 2012, TU Delft.

7.  *https://www.micronanotools.com/products/planetary-ball-mill-4x100ml-two-year-warranty-vacuum-and-inert-gas-grinding-compatible*.

8.  Boeije, M.F.J., *Electron density studies on magnetic systems*. 2017, TU Delft.

9.  Rodriguez-Carvajal, J., *Abstract Satelite Meeting on Powder Diffraction.* Congr. Int. Union of Crystallography. Toulouse: France, 1990.

10.  Momma, K. and F. Izumi, *VESTA 3 for three-dimensional visualisation of crystal, volumetric and morphology data.* Journal of Applied Crystallography, 2011. **44**: p. 1272-1276.

11.  Rasband, W.S., *ImageJ, U.S. National Institutes of Health, Bethesda, Maryland, USA*. http://imagej.nih.gov/ij/, 2011.

12.  Schneider, C.A., W.S. Rasband, and K.W. Eliceiri, *NIH Image to ImageJ: 25 years of image analysis*. Nature Methods, 2012. **9**: p. 671-675.

13.  Klencsár, Z., *Mössbauer spectrum analysis by Evolution Algorithm.* Nuclear Instruments and Methods in Physics Research Section B: Beam Interactions with Materials and Atoms, 1997. **129**: p. 527-533.

14.  Hermann, R.P., et al., *Mössbauer spectral study of the magnetocaloric $FeM_nP_{1-x}As_x$ compounds*. Physical Review B, 2004. **70**: p. 214425.

**2**

# PHASE DIAGRAM

## of the

## $Mn_xFe_{2-x}P_{1-y}Si_y$ SYSTEM

**3**
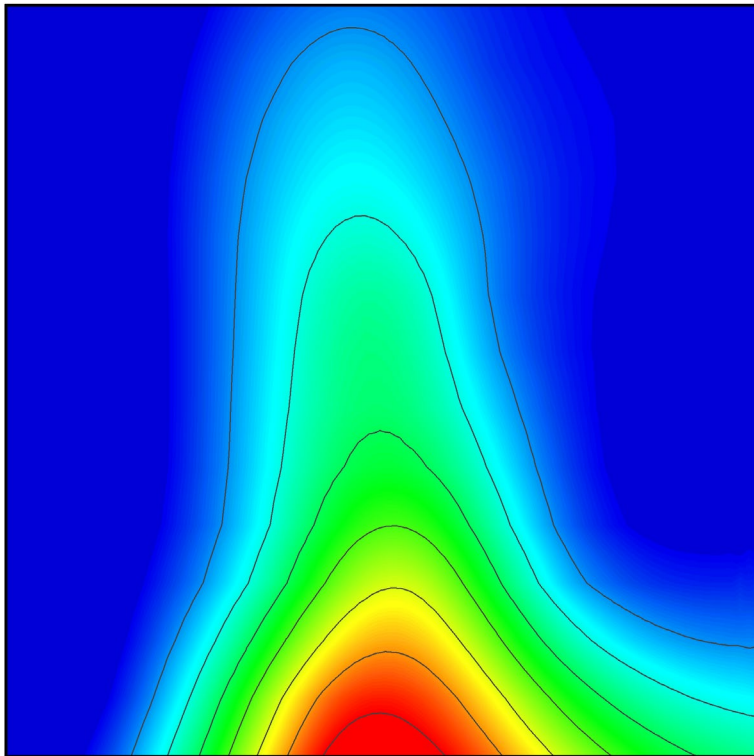
## 3.1 Introduction

The magneto-thermodynamic phenomenon that under adiabatic conditions a temperature change can be triggered in a solid by the application of an external magnetic field is known as the Magnetocaloric effect (MCE) [1]. It was discovered by Weiss and Picard in 1917 [2]. Magnetocaloric materials (MCMs) show great potential for utilisation in magnetic refrigeration and energy conversion. Some MCE materials such as Mn-Fe-P-based [3], La-Fe-Si based [4], and Ni-Mn-based materials [5] were widely studied for their giant MCE near room temperature. Materials with Curie temperatures near room temperature and small hysteresis can be found in the quaternary $(Mn,Fe)_2(P,Si)$ system. In order to find suitable compositions for applications, the phase diagram of the $Mn_xFe_{2-x}P_{1-y}Si_y$ system was investigated in a wide range of compositions (for a Mn fraction of $0.3<x<2$ and a Si fraction of $0.33 \leq y \leq 0.6$).

## 3.2 Experimental

Polycrystalline samples of $Mn_xFe_{2-x}P_{1-y}Si_y$ have been prepared by ball milling starting materials of Fe (99.9%), Mn (99.9%), red-P (99.7%), and Si(99.9%) powder. After 10 h of ball milling, the samples were pressed into tablets [6]. The tablets were sealed under Ar atmosphere in quartz ampoules, sintered at 1373 K for 25 h, and then quenched into water.

Powder diffraction patterns were collected in a PANalytical X-pert Pro diffractometer with Cu $K_\alpha$ radiation. The lattice parameters and the impurity phases are obtained by a full Rietveld analysis of the X-ray diffraction data using the FULLPROF package [7]. The heat capacity and latent heat were measured in a differential scanning calorimeter (DSC). The measurements were carried out in a TA-Q2000 DSC, which uses liquid nitrogen to cool the system. The sweeping rate was 10 K/min.

Magnetic properties were measured in a SQUID (Superconducting Quantum Interference Device) magnetometer using the RSO mode in the low-temperature range (5 -370 K) and VSM (vibrating sample magnetometer) in the high-temperature range (300 – 600 K). From the magnetic properties measurements, the magnetic transition temperature $T_C$ and the thermal hysteresis $\Delta T_{hys}$ can be calculated. In this work, $T_C$ and $\Delta T_{hys}$ were determined from the heating and cooling curves in an applied magnetic field of 0.01 T.

## 3.3 Results and discussion

### 3.3.1 Structure

A structural analysis has been performed to study the structure of the Mn$_x$Fe$_{2-x}$P$_{1-y}$Si$_y$ quaternary compounds. There are 4 possible lattice structures in the Mn$_x$Fe$_{2-x}$P$_{1-y}$Si$_y$. The orthorhombic Co$_2$P-type (*Pnma*) can form in the Si poor region ($y < 0.15$). The single hexagonal Fe$_2$P-type (*P-62m*) of Figure 3.1 can be found for Si compositions of $0.24 \leq y \leq 0.5$. For a Si composition of $0.5 \leq y < 1.0$, a three-phase region is observed, which consists of the Fe$_2$P-type, hexagonal Mn$_5$Si$_3$-type (*P6$_3$/mcm*) and the cubic Fe$_3$Si-type structure (*Fm-3m*) [8].

The silicon concentration ($0.33 \leq y \leq 0.6$) was chosen to synthesise Mn$_x$Fe$_{2-x}$P$_{1-y}$Si$_y$ samples with a hexagonal Fe$_2$P-type lattice structure. Here the investigated range of silicon concentrations has been restricted the to avoid the appearance of the orthorhombic lattice structure when the silicon concentration is too low. In contrast, if the silicon concentration is too high the three-phase region is entered (with the Fe$_2$P type main phase and the Fe$_3$Si and Mn$_5$Si$_3$ type impurity phases) resulting in a decrease in the phase fraction of the main phase [8]. The phase diagram for the phase composition of the Fe$_2$P type main phase and the Fe$_3$Si and Mn$_5$Si$_3$ type impurity phases is shown in Figure 3.2.
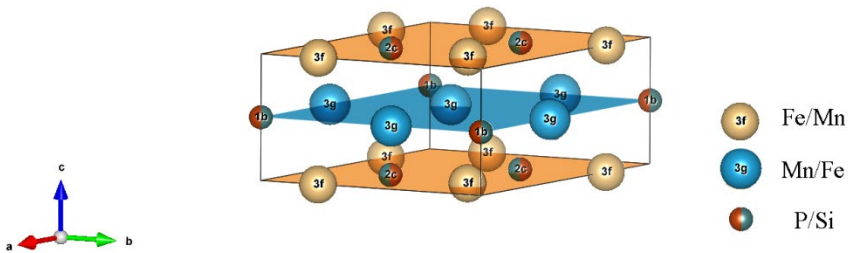


*Figure 3.1:* Unit cell of the hexagonal Fe$_2$P structure (space group *P-62m*) showing the Wyckoff positions and the layered structure. Mn and Fe atoms occupy the *3g* and 3f positions. P and Si atoms occupy the *2c* and *1b* positions.
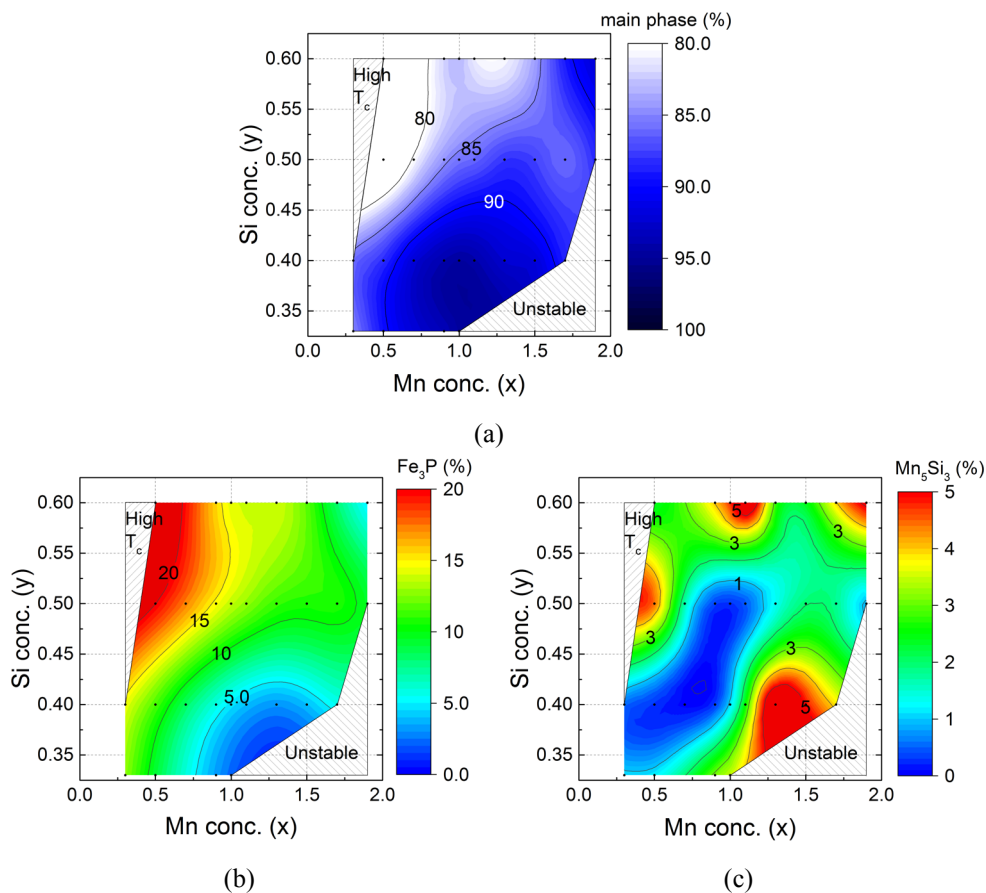
**3**



(a)



(b)



(c)

**Figure 3.2**: Phase diagrams of the $Mn_xFe_{2-x}P_{1-y}Si_y$ ($x = 0 - 2$, $y = 0.33 - 0.60$) system showing the phase fractions of (a) the $Fe_2P$ type main phase, (b) the $Fe_3P$ type impurity phase, and (c) the $Mn_5Si_3$ type impurity phase. The black points correspond to the experimental data.

The main impurity phase in the $Mn_xFe_{2-x}P_{1-y}Si_y$ compounds for iron-rich compounds ($x < 1$) is the $Fe_3Si$ type phase. Figure 3.2(b) shows that the $Fe_3Si$ impurity increases continuously for increasing Fe and Si concentrations. For high Mn and low Si concentrations, the $Mn_5Si_3$ type impurity phase is dominant.

Figure 3.3 shows the evolution in the lattice parameters of the hexagonal main phase with changing composition in the $Mn_xFe_{2-x}P_{1-y}Si_y$ compounds. The lattice parameter $a$ expands for increasing Mn and Si concentrations when $x > 1$ (Figure 3.3(a)). This phenomenon can be explained based on the atomic radius. The manganese atom has a larger radius than Fe atom, and Mn prefers the crystallographic *3g* site, while Fe prefers the *3f* site. When the *3g* site is fully

occupied, the rest Mn of the atoms occupy the *3f* site [9]. As a result, the lattice parameter *a* expands. Figure 3.3(b) shows that the lattice parameter *c* has a maximum value when Mn:Fe = 1:1. In this case the 3g site is fully occupied by Mn and the 3f site is fully occupied by Fe. The lattice parameter *c* is found to shrink for increasing Fe, Mn or Si concentration. The *c/a* ratio is 0.54 to 0.58, and shows a similar dependence on composition as lattice parameter *c*. (Figure 3.3(c))
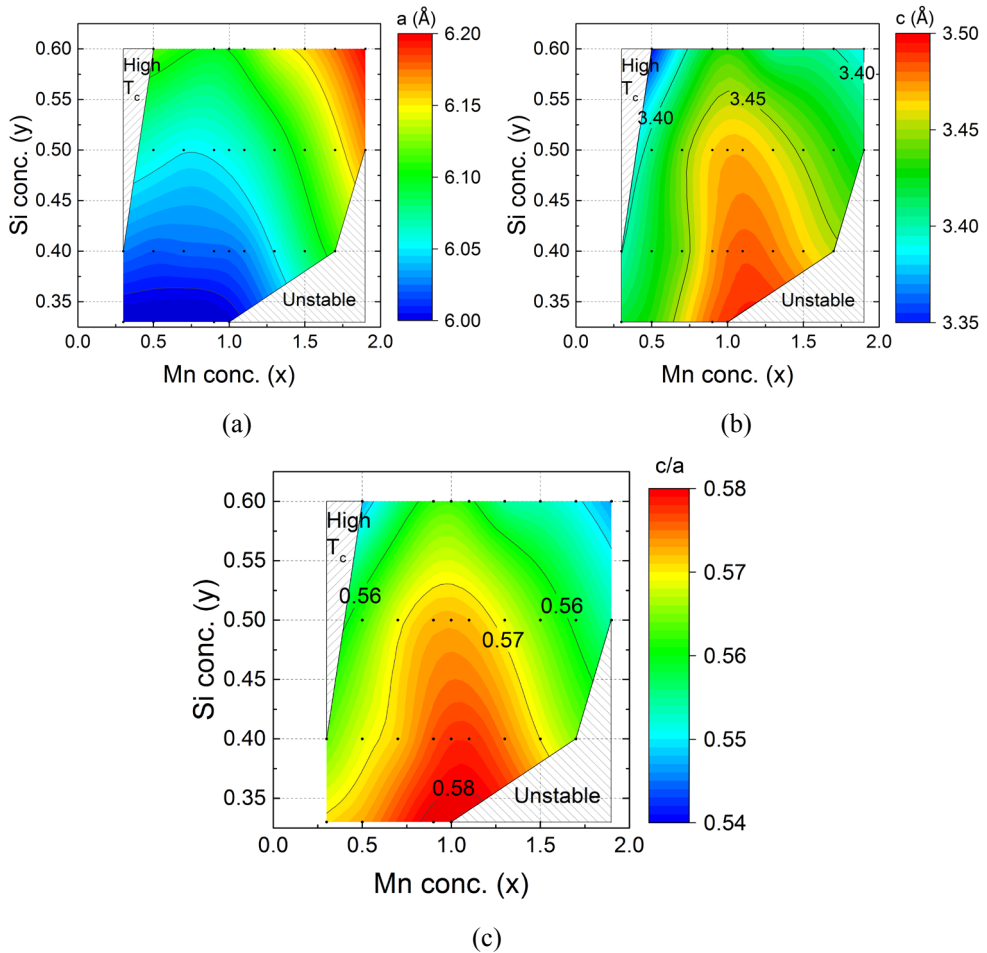


(a)

(b)



(c)

**Figure 3.3:** Composition dependence of the lattice parameters for the hexagonal Fe$_2$P type main phase in the Mn$_x$Fe$_{2-x}$P$_{1-y}$Si$_y$ system: (a) lattice parameter *a*, (b) lattice parameter *c*, and (c) the *c/a* ratio. The black points correspond to the experimental data. All data were measured in the paramagnetic state.
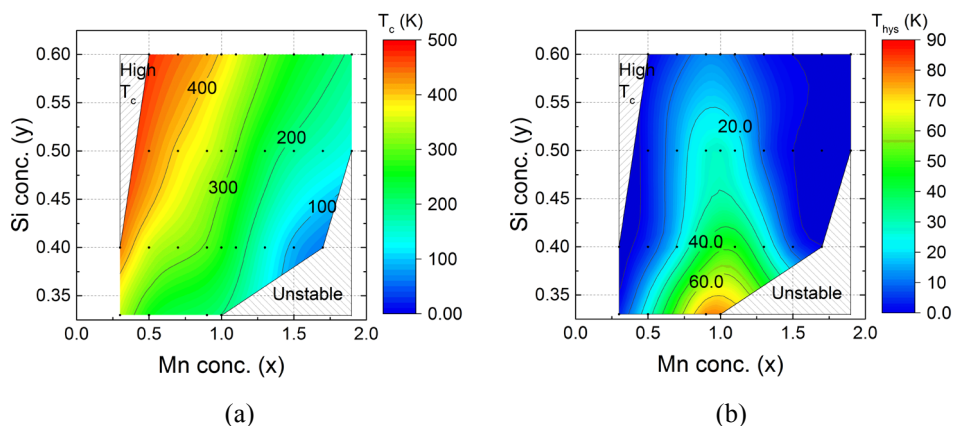
(a)                                    (b)

***Figure 3.4:*** Magnetic phase diagram of $Mn_xFe_{2-x}P_{1-y}Si_y$ ($x = 0 - 2$, $y = 0.33 - 0.60$) compounds showing the composition dependence of (a) the ferromagnetic transition temperature $T_C$ and (b) the thermal hysteresis $\Delta T_{hys}$. The black points correspond to the experimental data.

### 3.3.2 Phase diagram of $Mn_xFe_{2-x}P_{1-y}Si_y$

The magnetic phase diagram of the hexagonal $Fe_2P$ type main phase in the $Mn_xFe_{2-x}P_{1-y}Si_y$ ($x = 0.3 - 2.0$, $y = 0.33 - 0.60$) compounds was investigated by magnetisation measurements and is shown in Figure 3.4. In general, the ferromagnetic transition temperature $T_C$ increases with increasing Fe and Si contents. However, materials with a low thermal hysteresis $\Delta T_{hys}$ can be found both in the Fe-rich and in the Mn-rich region of the magnetic phase diagram.

### 3.3.2.1 Transition temperature and thermal hysteresis

The $Mn_xFe_{2-x}P_{1-y}Si_y$ compounds can cover a large range of ferromagnetic transition temperatures [10]. In this work, the transition temperature $T_C$ was found to range from 80 to 470 K. Part of the magnetic phase diagram is marked 'High $T_C$' as it shows a ferromagnetic transition temperature outside the measurement range ($T_C > 470$ K) and is therefore too high for both room temperature chilling or waste heat energy conversion applications. The highest transition temperature is found for high Fe and Si contents, while the lowest is found for low Fe and Si contents.

The thermal hysteresis $\Delta T_{hys}$ also covers a broad range from 0 to 90 K in this study. It is interesting to notice that in the phase diagram the largest hysteresis was found when Fe:Mn = 1:1, corresponding to a full occupancy of the *3g* site by Mn and the
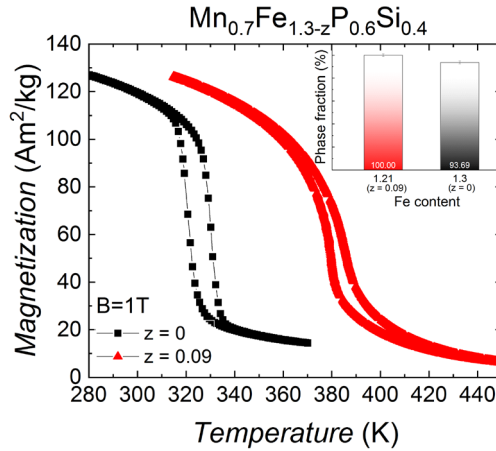
**Figure 3.5:** Magnetisation as a function of temperature of $Mn_{0.7}Fe_{1.3-z}P_{0.6}Si_{0.4}$ for $z = 0$ and $z = 0.09$ measured at an applied magnetic field of 1 T. The phase fraction of the main $Fe_2P$ type phase from the X-ray diffraction data is shown in the inset.

*3f* site by Fe. The thermal hysteresis decreases with decreasing Fe, Mn or P content, respectively. However, the thermal hysteresis of the $Mn_xFe_{2-x}P_{1-y}Si_y$ compounds is further tuneable by optimising the stoichiometry [11]. By optimising the stoichiometry, the Curie temperature $T_C$ and the thermal hysteresis $T_{hys}$ can change significantly. As shown in Figure 3.5, in $Mn_{0.7}Fe_{1.3-z}P_{0.6}Si_{0.4}$ a change in the Fe content from 1.30 ($z = 0$) to 1.21 ($z = 0.09$), the transition temperature increases by 52 K, and the thermal hysteresis decreases by 10 K. These changes are caused by a variation in the amount of impurity phase [12]. The impurity phase can be easily removed when the composition is optimised close to the optimal stoichiometry, accompanying with $T_C$ shifts to high temperature. Considering this experience, it is better to start synthesis a compound with lower $T_C$ than desired. The material without impurity phase in the desired working temperature range can be approached.

### 3.3.2.2 Unstable compositions

There is an area in the phase diagram marked as 'Unstable'. Figure 3.6 shows examples of *M-T* curves in the unstable region for $Mn_xFe_{2-x}P_{1-y}Si_y$ with $x = 1.1 - 1.9$, $y = 0.33$ and $x = 1.6$, $y = 0.4$. These samples generally show more than one magnetic transition, or they undergo an antiferromagnetic transition from the paramagnetic state instead of a ferromagnetic transition. These transitions cannot
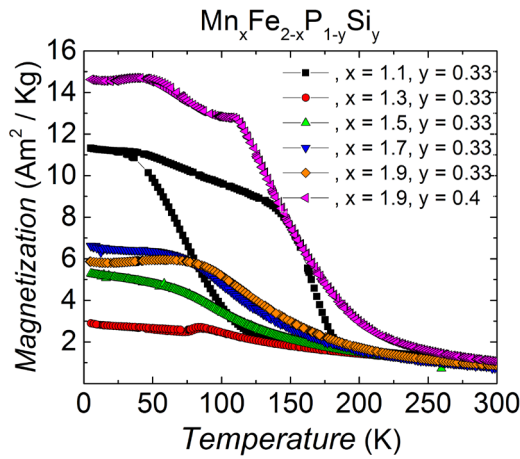
**Figure 3.6:** Magnetisation as a function of temperature for $Mn_xFe_{2-x}P_{1-y}Si_y$ samples in the 'unstable' zone (measured in an applied magnetic field of 1 T)

be used in application for magnetic refrigerators nor for thermomagnetic motors. Therefore, they are not studied further.

### 3.3.2.3 Latent heat and thermal hysteresis as a function of structural parameters

When the latent heat and thermal hysteresis (Figure 3.4(b)) are compared to the $c/a$ ratio (Figure 3.3(c)) of the lattice parameters for the $Fe_2P$ type hexagonal main phase of the $Mn_xFe_{2-x}P_{1-y}Si_y$ system a clear correlation is observed. As shown in Figure 3.7, a second-order magnetic transition without latent heat and hysteresis is observed for $c/a<0.560$ and a first-order magnetic transition with a latent heat and hysteresis is found for $c/a > 0.572$. A cross-over region is observed for $0.560 < c/a < 0.572$.
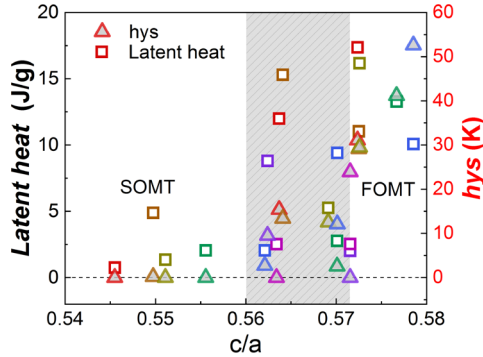
**Figure 3.7:** Latent heat and thermal hysteresis as a function of *c/a* ratio of the lattice parameters for the Fe$_2$P type hexagonal main phase of the Mn$_x$Fe$_{2-x}$P$_{1-y}$Si$_y$ system.

### 3.3.3 Suitable materials for magnetic energy conversion applications

The experimental structural and magnetic phase diagrams allow us to identify proper candidates for magnetic energy conversion applications in a thermomagnetic motor. The current working temperature range of the thermomagnetic motor is between 20°C (293 K) and 60°C (333 K) with an optimal $T_C$ of 40°C (313 K). Based on this working range, contour lines can be drawn in the phase diagram for $T_C$, and duplicate them at the same positions in the phase diagram for the thermal hysteresis. The obtained information on the transition temperature and thermal hysteresis are summarised in Figure 3.8.

For each temperature, the hysteresis increases with increasing Mn and Si concentration. Then, the hysteresis drops after it reaches a peak for a Mn content of $x \approx 1.0$ and a Si content of y $\approx 0.45$. Promising candidates can only be found in the grey area in Figure 3.8, which correspond to the Fe-rich/P-rich part (Mn: $x < 0.7$, Si: y < 0.4) and Mn-rich/Si-rich part (Mn: $x > 1.1$, Si: $y > 0.5$) of the phase diagram.
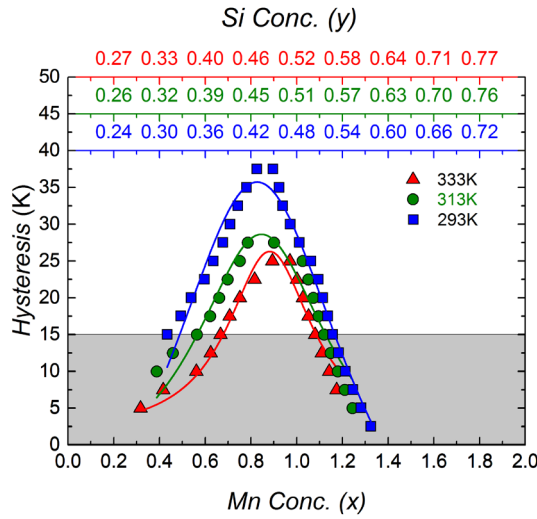
**Figure 3.8:** Concentration dependence of the thermal hysteresis in the $Mn_xFe_{2-x}P_{1-y}Si_y$ system for a transition temperature $T_C$ of 293, 313 and 333 K. The points correspond to the interpolated data in the phase diagram. The blue and red symbols and lines mark the lower and upper-temperature limit of the optimal cycling range between 20°C (293 K) and 60°C (333 K) of the current thermomagnetic motor. The green symbols and line marks the optimal $T_C$ of 40°C (313 K).

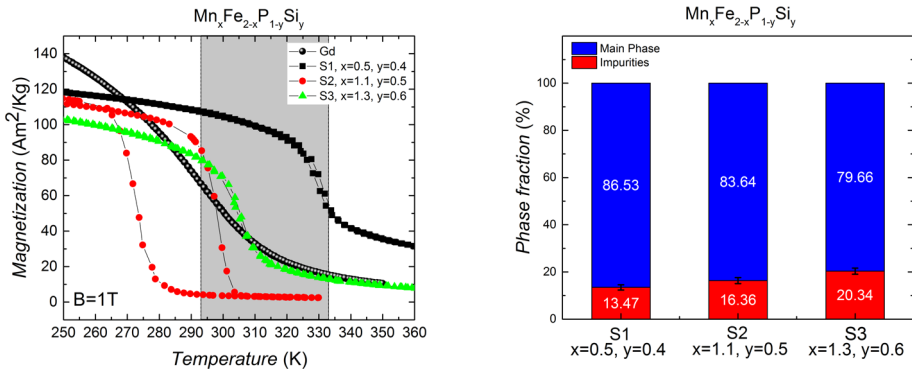

(a)                (b)

**Figure 3.9:** (a) Magnetisation as a function of temperature of promising candidates in the $Mn_xFe_{2-x}P_{1-y}Si_y$ system in an applied magnetic field of 1 T compared with (b) the phase fractions of the main phase and the impurity phase obtained from X-ray diffraction measurements. The grey area is the suitable temperature range for the thermomagnetic motor (TMM).

### 3.3.4 Examples of promising candidates

Three samples ($Mn_{0.5}Fe_{1.5}P_{0.6}Si_{0.4}$, $Mn_{1.1}Fe_{0.9}P_{0.5}Si_{0.5}$, $Mn_{1.3}Fe_{0.7}P_{0.4}Si_{0.6}$) were prepared using the guidance of the phase diagram. The results show that the transition temperature is in the desired range (Figure 3.9(a)). However, the hysteresis is more significant ($\Delta T_{hys}$ = 24 K) than expected for $Mn_{1.1}Fe_{0.9}P_{0.5}Si_{0.5}$. According to XRD data, the phase fraction of the main phase is smaller than 90% for all three samples (Figure 3.9(b)). This means that either the fabrication method or the stoichiometry of the material has to be optimised to achieve the desired properties.

**3**

## 3.4 Conclusions

A full-range phase diagram of the $Mn_xFe_{2-x}P_{1-y}Si_y$ system has been established as a guide to finding suitable materials for energy conversion applications in a thermomagnetic motor. Both Mn-rich samples and Fe-rich samples with a low Si concentration were found to show a low hysteresis that can form promising candidates for applications in a thermomagnetic motor. A reduction of the impurity phase by optimising the stoichiometry is an important step to further reduce the thermal hysteresis.

## References

1.  Gschneidner, K.A., V.K. Pecharsky, and AO. Tsokol, *Recent developments in magnetocaloric materials.* Reports on Progress in Physics, 2005. **68**: p. 1479-1539.

2.  Weiss, P. and A. Piccard, *Le phénomène magnétocalorique.* J. Phys. Theor. Appl., 1917. **7**: p. 103 - 109.

3.  Tegus, O., et al., *Transition-metal-based magnetic refrigerants for room-temperature applications.* Nature, 2002. **415**: p. 150-152.

4.  Hu, F., et al., *Influence of negative lattice expansion and metamagnetic transition on magnetic entropy change in the compound $LaFe_{11.4}Si_{1.6}$.* Applied Physics Letters, 2001. **78**: p. 3675-3677.

5.  Krenke, T., et al., *Inverse magnetocaloric effect in ferromagnetic Ni-Mn-Sn alloys.* Nature Materials, 2005. **4**: p. 450-454.

6.  Nguyen H. Dung, et al., *Mixed Magnetism for Refrigeration and Energy Conversion.* Advanced Energy Materials, 2011. **1**: p. 5.

7.  Rodriguez-Carvajal, J., *Abstract Satelite Meeting on Powder Diffraction.* Congr. Int. Union of Crystallography. Toulouse: France, 1990.

8.  Höglin, V., et al., *Phase diagram, structures and magnetism of the $FeMnP_{1-x}Si_x$ system.* RSC Advances, 2015. **5**: p. 8278-8284.

9.  Miao, X.F., et al., *Tuning the magnetoelastic transition in $(Mn,Fe)_2(P,Si)$ by B, C, and N doping.* Scripta Materialia, 2016. **124**: p. 129-132.

10. Brück, E., et al., *A review on Mn based materials for magnetic refrigeration: Structure and properties.* International Journal of Refrigeration, 2008. **31**: p. 763-770.

11. Leif, L., et al., *First Order Magnetic Phase Transition in $Fe_2P$.* Physica Scripta, 1978. **17**: p. 39.

12. Zavadskii, E.A., LI. Medvedeva, and AE Filippov, *Specific character of metamagnetic transitions in Fe2P.* Journal of Magnetism and Magnetic

# FIRST and SECOND-ORDER PHASE TRANSITIONS in (Mn,Fe)₂(P,Si) ALLOYS

# 4
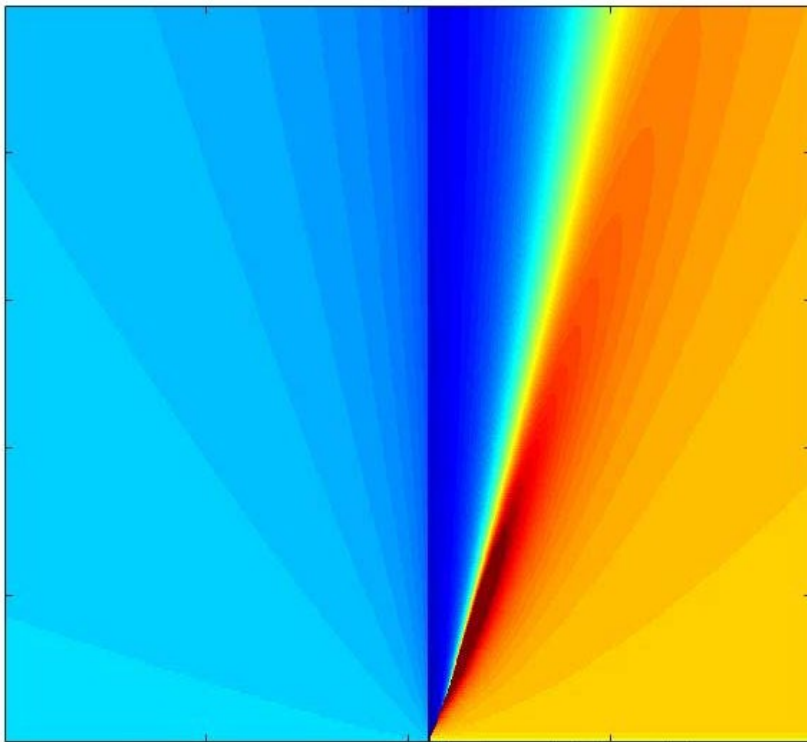
## 4.1 Introduction

Magnetocaloric materials (MCMs) show great potential for utilisation in magnetic refrigeration and magnetic energy conversion. A suitable MCM should have a significant magnetisation change and entropy change in a narrow working temperature window, a limited latent heat (for energy conversion applications) and a small change in lattice parameters (for stable mechanical properties). The significant change in magnetisation and entropy in a small temperature window is a typical first-order characteristic [1], while the limited latent heat and a small change in lattice parameters correspond to a second-order characteristic [2]. These conflicting demands inspire a fundamental study of the nature of the magnetic phase transition.

The classic way to describe the first-order magnetic phase transition (FOMT) and the second-order magnetic phase transition (SOMT) is based on the Landau model [3-5] or the Bean and Rodbell model[6]. In these models, the FOMT is distinguished from the SOMT by the presence of latent heat. Recently, a new criterion was proposed by Jia Yan Law et al. [7]. In this paper, the most popular ways to distinguish the order of the phase transition are listed and compared.

## 4.2 Methods

Polycrystalline samples of $Mn_xFe_{2-x}P_{1-y}Si_y$ have been prepared by ball milling starting materials of Fe (99.9%), Mn (99.9%), red-P (99.7%), and Si (99.9%) powder. After 10 h of ball milling, the samples were pressed into tablets [1]. The tablets were sealed under Ar atmosphere in quartz ampoules, sintered at 1373 K for 25 h, and then quenched into water.

Microstructures were analysed with a scanning electron microscope (JEOL JSM 6500F) equipped with an Autrata back-scattered electron (BSE) detector and coupled with energy disperse X-ray spectroscopy (EDS). Micrographs were taken with an electron beam energy of 15 keV. The phase fraction (area fraction) was obtained by ImageJ [8, 9].

X-ray powder diffraction patterns were collected in a PANalytical X-pert Pro diffractometer with Cu $K_\alpha$ radiation. The lattice parameters and the impurity phases are obtained by a full Rietveld refinement of the X-ray diffraction data using the FULLPROF package [10]. The heat capacity and latent heat were measured in a differential scanning calorimeter (DSC). The measurements were carried out by a

TA-Q2000 DSC, which uses liquid nitrogen to cool the system. The sweeping rate was 10 K/min.

Magnetic properties were measured in a SQUID (Superconducting Quantum Interference Device) magnetometer using the RSO mode in the low-temperature range (5 - 370 K). From the magnetic properties measurements, the Curie temperature $T_C$ and the thermal hysteresis $\Delta T_{hys}$ can be calculated.

Transmission $^{57}$Fe Mössbauer spectra were collected at 400 K with a conventional constant-acceleration spectrometer and at 4.2 K with a sinusoidal velocity spectrometer, using a $^{57}$Co(Rh) source. A velocity calibration was carried out using an α-Fe foil at room temperature. The source and the absorbing sample were kept at the same temperature of 4.2 K during the measurements. The Mössbauer spectra were fitted using the Mosswinn 4.0 program [11]. The spectra were fitted with a binomial distribution model, as previously described for the analysis of the Mossbauer spectra of the FeMnP$_{1-x}$As$_x$ compounds [12].

## 4.3 Results and discussions

### 4.3.1 Sample properties

#### 4.3.1.1 Structural and microstructural characterization

Figure 4.1 (a) shows the phase fractions in the Mn$_{1.3}$Fe$_{0.7}$P$_{1-y}$Si$_y$ ($y$ = 0.4, 0.5, 0.6) compounds. All samples predominantly consist of the hexagonal Fe$_2$P-type (space group *P-62m*) main phase. The impurities increase with increasing Si content,
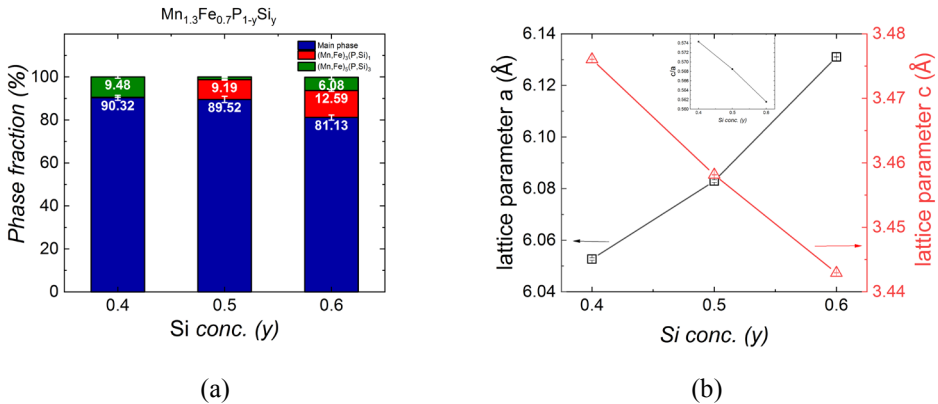


(a)                                     (b)

*Figure 4.1:* Phase fraction (a) and lattice parameters *a* and *c* of the hexagonal main phase (b) of the Mn$_{1.3}$Fe$_{0.7}$P$_{1-y}$Si$_y$ alloys. The *c/a* ratio is shown in the inset.

which is in good agreement with the previous report [13]. The change in lattice parameter versus the silicon concentration is shown in Figure 4.1(b). With increasing silicon concentration, the lattice parameter *a* expands, while lattice parameter *c* shrinks, and the *c*/*a* ratio reduces.

In Figure 4.2 the scanning electron microscopy (SEM) image for back scattered electrons (BSE) is shown for the $Mn_{1.3}Fe_{0.7}P_{0.6}Si_{0.4}$ sample. The black spots in the BSE image correspond to pores that may form during powder pressing into tablets and then remain in the system after the sample processing. The light and dark regions in the BSE image indicate different phases. Based on the EDX results, the dark region indicates the $Mn_{1.3}Fe_{0.7}P_{1-y}Si_y$ main phase and the light region corresponds to the $(Mn,Fe)_3(P,Si)_1$ impurity phase.

The phase fractions can be obtained by calculating the area fractions in the SEM image using ImageJ. The phase fraction given by XRD Rietveld refinement result refers to the weight fraction, which can be translated in the volume fraction. Table 4.1 shows the phase fraction obtained by the two different characterisation methods. The phase fraction obtained by both methods shows reasonable agreement. The advantage of the SEM analysis is that it allows the porosity to be observed. If the sample is too brittle to be polished, then it's hard to get a clear view and distinguish the different phases. The $Mn_{1.3}Fe_{0.7}P_{0.4}Si_{0.6}$ sample was found to be difficult to analyse as the grain boundaries were difficult to be distinguished.



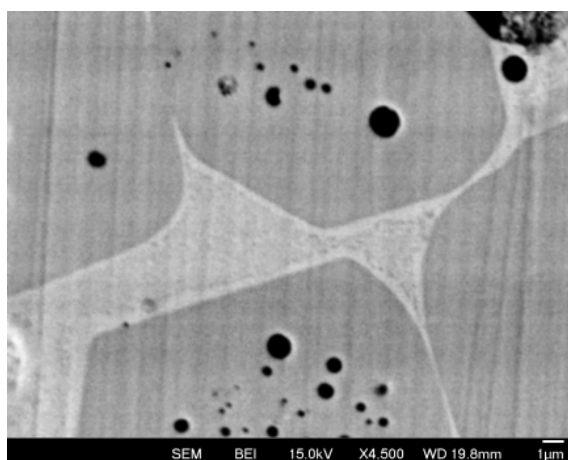***Figure 4.2:*** SEM micrograph of the $Mn_{1.3}Fe_{0.7}P_{0.6}Si_{0.4}$ sample.

### 4.3.1.2 Mössbauer Spectroscopy

The Mössbauer spectra measured at 4.2 and 400 K for three samples are shown in

**Table 4.1:** Comparison of phase fractions obtained by XRD and SEM.

| Sample | Method | Main phase Material fraction (%) | Impurity phase Material fraction (%) | Porosity fraction (%) |
|---|---|---|---|---|
| $Mn_{1.3}Fe_{0.7}P_{0.6}Si_{0.4}$ | XRD | $88.2 \pm 1.6$ | $11.8 \pm 0.7$ | - |
| | SEM | 80.3 | 19.7 | 1.5 |
| $Mn_{1.3}Fe_{0.7}P_{0.5}Si_{0.5}$ | XRD | $88.3 \pm 1.9$ | $11.7 \pm 0.4$ | - |
| | SEM | 78.1 | 21.9 | 3.7 |
| $Mn_{1.3}Fe_{0.7}P_{0.4}Si_{0.6}$ | XRD | $79.2 \pm 1.7$ | $20.8 \pm 1.2$ | - |
| | SEM | * | * | 5.2 |

*The phase fraction from SEM analysis for $Mn_{1.3}Fe_{0.7}P_{0.4}Si_{0.6}$ sample was not included because the grain boundaries were difficult to be distinguished.*

In the ferromagnetic (FM) low-temperature state (Figure 4.3 (a)), a complex absorption profile that exhibits six broad spectral lines is observed. These spectral lines indicate a hyperfine field distribution, resulting from varying distribution of neighbouring atoms around the Fe atom. Since P and Si atoms are randomly distributed on the 2*c* and the 1*b* crystallographic sites, this leads to five inequivalent Fe nearest neighbours. The experimental Mössbauer spectra are usually fitted with a model that weighs the contribution of each Fe environment using a binomial distribution[12]. In the paramagnetic (PM) high-temperature phase, a single broad absorption line is observed (Figure 4.3 (b)). A summary of the derived average hyperfine parameters, together with the linewidth and the fraction of the magnetic phase, is given in Table 4.2.
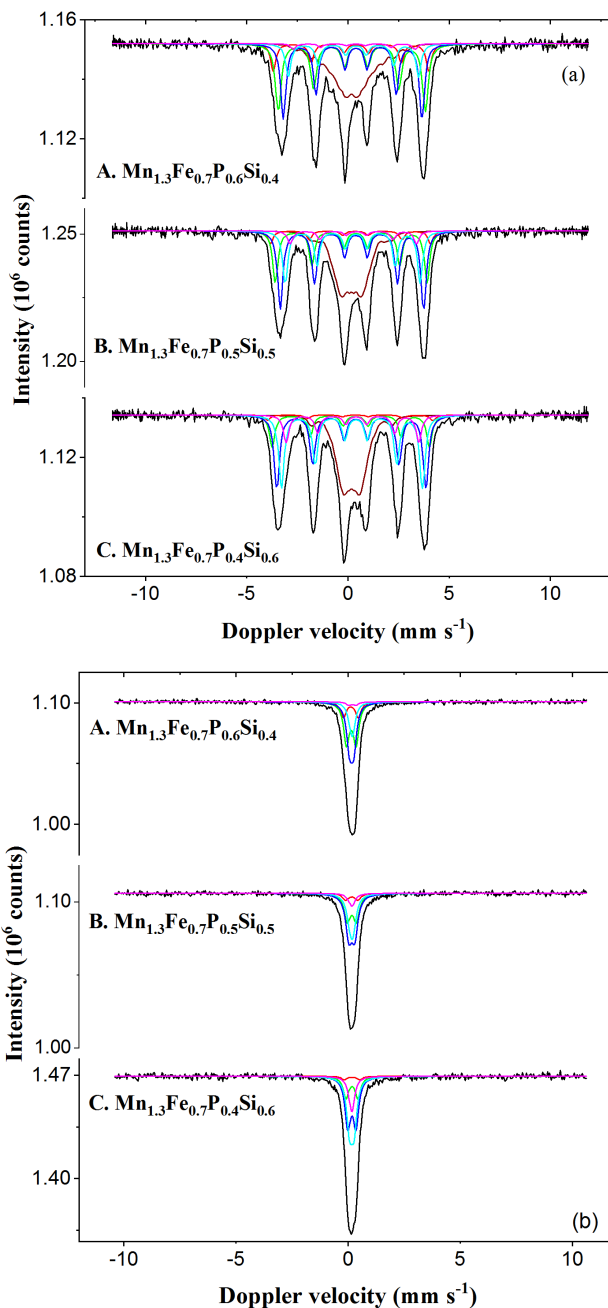
**Figure 4.3:** Mössbauer spectra obtained for the magnetocaloric $Mn_{1.3}Fe_{0.7}P_{1-y}Si_y$ samples in the ferromagnetic state at 4.2 K (a) and in the paramagnetic state at 400 K (b).

At a temperature of 4.2 K, all samples are in the ferromagnetic state. Surprisingly, $Mn_{1.3}Fe_{0.7}P_{0.6}Si_{0.4}$ shows a broadened singlet contribution, while the other samples show a narrow singlet contribution. Considering that this sample has the lowest $T_C$, this may be due to the presence of the metastable spin-density wave (SDW), observed in samples with a low $T_C$ that demonstrate an incomplete FM phase transition [14]. The paramagnetic state of the Si0.5 and Si0.6 samples may be due to the presence of a diamagnetic contribution, as revealed by recent [55]Mn NMR data. [15] The hyperfine field increases with increasing Si concentration. This is because the impurities have a higher hyperfine field compared to the main phase. An increase in the impurity concentration directly results in an increase in the hyperfine field. [12, 16, 17]

**4**

**Table 4.2:** Fitted Mössbauer parameters of the magnetocaloric $Mn_{1.3}Fe_{0.7}P_{1-y}Si_y$ samples measured at temperatures of 4.2 and 400 K.

| Sample | T (K) | IS* (mm·s⁻¹) | QS* (mm·s⁻¹) | Hyperfine field* (T) | Γ (mm·s⁻¹) | Phase | Spectral contribution (%) |
|---|---|---|---|---|---|---|---|
| Si0.4 | 400 | 0.15 | 0.27 | - | 0.30 | P | 100 |
| | 4.2 | 0.30 | -0.18 | 21.8 | 0.32 | F | 74 |
| | | 0.18 | - | 7.7 | 0.32 | SDW | 26 |
| Si0.5 | 400 | 0.17 | 0.26 | - | 0.34 | P | 100 |
| | 4.2 | 0.32 | -0.17 | 22.0 | 0.31 | F | 73 |
| | | 0.18 | - | 5.5 | 0.31 | SDW | 27 |
| Si0.6 | 400 | 0.17 | 0.29 | - | 0.30 | P | 100 |
| | 4.2 | 0.28 | -0.21 | 22.4 | 0.33 | F | 72 |
| | | 0.18 | - | 4.8 | 0.33 | SDW | 27 |

*Experimental uncertainties: Isomer shift: I.S. ± 0.01 mm s⁻¹; Quadrupole splitting: Q.S. ± 0.01 mm s⁻¹; Line width: Γ ± 0.01 mm s⁻¹; Hyperfine field: ± 0.1 T; Spectral contribution: ± 3%; F/P: ferromagnetic/paramagnetic phases;  ; SDW: Spin-density wave phase.*

### 4.3.1.3 Magnetic properties

The temperature dependent the magnetisation of the $Mn_{1.3}Fe_{0.7}P_{1-y}Si_y$ ($y = 0.4, 0.5, 0.6$) compounds measured in an applied magnetic field of 1 T is plotted in Figure 4.4 (a).For comparison, the temperature dependence of the magnetisation of gadolinium is also shown.  In Figure 4.4 (b) the corresponding values of $T_C$ and the thermal hysteresis $\Delta T_{hys}$ are plotted for the (Mn,Fe)₂(P,Si) compounds. All three
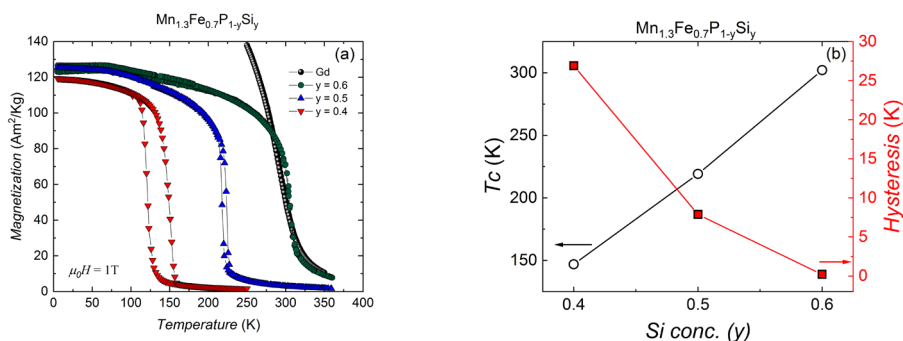
**Figure 4.4:** Magnetisation as a function of temperature in an applied magnetic field of $\mu_0 H = 1$ T (a) together with the derived Curie temperature $T_C$ and the thermal hysteresis $\Delta T_{hys}$ as a function of the Si content (b) for the $Mn_{1.3}Fe_{0.7}P_{1-y}Si_y$ ($y = 0.4,\ 0.5,\ 0.6$) compounds from M-T measurement in 0.01 T external field.

**4**

samples undergo a ferromagnetic (FM) – paramagnetic (PM) phase transition. The transition temperature increases roughly linear with increasing Si concentration. However, the hysteresis decreases rapidly. The thermal hysteresis for the $Mn_{1.3}Fe_{0.7}P_{0.4}Si_{0.6}$ samples is negligible.

### 4.3.2  Order of the magnetic phase transition

There are several ways to identify the nature of the magnetic transition as a FOMT, SOMT or critical point (CP). Based on the magnetisation data, the easiest and most intuitive way to define the order of transition is by the rapid increase in magnetisation and by the hysteresis. For instance, in Figure 4.4, the conclusion can be easily drawn that the $Mn_{1.3}Fe_{0.7}P_{0.6}Si_{0.4}$ is a FOMT material due to the sharp transition and large hysteresis. Sometimes, the answer is not straightforward for cases with a small thermal hysteresis, as this does not exclude a FOMT. Besides analysing the magnetisation data, there are several other ways to determine the order of the magnetic phase transition, as will be discussed in the following sections.

### 4.3.2.1 Temperature evolution of the XRD patterns

Figure 4.5 depicts the evolution of X-ray diffraction patterns with temperature in the 2θ range of 39 - 46º for the $Mn_{1.3}Fe_{0.7}P_{1-y}Si_y$ compounds with $y = 0.5$ (a) and $y = 0.6$ (b) in the temperature range of $T_C \pm 50$ K recorded upon heating. The
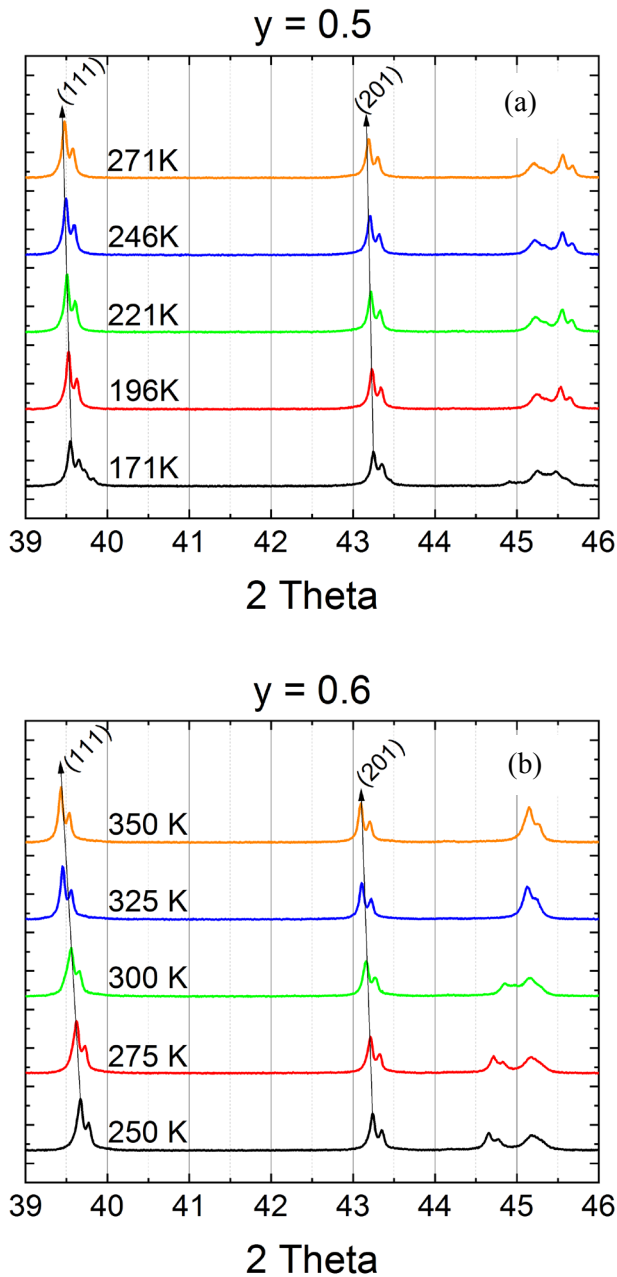
**Figure 4.5:** X-ray diffraction patterns of Mn$_{1.3}$Fe$_{0.7}$P$_{1-y}$Si$_y$ recorded at different temperatures for (a) $y = 0.5$ and (b) $y = 0.6$. The lines indicate the (111) and (201) peak positions before and after the magnetic phase transition.

$Mn_{1.3}Fe_{0.7}P_{0.6}Si_{0.4}$ sample wasn't included as the available temperature range was insufficient to cool down to $T_C$ - 50 K for $Mn_{1.3}Fe_{0.7}P_{0.6}Si_{0.4}$. Within the $T_C \pm 50$ K temperature range, the $Mn_{1.3}Fe_{0.7}P_{1-y}Si_y$ samples with $y = 0.5$ and 0.6 undergo a FM-PM transition without a change in the crystal structure.

The lattice distortion can be seen as direct evidence of the nature of the transition. It can be simply judged from the temperature dependence of the XRD pattern, whether the position of the diffraction peaks changes continuously (SOMT) or discontinuously (FOMT) [18]. The (111) peak position indicates a discontinuous change at $T_C$ + 25 K for both samples. For the (201) peak position, the same behaviour is observed, which gives the impression that these two samples both undergo a FOMT. However, sometimes, the shift of peak position is very small, which makes it difficult to distinguish the nature of the transition (as the resolution may be insufficient). The temperature evolution of the lattice parameters can define the order of the magnetic transitions.

Generally, the thermal expansion of material can be positive, zero (Invar alloy, for instance[19, 20]), and negative (La(Fe,Si)$_{13}$ alloys[21]). In (Mn, Fe)$_2$(P,Si) alloy, there is a magneto-elastic transition for which the crystal structure remains unchanged but the lattice constants and the unit cell volume change at the magnetic transition.[22]

Figure 4.6 (a) shows the temperature dependence of the unit-cell volume for the $Mn_{1.3}Fe_{0.7}P_{1-y}Si_y$ ($y = 0.5$ and 0.6) compounds. In this $Mn_{1.3}Fe_{0.7}P_{1-y}Si_y$ compounds, the unit cell volume expands when the temperature increases. When the temperature is around $T_C$, some volume fluctuation in the crystal is observed, which indicate a two-phase coexistence of the FM and PM phases in the compounds. The temperature dependence of the lattice parameters for the Si0.5 and Si0.6 samples are shown in Figure 4.6 (b, c). The Si0.5 sample shows a gradual change in both $a$ and $c$ with a gap between the FM and PM state values and a phase coexistence at the transition temperature. The discontinuous change in the lattice parameters is a strong indication for a FOMT. Within the experimental resolution, the Si0.6 sample, however, shows a continuous change in both $a$ and $c$ between the FM and PM state values, suggesting a SOMT.
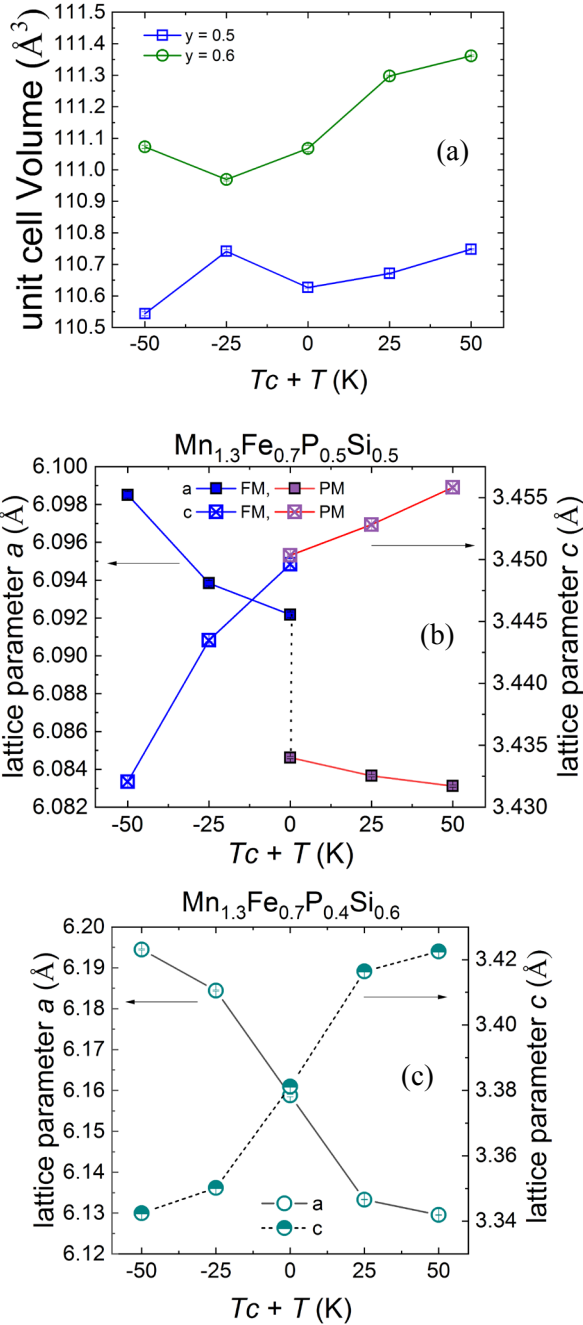
*Figure 4.6:* Temperature dependence of volume (a) and of the lattice parameters of Mn$_{1.3}$Fe$_{0.7}$P$_{0.5}$Si$_{0.5}$ (b) and Mn$_{1.3}$Fe$_{0.7}$P$_{0.4}$Si$_{0.6}$ (c), derived from X-ray diffraction patterns measured upon heating.

### 4.3.2.2 DSC pattern and latent heat

The latent heat of the magnetic phase transition can also reveal the order of phase transition. In principle, a FOMT is always associated with latent heat, while the SOMT is not. Figure 4.7 shows the temperature dependence of the specific heat of the $Mn_{1.3}Fe_{0.7}P_{1-y}Si_y$ ($y = 0.5$ and 0.6) compounds. These two samples both show a relatively large sharp peak. The latent heat can be obtained by integrating the peak area. The latent heat of the $Mn_{1.3}Fe_{0.7}P_{1-y}Si_y$ compounds is 4.72 and 4.58 (J g$^{-1}$) for $y = 0.5$ and 0.6, respectively. This suggests that both samples undergo a FOMT.

The disadvantage of this method is that it monitors the heat flow for the continuous evolution of temperature at a finite rate. However, the sample rejects or absorbs heat when it crosses the transition, which will result in a broadened peak in the specific heat. For a FOMT the associated latent heat is expected to be released at the transition temperature giving rise to a sharp peak. In contrast, for a SOMT, the specific heat is enhanced over a wider temperature range around the transition. The sharpness of the peak, however, generally depends on the rate at which the temperature is changed, and its evaluation depends on experience.
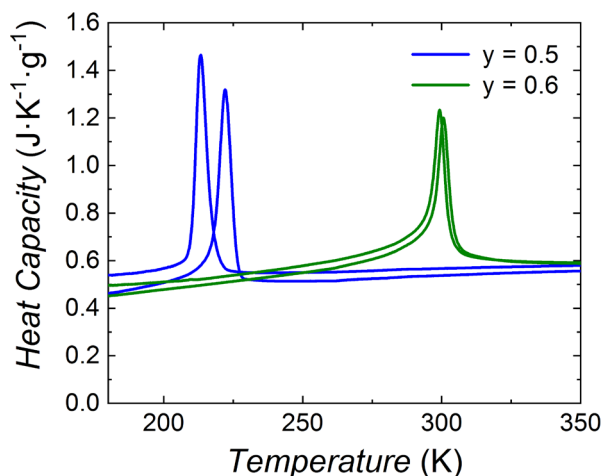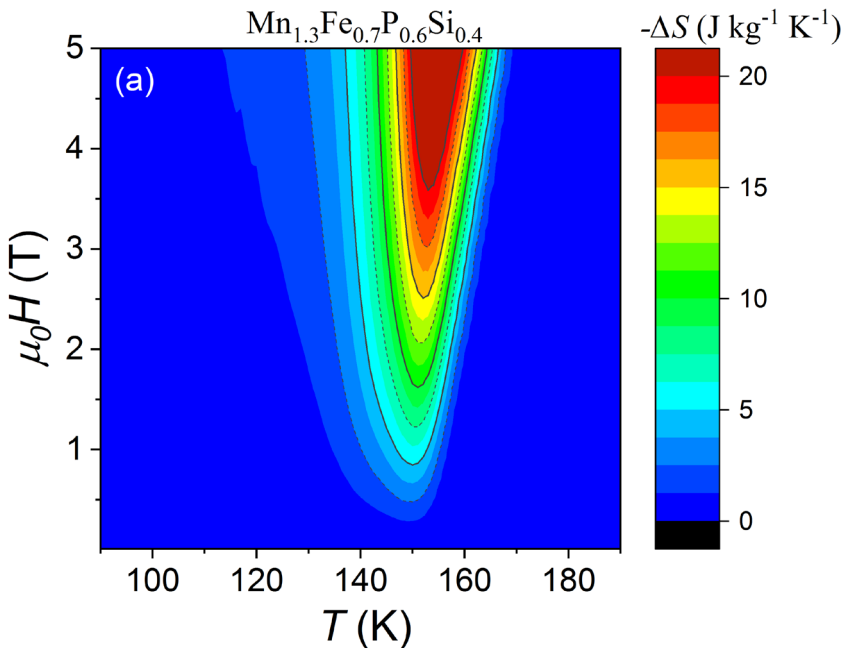


**Figure 4.7:** Temperature dependence of the specific heat of the $Mn_{1.3}Fe_{0.7}P_{1-y}Si_y$ ($y = 0.5$ and 0.6) compounds measured in zero fields upon cooling and heating.

### 4.3.2.3 Entropy change

Figure 4.8 shows a contour plot of the magnetic entropy change of the Mn$_{1.3}$Fe$_{0.7}$P$_{1-y}$Si$_y$ ($y$ = 0.4, 0.5, 0.6) alloys. Near $T_C$ the magnetic entropy change increases dramatically with fields for a FOMT sample, while the entropy changes gradually for SOMT sample. The Si0.4 sample shows a sudden change in a narrow window compared to the Si0.5 and Si0.6 samples. This also indicates that the Mn$_{1.3}$Fe$_{0.7}$P$_{0.6}$Si$_{0.4}$ sample is a FOMT sample. The Si0.5 sample also shows a sizeable change indicative for a FOMT behaviour, while the change is more gradual for the Si0.6 sample. The disadvantage of this method is the same as DSC measurements. In the cross-over region, it is not easy to distinguish the FOMT and SOMT samples.
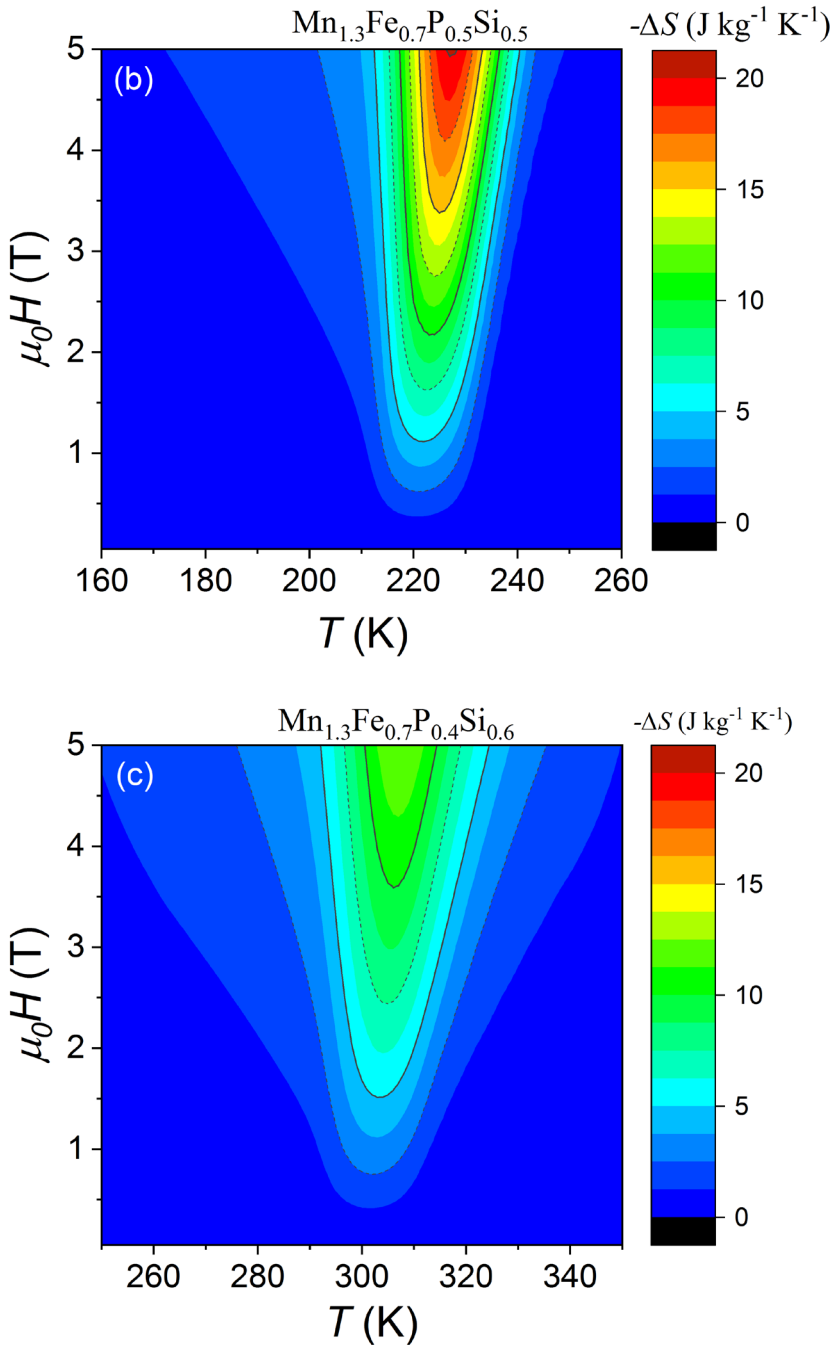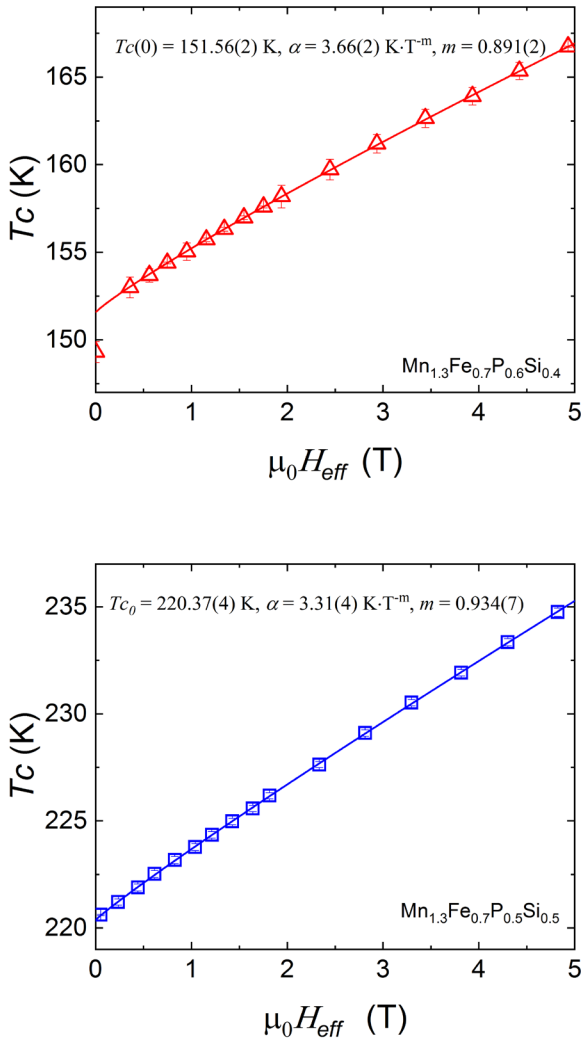
**4**

**4**



**Figure 4.8:** Magnetic entropy change of the $Mn_{1.3}Fe_{0.7}P_{1-y}Si_y$ ($y$ = 0.4, 0.5, 0.6) alloys.

### 4.3.2.4 Curie temperature

In Figure 4.9 the field dependence of the ferromagnetic transition temperature $T_C$ is shown. Experimentally it is found that the transition temperature in an applied magnetic field can be described as:

$$Tc\,(B) = Tc(0) + \alpha(\mu_0 H)^m$$

The field exponent for the transition temperature $m$ is in all cases slightly smaller than 1, and shows a limited variation for all three samples. This suggests that the field exponent is not very sensitive to the nature of the magnetic order.
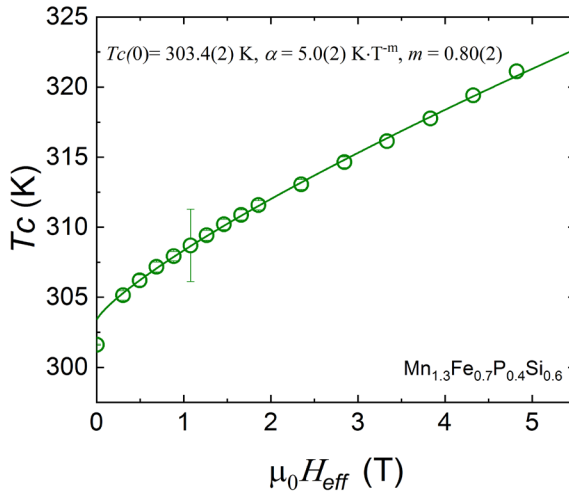


$Tc(0) = 151.56(2)$ K, $\alpha = 3.66(2)$ K·T$^{-m}$, $m = 0.891(2)$

Mn$_{1.3}$Fe$_{0.7}$P$_{0.6}$Si$_{0.4}$



$Tc_0 = 220.37(4)$ K, $\alpha = 3.31(4)$ K·T$^{-m}$, $m = 0.934(7)$

Mn$_{1.3}$Fe$_{0.7}$P$_{0.5}$Si$_{0.5}$

Plot with axes: $Tc$ (K) on vertical axis (ranging 300 to 325), $\mu_0 H_{eff}$ (T) on horizontal axis (0 to 5).

Annotation: $Tc(0)= 303.4(2)$ K, $\alpha = 5.0(2)$ K·T$^{-m}$, $m = 0.80(2)$

Sample label: $Mn_{1.3}Fe_{0.7}P_{0.4}Si_{0.6}$

**Figure 4.9:** Field dependence of the ferromagnetic transition temperature $T_C$. The field was corrected by the demagnetisation field.

### 4.3.2.5 Arrott plots

The isotherm Arrott plots in combination with the Banerjee criterion [23] ($H/M$ versus $M^2$) graphically represents the order of phase transition. This is based on the Landau model which will be discussed in the following paragraph. The Arrott plots can give information about the curie point where the line goes through the original point. The slope of Arrott plots reveals the order of transition. If the curve shows a negative slope ( S-shape), indicating the sample undergoes a FOMT, and if the curve shows a positive slope, indicates the sample undergoes a SOMT. In Figure 4.10 the Arrotts ($H/M$ versus $M^2$) for the Si0.4, Si0.5 and Si0.6 samples are shown. This graph also confirms that Si0.4 and Si0.5 samples undergo a FOMT, while in contrast to DSC and XRD results, the Si0.6 sample shows a SOMT.
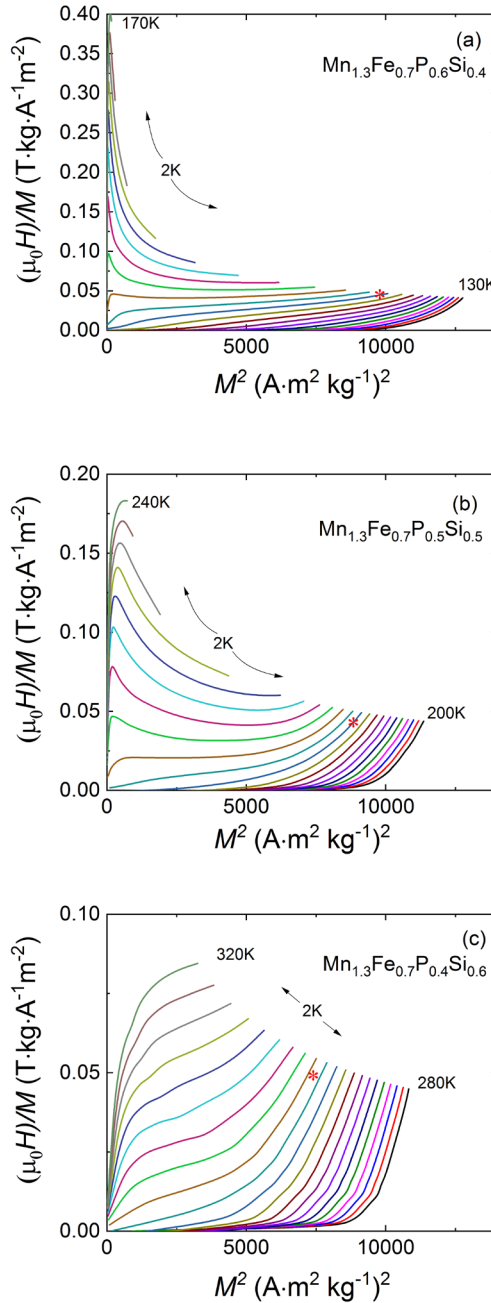
***Figure 4.10:*** Arrott plots for the $Mn_{1.3}Fe_{0.7}P_{1-y}Si_y$ ($y$ = 0.4, 0.5 and 0.6) samples. The field was corrected for the demagnetisation field. According to the Banerjee criterion, Si 0.4 and Si 0.5 samples undergo a FOMT, while Si 0.6 has a SOMT. * presents Tc for each sample.

### 4.3.2.6 Magnetic field exponent for the entropy change

An exponent criterion has been proposed recently [7] to identify the order of the magnetic transition. The field exponent *n* is defined as:

$$n = \frac{d \ln\left(|\Delta S|\right)}{d \ln\left(H\right)}$$

where $\Delta S$ is the entropy change and $\mu_0 H$ the applied magnetic field. If the exponent *n* has a maximum value bigger than 2 this indicates a FOMT; otherwise, it is a SOMT. Figure 4.11 shows the experimental results for *n*. It shows Si0.6 undergoes a SOMT, while Si0.4 and Si0.5 correspond to a FOMT. Besides the maximum value, the lowest value is interesting to note. The lowest value for the $Mn_{1.3}Fe_{0.7}P_{1-y}Si_y$ alloys are 0.32, 0.31 and 0.5 for $y = 0.4$, 0.5 and 0.6, respectively.
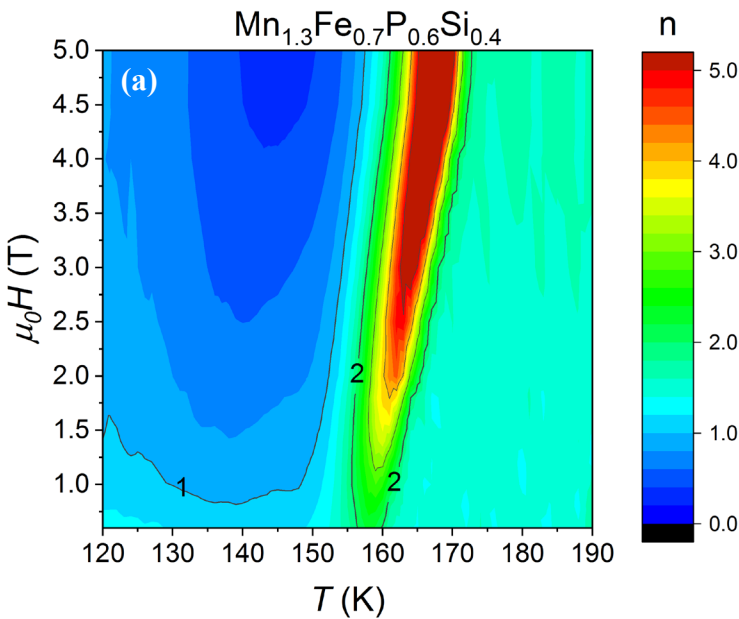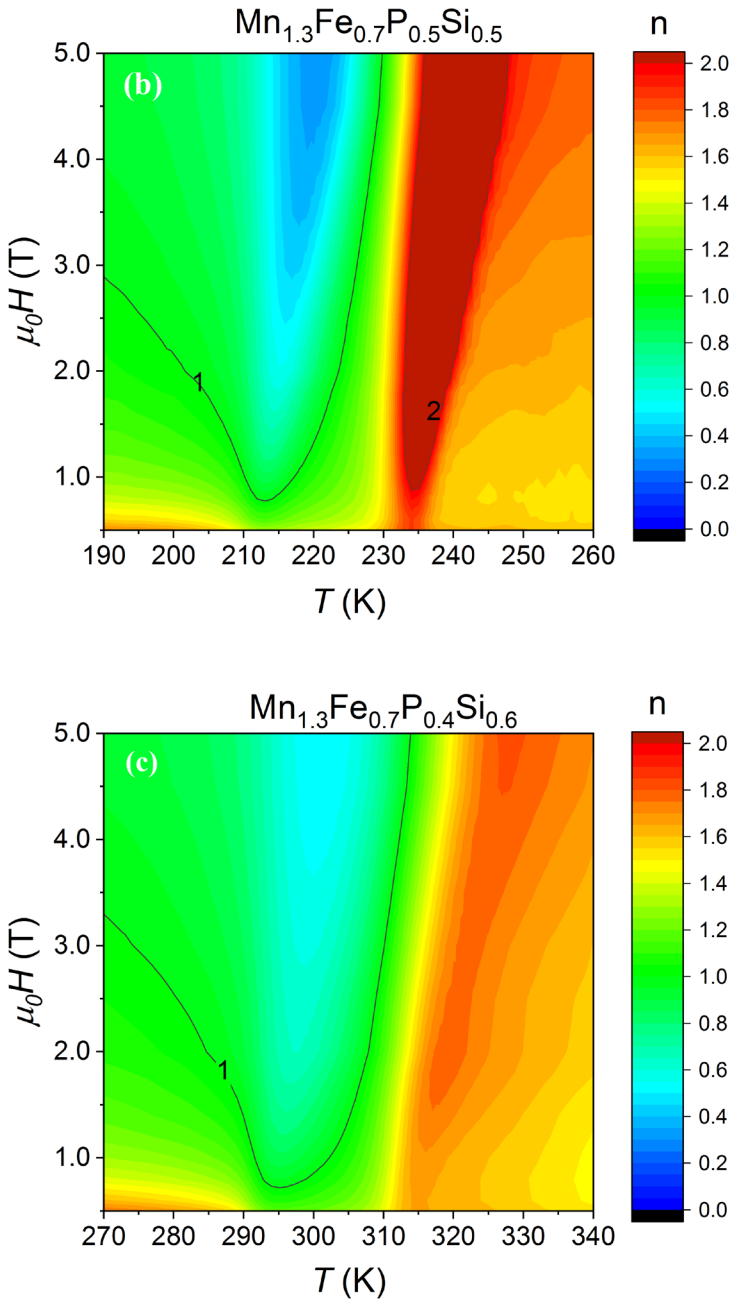
**Figure 4.11:** Field and temperature dependence of the field exponent $n$ of the entropy change for the $Mn_{1.3}Fe_{0.7}P_{1-y}Si_y$ ($y = 0.4, 0.5, 0.6$) alloys.

### 4.3.2.7 Landau model

The Landau model [3, 4]is an approach to describe the Gibbs free energy of a magnetic system close to the phase transition temperature ($T_C$). Depending on the model parameters, it can show a continuous (SOMT) or a discontinuous (FOMT) transition. This provides a way to investigate the nature of the transition. Therefore, many investigations are based on the Landau theory.

In the Landau model the change in Gibbs free energy $\Delta G$ from the unordered paramagnetic state to the magnetically ordered state is described in terms of the order parameter, which is the magnetisation $M$ :

$$\Delta G = \frac{\alpha}{2} M^2 + \frac{\beta}{4} M^4 + \frac{\gamma}{6} M^6 - \mu_0 HM$$

where $\mu_0 H$ is the applied magnetic field. In the vicinity of the magnetic transition with a characteristic temperature, $T_0$ one can assume $\alpha = \alpha_0 (T - T_0)$ , where $\alpha_0 > 0$ , $\beta$ and $\gamma \geq 0$ are constants. Depending on the value of $\beta$ one now finds three different types for the ferromagnetic transition: (i) a first-order phase transition (FOMT) for $\beta < 0$ , (ii) a second-order phase transition (SOMT) for $\beta > 0$ and (iii) a critical point (CP) for $\beta = 0$ . A minimisation of $\Delta G$ to the order parameter $M$ results in the equation of state:

$$\alpha M + \beta M^3 + \gamma M^5 = \mu_0 H$$

Using the Landau model the field exponents *n* of the entropy change are obtained. The results for the FOMT, CP and SOMT are shown in Figure 4.12. The diagrams for *n* are plotted as a function of the reduced temperature $t = (T - T_C)/T_C$ and the reduced magnetic field $h = H/H_0$ , where $H_0$ is a characteristic field that depends on the model parameters [ref]. The maximum value for the field exponent *n* corresponds to *n* > 2 for the FOMT near the transition, and *n* = 2 for the CP and SOMT in the paramagnetic state. The minimum value for the field exponent *n* corresponds to *n* = 0 for the FOMT, *n* = 2/5 for the CP and *n* = 2/3 for the SOMT at the transition temperature in zero field $T_C$ (*H* = 0).

The experimental maps of the field exponent for the entropy change *n* for the Si04, Si05 and Si06 samples in Figure 4.11 and the model predictions based on the Landau model of Figure 4.12  qualitatively show the same overall features. For the

Si0.4 and Si0.5 samples, the highest value corresponds to $n > 2$ and the lowest value to $n < 2/5$. This clearly confirms the FOMT nature of the transition in the Si0.4 and Si0.5 samples, where the Si0.4 has a higher maximum than Si0.5 and shows a more pronounced first-order character. For the Si0.6 sample the highest value corresponds to $n = 2$ and the lowest value to $2/5 < n < 2/3$. This indicates a SOMT nature of the transition with a proximity to the CP.
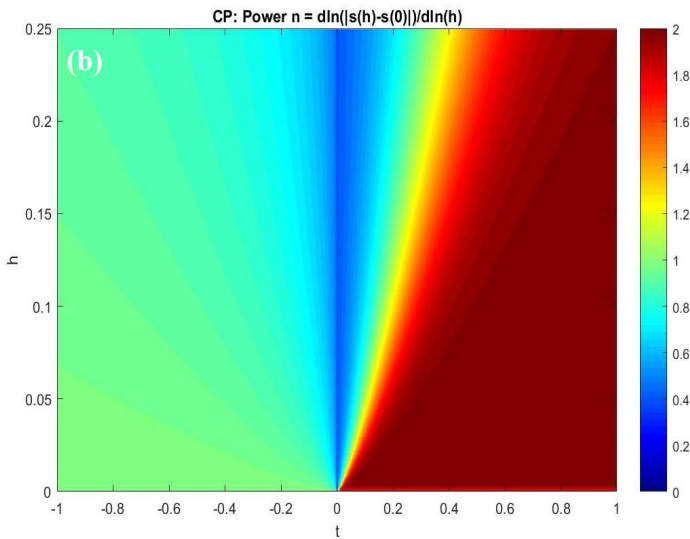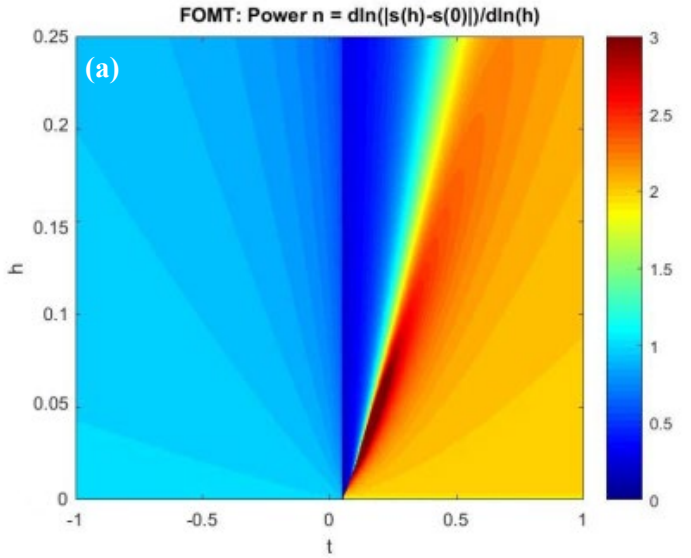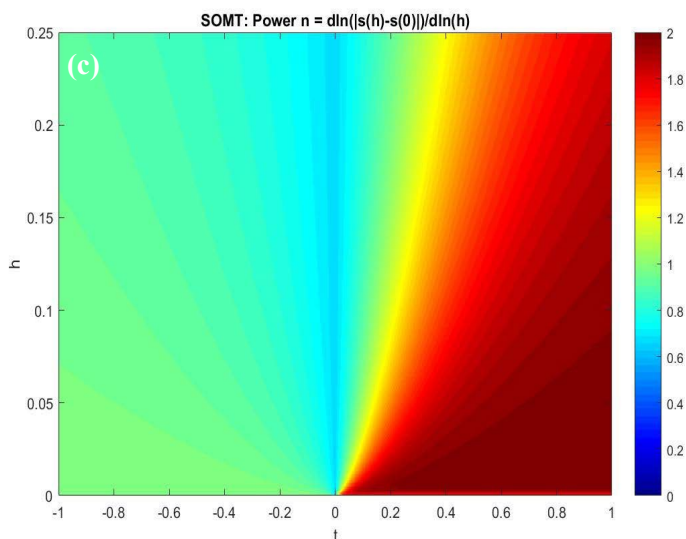
*Figure 4.12:* Field and temperature dependence of the exponent n for FOMT (a), critical points (b), SOMT (c).

## 4.4 Conclusions

In this chapter, the currently used methods to classify FOMT and SOMT materials were applied and compared. The Si0.4 and Si0.5 samples clearly classify as FOMT samples. For sample Si0.6, different criteria give a different conclusion. From the latent heat, the Si0.6 is predicted to undergo a FOMT. From the XRD data and the field dependence $T_C$, the Si0.6 sample is right on the CP. However, based on the Arrott plots, and the gradual field dependence for the entropy change and the newly proposed field exponent $n$, the sample is a SOMT material (but in close proximity to the CP).

# References

1. Nguyen H. Dung, et al., *Mixed Magnetism for Refrigeration and Energy Conversion.* Advanced Energy Materials, 2011. **1**: p. 5.

2. Singh, S., et al., *Large Magnetisation and Reversible Magnetocaloric Effect at the Second-Order Magnetic Transition in Heusler Materials.* Advanced Materials, 2016.

3. Landau, L.D., *On the theory of phase transitions.* Ukr. J. Phys., 1937. **11**: p. 19-32.

4. Uzunov, D.I., *Introduction to the theory of critical phenomena: mean field, fluctuations and renormalisation*. 1993: World Scientific.

5. Boeije, M.F.J., et al., *Mixed magnetism in magnetocaloric materials with first-order and second-order magnetoelastic transitions.* Journal of Physics D: Applied Physics, 2017. **50**: p. s.

6. Bean, C.P. and D.S. Rodbell, *Magnetic Disorder as a First-Order Phase Transformation.* Physical Review, 1962. **126**: p. 104-115.

7. Law, J.Y., et al., *A quantitative criterion for determining the order of magnetic phase transitions using the magnetocaloric effect.* Nature Communications, 2018. **9**: p. 2680.

8. Rasband, W.S., *ImageJ, U.S. National Institutes of Health, Bethesda, Maryland, USA.* http://imagej.nih.gov/ij/, 2011.

9. Schneider, C.A., W.S. Rasband, and K.W. Eliceiri, *NIH Image to ImageJ: 25 years of image analysis.* Nature Methods, 2012. **9**: p. 671-675.

10. Rodriguez-Carvajal, J., *Abstract Satelite Meeting on Powder Diffraction.* Congr. Int. Union of Crystallography. Toulouse: France, 1990.

11. Klencsár, Z., *Mössbauer spectrum analysis by Evolution Algorithm.* Nuclear Instruments and Methods in Physics Research Section B: Beam Interactions with Materials and Atoms, 1997. **129**: p. 527-533.

12. Hermann, R.P., et al., *Mössbauer spectral study of the magnetocaloric FeMnP₁₋ₓAsₓ compounds.* Physical Review B, 2004. **70**.

13. Höglin, V., et al., *Phase diagram, structures and magnetism of the FeMnP₁₋ₓSiₓ system.* RSC Advances, 2015. **5**: p. 8278-8284.

**4**

14. Miao, X.F., et al., *Kinetic-arrest-induced phase coexistence and metastability in(Mn,Fe)$_2$(P,Si).* Physical Review B, 2016. **94**.

15. Hussain, R., et al., *Ubiquitous first-order transitions and site-selective vanishing of the magnetic moment in giant magnetocaloric MnFeSiP alloys detected by $^{55}$Mn NMR.* Physical Review B, 2019. **100**.

16. Johnson, V., et al., *Magnetic and Mössbauer effect studies of Mn5Si3:Fe5Si3 solid solutions.* Journal of Solid State Chemistry, 1972. **4**: p. 311-323.

17. Al-Nawashi, G.A., et al., *Mössbauer spectroscopic study of order–disorder phenomena in Fe$_{3-x}$Mn$_x$Si.* Physica B: Condensed Matter, 2002. **321**: p. 167-172.

18. Maschek, M., et al., *Charge redistribution and the magnetoelastic transition across the first-order magnetic transition in (Mn,Fe)$_2$(P,Si,B).* Physical Review B, 2018. **98**.

19. Guillaume, C.E., *CR Acad. Sci.* 1897.

20. Mohn, P., *A century of zero expansion.* Nature, 1999. **400**: p. 18-19.

21. Huang, R., et al., *Giant negative thermal expansion in NaZn$_{13}$-type La(Fe,Si,Co)$_{13}$ compounds.* J Am Chem Soc, 2013. **135**: p. 11469-72.

22. Dung, N.H., et al., *From first-order magneto-elastic to magneto-structural transition in (Mn,Fe)$_{1.95}$P$_{0.50}$Si$_{0.50}$ compounds.* Applied Physics Letters, 2011. **99**.

23. Banerjee, B.K., *On a generalised approach to first and second order magnetic transitions.* Physics Letters, 1964. **12**: p. 16-17.

**4**

# Vanadium Substitution In Magnetocaloric $Mn_{0.7}Fe_{x-y}V_yP_{0.6}Si_{0.4}$ Alloys

# 5

## 5.1 Introduction

Magnetocaloric materials (MCMs) show great potential for utilisation in magnetic refrigeration and magnetic energy conversion. Magnetocaloric materials, like the Mn-Fe-P-based alloys, have been widely studied for their giant magnetocaloric effect (MCE) near room temperature. A material with the desired transition temperature, a large change in magnetisation at the working temperature range and a small thermal hysteresis is considered a promising candidate for both applications. A recent study shows that vanadium substitution of Mn in Mn-rich $Mn_{1.2}Fe_{0.75}P_{0.5}Si_{0.5}$ alloys results in a decrease in the thermal hysteresis and allows a tuning of the material towards a second-order magnetic phase transition (SOMT) [1, 2]. However, the effect of vanadium substitution in the Fe-rich alloys has not been studied so far. In order to reduce the cost of synthesis $Fe_2P$, obtained as a by-product in the refinement of Fe, is used as a starting material to synthesise the compounds.

## 5.2 Methods

Polycrystalline samples of $Mn_{0.7}Fe_{x-y}V_yP_{0.6}Si_{0.4}$ have been prepared by ball milling starting materials of Fe (99.9%), Mn (99.9%), Si (99.9%), V (99.9%), MnP [Fe (0.2%), Mn(62.9%), P (33.1%), Si(0.6%)], and $Fe_2P$ (92.5%) powder. After 10 h of ball milling, the samples were pressed into tablets [3]. The tablets were sealed under Ar atmosphere in quartz ampoules, sintered at 1373 K for 25 h, and then quenched into water.

Powder diffraction patterns were collected in a PANalytical X-pert Pro diffractometer with Cu $K_\alpha$ radiation. The lattice parameters and the impurity phases are obtained by a full Rietveld analysis of the X-ray diffraction data using the FULLPROF package [4]. The heat capacity and latent heat were measured in a differential scanning calorimeter (DSC). The DSC measurements were carried out using a TA-Q2000 DSC, which uses liquid nitrogen to cool the system. The sweeping rate was 10 K/min. From the DSC measurements, the magnetic transition temperature $T_C$ and the thermal hysteresis $\Delta T_{hys}$ can be calculated. In this work, $T_C$ and $\Delta T_{hys}$ were determined from the heating and cooling curves in zero fields.

The magnetic properties were measured in a SQUID (Superconducting Quantum Interference Device) magnetometer using the RSO mode in the low-temperature
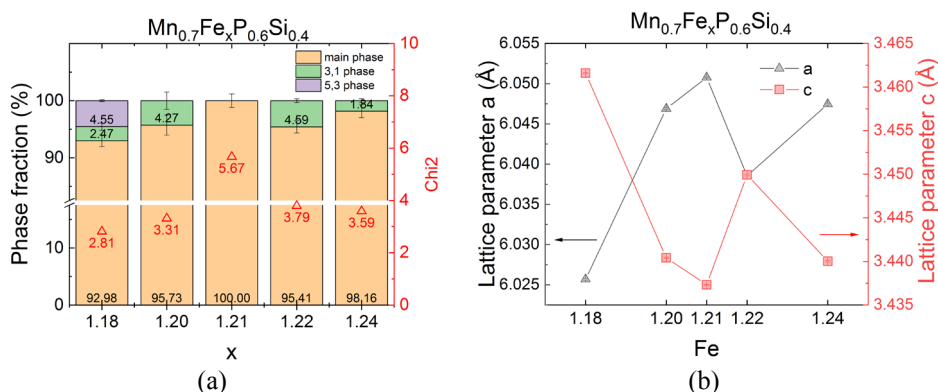
**Figure 5.1:** Phase fraction (a) and lattice parameters $a$ and $c$ (b) of the Mn$_{0.7}$Fe$_x$P$_{0.6}$Si$_{0.4}$ ($x$ = 1.18, 1.20, 1.21, 1.22, 1.24) compounds.

range (5 - 370 K) and a VSM (vibrating sample magnetometer) in the high-temperature range (300 - 600 K).

## 5.3 Results and discussions

### 5.3.1 Optimisation of the stoichiometry

To study the effect of vanadium substitution, first the Fe content is tuned to find a candidate material with a low thermal hysteresis and a low impurity phase fraction.

#### 5.3.1.1 X-ray diffraction

Figure 5.1 (a) shows the phase fraction of the Mn$_{0.7}$Fe$_x$P$_{0.6}$Si$_{0.4}$ ($x$ = 1.18, 1.20, 1.21, 1.22 and 1.24) compounds. All samples predominantly consist of the hexagonal Fe$_2$P-type (space group *P-62m*) main phase. The measurements indicate an impurity phase fraction below 10% for all samples. The main impurity phase is found to be (Mn,Fe)$_3$(P,Si)$_1$. The Mn$_{0.7}$Fe$_{1.18}$P$_{0.6}$Si$_{0.4}$ sample also shows the presence of the (Mn,Fe)$_5$(P,Si)$_3$ impurity phase. The Mn$_{0.7}$Fe$_{1.21}$P$_{0.6}$Si$_{0.4}$ sample has the lowest amount of impurity phase in the series. Figure 5.1 (b) shows how the variation in lattice parameter $a$ and $c$ of the hexagonal lattice structure as a function of the Fe content. The lattice parameter $c$ decreases with increasing Fe content until it reaches the lowest value (of 3.437 Å) when the Fe content is $x$ = 1.21. The lattice parameter $a$ shows the opposite trend compared to $c$. However, when the Fe content is higher than $x$ = 1.21, the lattice parameter $c$ fluctuates (between 3.440 and 3.450 Å).

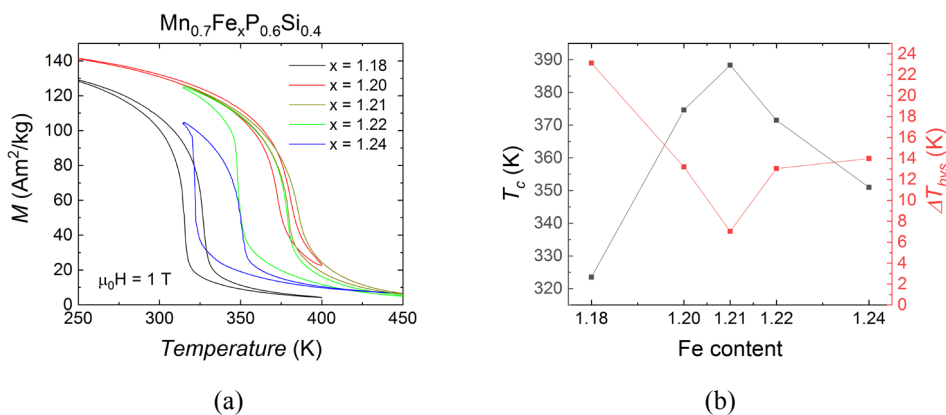(a)                                                            (b)

**Figure 5.2:** Magnetisation as a function of temperature in an applied magnetic field $\mu_0 H$ of 1 T (a) with the ferromagnetic transition temperature $T_C$ and the thermal hysteresis $\Delta T_{hys}$ as a function of the Fe content derived from DSC measurement in zero field (b) for the $Mn_{0.7}Fe_xP_{0.6}Si_{0.4}$ ($x = 1.18$, 1.20, 1.21, 1.22, 1.24) compounds.

### 5.3.1.2 magnetic properties

In Figure 5.2 the magnetic properties of the samples are shown with the magnetisation as a function of temperature and the evolution of the ferromagnetic transition temperature $T_C$ and the thermal hysteresis $\Delta T_{hys}$ as a function of the Fe content $x$. It is found that $T_C$ first increases with the increasing Fe content, until it reaches its highest value (at 382 K) when the Fe content is $x = 1.21$, and then decreases. In contrast, the hysteresis $\Delta T_{hys}$ first decreases and then increases. From the temperature dependence of the magnetisation curves, it is found that the $Mn_{0.7}Fe_{1.21}P_{0.6}Si_{0.4}$ sample shows the highest saturation magnetisation at low temperature among the $Mn_{0.7}Fe_xP_{0.6}Si_{0.4}$ ($x = 1.18$, 1.20, 1.21, 1.22, 1.24) compounds.

The $Mn_{0.7}Fe_{1.21}P_{0.6}Si_{0.4}$ sample ($x = 1.21$) was chosen as a starting material to achieve the highest saturation magnetisation with the lowest thermal hysteresis and the lowest impurity phase fraction.

### 5.3.2 Influence of vanadium on the Fe-rich samples

### 5.3.2.1 X-ray diffraction

In Figure 5.3, the phase fractions obtained from a refinement of the X-ray diffraction data of the vanadium substituted $Mn_{0.7}Fe_{1.21-y}V_yP_{0.6}Si_{0.4}$ compounds is shown. All samples consist predominantly of the hexagonal $Fe_2P$-type (space group
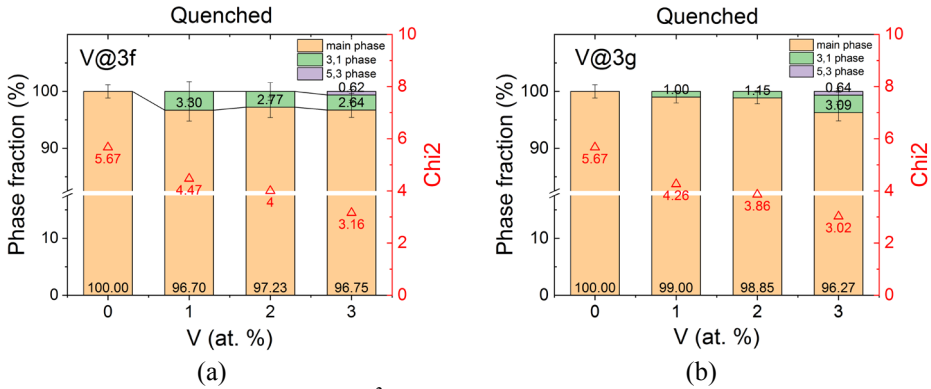
**Figure 5.3:** Phase fraction and $\chi^2$ for Mn$_{0.7}$Fe$_{1.21-y}$V$_y$P$_{0.6}$Si$_{0.4}$ samples obtained for refinements of the X-ray diffraction data assuming that vanadium preferentially occupies the 3f (a) or the 3g (b) position.

*P-62m*) main phase. The main impurity phase is (Mn,Fe)$_3$(P,Si)$_1$. The amount of impurity increases with an increasing vanadium substitution. There are two possible sites for vanadium substitution, the 3*f* and the 3*g* site. These two different models were compared in the refinement of the diffraction patterns. The refinement results show that there is no obvious difference in the quality of fit (expressed by $\chi^2$) between these two different models with a different preferred site occupancy for vanadium. As the *Z* value of V, Mn and Fe are quite similar it is difficult to distinguish their positions (in terms of the site occupancy of these three atoms at the 3*f* and 3*g* sites) by X-ray diffraction. Further study, preferably with neutron diffraction, is needed to investigate the site occupancy of vanadium.

Figure 5.4 shows the evolution of the lattice parameters *a* and *c*, the *c*/*a* ratio and the unit-cell volume *V* in the paramagnetic state (at 500 K) for the vanadium substituted Mn$_{0.7}$Fe$_{1.21-y}$V$_y$P$_{0.6}$Si$_{0.4}$ compounds. The addition of vanadium as a substitutional element leads to the following main features. The increasing V content (*y*) results in a decrease in lattice parameter *a* and an increase in lattice parameter *c*, while the *c*/*a* ratio increases accordingly. However, the volume of the unit cell expansion is negligible (0.1%) when 3% vanadium is added. Together with the phase fraction ratio shows in Figure 5.3 that we have an impression that the vanadium substitution mainly has an effect of forming the impurity phase.
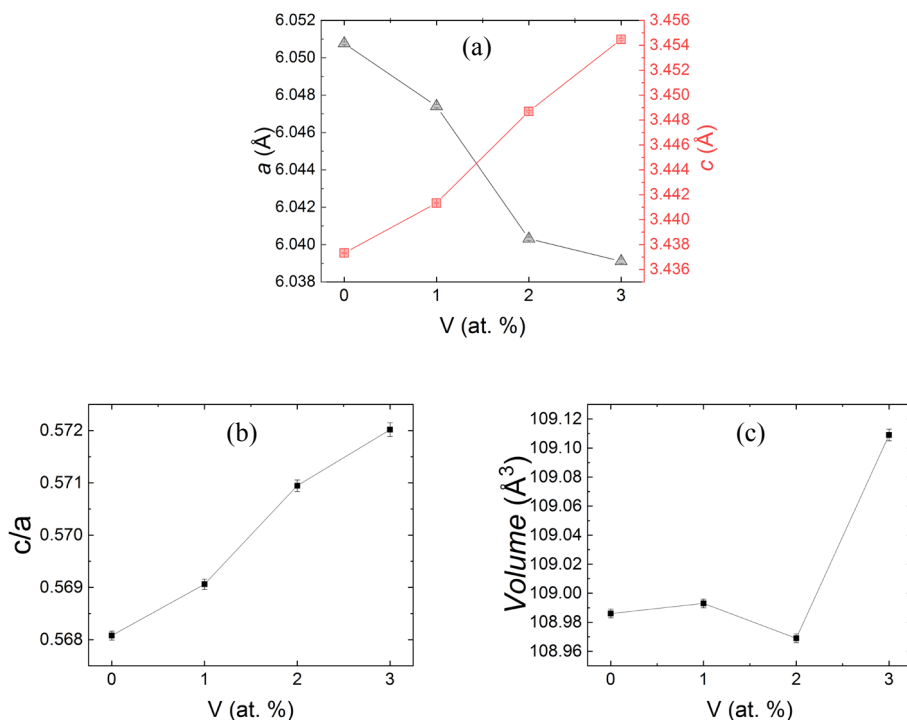
***Figure 5.4:*** Lattice parameter *a* and *c* (a), *c/a* ratio (b) and unit-cell volume (c) as a function of the vanadium content for the $Mn_{0.7}Fe_{1.21-y}V_yP_{0.6}Si_{0.4}$ (*y* = 0.00, 0.01, 0.02, 0.03) compounds.

### 5.3.2.2 Magnetic properties

In Figure 5.5 the temperature dependent magnetisation in an applied magnetic field of 1 T, the field-dependent magnetisation measured at a temperature of 5 K and the DSC curves in zero field are shown for the $Mn_{0.7}Fe_{1.21-y}V_yP_{0.6}Si_{0.4}$ compounds. From the DSC data, summarised in Table 5.1, it is clear that the vanadium substitution results in a reduction of the latent heat, which reflects the strength of the first-order magnetic phase transition (FOMT) [5]. In other words, the V substitution is found to weaken the first-order transition. At the same time, thermal hysteresis increases. The values of $T_C$ and the thermal hysteresis $\Delta T_{hys}$ are listed in Table1. This increase in $\Delta T_{hys}$ may be due to the increase in the impurity phase fraction.
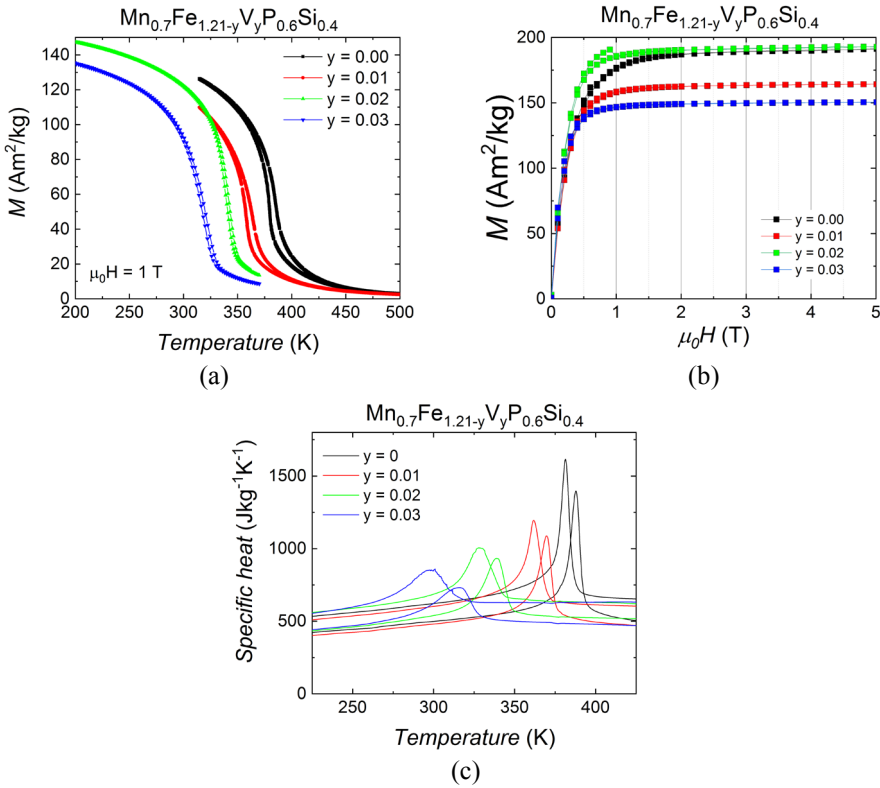
(a)



(b)



(c)

**Figure 5.5:** Temperature-dependent magnetisation in an applied magnetic field $\mu_0 H$ of 1 T (a), field-dependent magnetisation measured at a temperature of 5 K (b) and the specific heat derived from DSC measurements in zero fields upon cooling and heating for Mn$_{0.7}$Fe$_{1.21-y}$V$_y$P$_{0.6}$Si$_{0.4}$ ($y$ = 0.00, 0.01, 0.02, 0.03) compounds.

The saturation magnetisation is measured at 5 K for magnetic fields up to 5 T (Figure 5.5(b)). The field-dependent magnetisation curves show that the phase transition can be driven by a small external field when a small amount of vanadium is incorporated in the structure of the Fe$_2$P alloy. The magnetisation reaches 79%, 88%, 89% and 93% of its saturation magnetisation for V substitutions of y = 0.00, 0.01, 0.02 and 0.03 respectively, in an external field of 0.5 T. This result is in good agreement with previous results[2], where V substituted Mn in the Mn-rich samples.

**Table 5.1:** Curie temperature $T_C$, thermal hysteresis $\Delta T_{hys}$ and latent heat in zero field for the $Mn_{0.7}Fe_{1.21-y}V_yP_{0.6}Si_{0.4}$ compounds. The Curie temperature was derived on heating, the thermal hysteresis derived upon cooling and heating, and the latent heat integrates the heating peak in DSC measurement in zero field.

| $Mn_{0.7}Fe_{1.21-y}V_yP_{0.6}Si_{0.4}$ | $T_C$ (K) | $\Delta T_{hys}$ (K) | *Latent heat* (Jg$^{-1}$) |
|---|---|---|---|
| $y = 0.00$ | 382 | 7.1 | 7.1 |
| $y = 0.01$ | 370 | 8.5 | 5.6 |
| $y = 0.02$ | 339 | 11.5 | 5.2 |
| $y = 0.03$ | 316 | 15.9 | 4.8 |

### 5.3.3 Effect of heat treatment

The influence of the heat treatment on the magnetisation for the $Mn_{0.7}Fe_{1.21-y}V_yP_{0.6}Si_{0.4}$ ($y$ = 0.00 and 0.01) compounds was studied for both compositions sintered at 1373 K for 25 h. Two heat treatments were compared, where one sample was quenched in cold water, and the other one is naturally cooled to room temperature in the oven.

The temperature dependence of the magnetisation curves indicates that the quenched samples have a higher $T_C$ and a higher saturation magnetisation than the oven cooled samples (Figure 5.6(a)). From the phase fraction defined by X-ray diffraction, It is quite obvious that the difference in $T_C$ and saturation magnetisation is due to the amount of impurity phase. The more impurity phase is present a larger
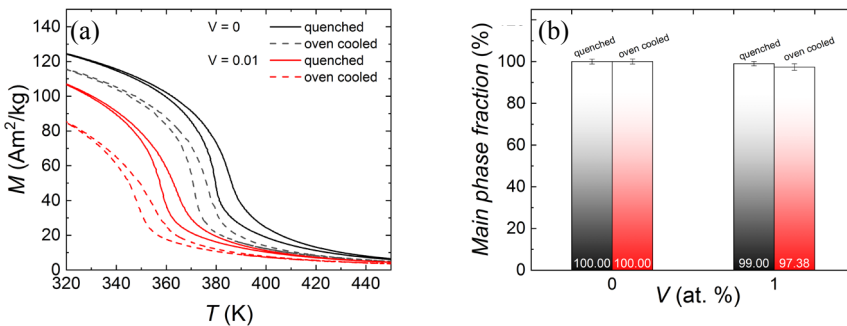


**Fig**ure 5.6: Temperature dependence of the magnetisation during heating and cooling at a rate of 2 K/min in an external magnetic field 1 T for the $Mn_{0.7}Fe_{1.21-y}V_yP_{0.6}Si_{0.4}$ ($y$ = 0.00 and 0.01) compounds under quenched (solid line) and oven cooled (dash line) conditions (a) with the main phase fraction (b).

decrease in $T_C$ and in the saturation magnetisation is found (Figure 5.6).

## 5.4 Conclusions

The effect of V substitution for Fe is investigating in the $Mn_{0.7}Fe_{x-y}V_yP_{0.6}Si_{0.4}$ alloys. The $(Mn,Fe)_{1.91}(P,Si)$ compound was chosen as a starting point to obtain the smallest impurity content. For an increasing V content the *a*-axis expands and the *c*-axis shrinks (together with the *c/a* ratio), whereas the unit-cell volume stays about the same. The ferromagnetic transition temperature $T_C$ decreases with increasing V content. In the $Mn_{0.7}Fe_{1.18}V_{0.03}P_{0.6}Si_{0.4}$ compounds, 93% of its saturation magnetisation at 5 K was reached in an applied magnetic field of 0.5 T, which makes this compound a promising candidate for low-field applications. The oven-cooled samples contain a larger impurity phase fraction than the quenched samples, which results in a lower transition temperature.

**5**

## References

1. Lai, J., et al., *Combined effect of annealing temperature and vanadium substitution for mangetocaloric $Mn_{1.2-x}V_xFe_{0.75}P_{0.5}Si_{0.5}$ alloys*. Journal of Alloys and Compounds, 2019. **803**: p. 671-677.
2. Lai, J., et al., *Tuning the magneto-elastic transition of $(Mn,Fe,V)_2(P,Si)$ alloys to low magnetic field applications*. Journal of Alloys and Compounds, 2020. **821**: p. 153451.
3. Nguyen H. Dung, et al., *Mixed Magnetism for Refrigeration and Energy Conversion*. Advanced Energy Materials, 2011. **1**: p. 5.
4. Rodriguez-Carvajal, J., *Abstract Satelite Meeting on Powder Diffraction*. Congr. Int. Union of Crystallography. Toulouse: France, 1990.
5. Thanh, D.T.C., et al., *Structure, magnetism, and magnetocaloric properties of $MnFeP_{1-x}Si_x$ compounds*. Journal of Applied Physics, 2008. **103**.

# SYNCHROTRON x-RAY DIFFRACTION ON THE CHARGE DISTRIBUTION IN La(Fe,Co,Si)$_{13}$ COMPOUNDS

**6**
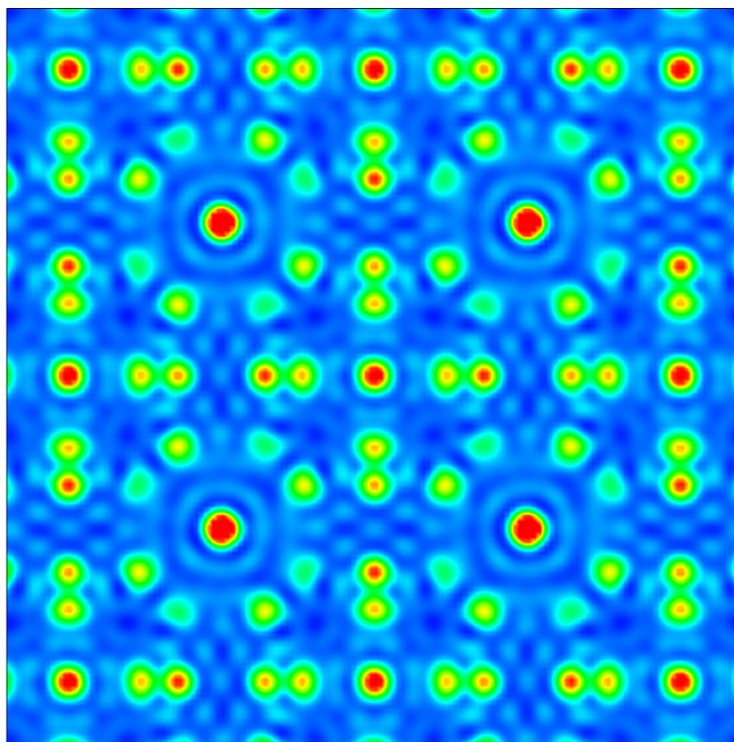
## 6.1 Introduction

The La(Fe, Si)13 class of materials exhibit a giant magnetocaloric effect (GMCE) and is attractive as a highly efficient and environmentally-friendly refrigerant material for room-temperature magnetic refrigeration [1]. When heating these materials above the ferromagnetic transition temperature, the cubic structure undergoes a volume change. The origin of the volume change is attributed to a change in the size of the magnetic moments across the transition.[2] The same mechanism was found in the hexagonal Fe2P-based materials [3] in the presence of two magnetic sublattices giving rise to mixed magnetism and a subtle charge redistribution across the magnetic transition. Investigating the nature of the transition in the La(Fe,Si)13 system and the search for a charge redistribution across the transition in this system will complement our insight in the physics of both material families and help in the development of these materials.

## 6.2 Experimental

The three studied samples, $LaFe_{11.8-x}Co_xSi_{1.2}$ ($x$ = 0.25, 0.69 and 1.13) compounds, were prepared by Vacuumschmelze.

**6**

The magnetic properties were measured in a SQUID (Superconducting Quantum Interference Device) magnetometer using the RSO mode. The entropy changes were determined by field-dependent isothermal magnetisation measurements.

High-resolution X-ray diffraction (XRD) was performed at the BM01A beamline at the European Synchrotron Radiation Facility (ESRF) using a wavelength of 0.69264 Å and an energy of 17 keV. The covered temperature range is from 150 to 500 K in steps of 2 K. The temperature was controlled by a Nitrogen Cryosteam. The powder samples were placed in capillaries with a 0.5 mm diameter and spun during exposure. The powder X-ray diffraction data were analysed by Rietveld refinement using the FULLPROF package [4]. The electron densities were calculated from the fitted structure factors using VESTA [5].
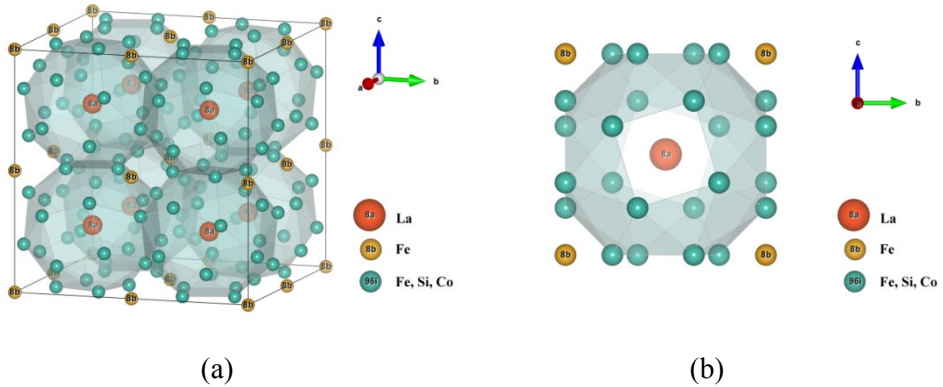
(a)                                        (b)

**Figure 6.1:** Schematic diagram of the atomic structure for La(Fe,Co,Si)$_{13}$ with (a) the unit cell and (b) a front view of the primitive cell.

## 6.3 Results and discussion

### 6.3.1 Crystal structure of La(Fe, Si, Co)$_{13}$

The structure of the NaZn$_{13}$-type La(Fe, Si)$_{13}$ compounds (space group $Fm\bar{3}c$) is shown in Figure 6.1. The *8a* site at position (1/4,1/4,1/4) is occupied by La, the *8b* site at position (0,0,0) is occupied by Fe, and the *96i* site at position (0,$y$,$z$) is occupied by the Fe and Si. The unit cell contains 8 formula units ($Z = 8$) and is composed of 8 cubic primitive cells with a rotating cage around the central La atom [6]. According to Liu et al. [7], the Co atom has a preference for the *96i* site.

The intensity distribution for 2θ scattering angles from 19.5° to 21° as a function of temperature is shown in Figure 6.2. The most significant peak at 20.5° corresponds to the (531) diffraction peak, which is the strongest reflection of the La(Fe,Si,Co)$_{13}$ main phase. The weaker peak at 20.8 corresponds to the (600) and (442) diffraction peak, which are overlapping. The change in peak position across the transition directly reflects the change in lattice parameter for this cubic structure. The temperature where that change in lattice parameter takes place corresponds to the ferromagnetic-to-paramagnetic transition temperature $T_C$. The step in diffraction angle of the (531) peak before and after the transition is most pronounced for $y = 0.25$, becomes smaller with increasing Co content, and is the least pronounced for $y = 1.13$. From these data for the main phase, it is found that Co substitution in La(Fe,Si)$_{13}$ results in an increase in $T_C$ and a tuning of the material from a first-order magnetic phase transition (FOMT) towards a second-
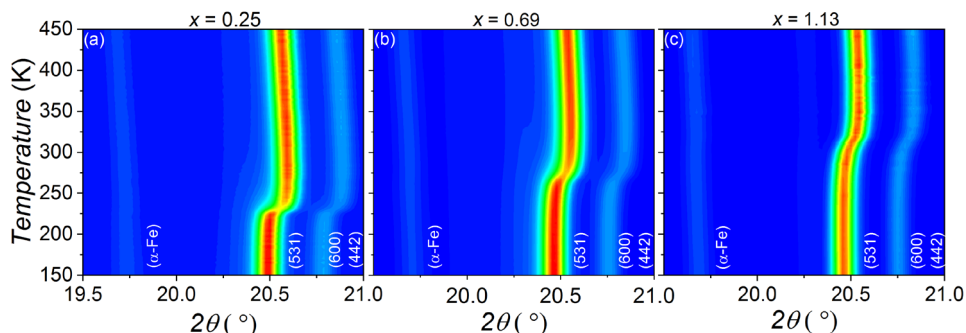
**Figure 6.2:** Intensity versus scattering angle $2\theta$ (°) as a function of temperature $T$ (K) for LaFe$_{11.8-x}$Co$_x$Si$_{1.2}$ ($x$ = 0.25, 0.69 and 1.13) compounds obtained in high-resolution X-ray powder diffraction measurements.

order phase transition (SOMT). This is in line with previous research [8]. There is also a weak peak around 19.7° belonging to the α-Fe impurity phase, which evolves continuously without any abrupt jump. This means this impurity phase doesn't show a phase transition in this temperature window. Only the lattice undergoes thermal expansion.

The XRD investigation confirms that the structure of the LaFe$_{11.8-x}$Co$_x$Si$_{1.2}$ compounds belongs to the NaZn$_{13}$-type space group. There are two impurity phases present, in the form of α-Fe (space group *Im-3m*) and La$_2$O$_3$ (space group *P-3m1*) [9, 10].
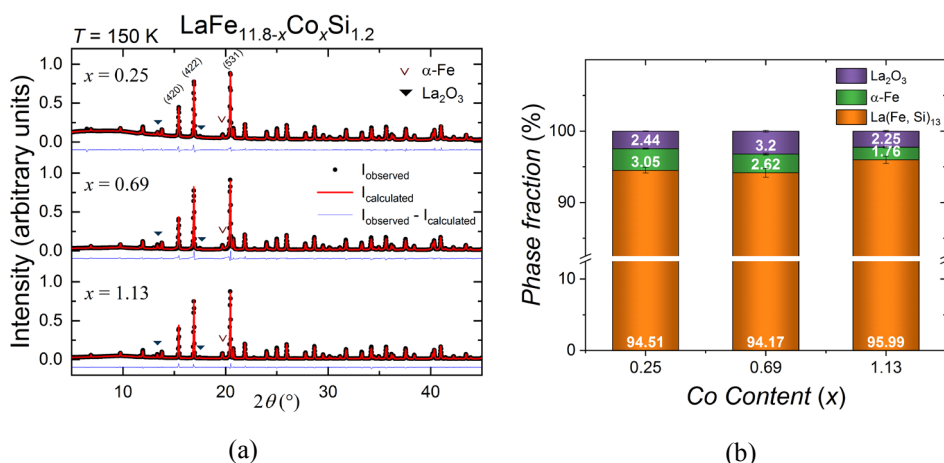


(a)                                    (b)

**Figure 6.3** Partial X-ray patterns and Rieveld refinements in 150 K (a) and phase fraction of LaFe$_{11.8-x}$Co$_x$Si$_{1.2}$ ($x$ = 0.25, 0.69 and 1.13) compounds.
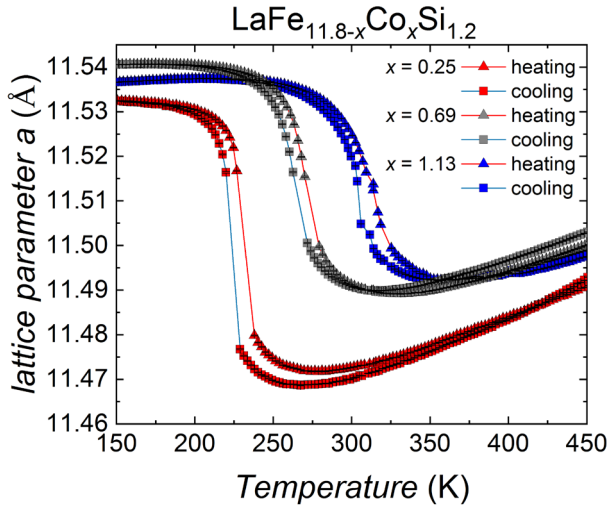
**Figure 6.4:** Temperature dependence lattice parameter $a$ for LaFe$_{11.8-x}$Co$_x$Si$_{1.2}$ ($x = 0.25$, 0.69 and 1.13) compounds. Triangles with a red line refer to the heating and the squares with a blue line refers to the cooling process.

The phase fraction of LaFe$_{11.8-x}$Co$_x$Si$_{1.2}$ ($x = 0.25$, 0.69 and 1.13) compounds is shown in Figure 6.3(b). All three samples have three phases, and the main phase is around 95% pure, indicating that the samples are optimised so that the increasing Co content has a limited effect on the impurity phases.

The lattice parameter changes can be considered as evidence for the order of the magnetic transition. As shown in Figure 6.4(a), the FOMT sample (red symbols) with lowest Co content has the largest lattice parameter change across the transition, while the SOMT sample (blue symbols) with the highest Co content has the smallest lattice parameter change in the temperature window.

### 6.3.2 Magnetic properties

The temperature-dependent magnetization of LaFe$_{11.8-x}$Co$_x$Si$_{1.2}$ ($x = 0.25$, 0.69 and 1.13) compounds were measured in an applied magnetic field of 1 T. The transition temperature of LaFe$_{11.8-x}$Co$_x$Si$_{1.2}$ ($x = 0.25$, 0.69 and 1.13) compounds are 225, 265 and 320 K, respectively. The thermal hysteresis is negligible in this series of samples.
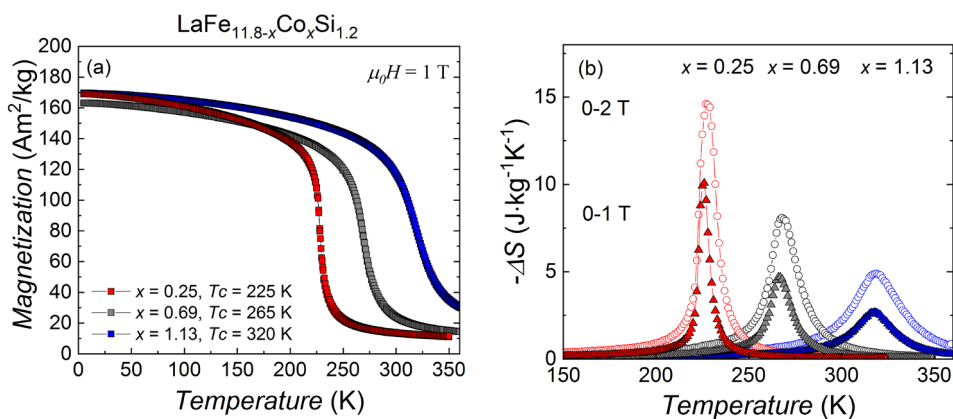
**Figure 6.5:** Temperature dependent magnetization (a) for $LaFe_{11.8-x}Co_xSi_{1.2}$ ($x = 0.25$, 0.69 and 1.13) compounds measured in a magnetic field of $\mu_0H = 1$ T and magnetic entropy change (b) for 1 T (filled symbols) and 2 T (open symbols).

The magnetic entropy change $-\Delta S$ was determined in magnetic fields up to 2 T (Figure 6.5(b)). In a magnetic field of 1 T, the $LaFe_{10.35}Co_{0.25}Si_{1.2}$ sample has a maximum entropy change of $-\Delta S_{1T} = 10.1$ $Jkg^{-1}K^{-1}$. The entropy change decreases as a function of the Co content with an increase in peak width, which also indicates a transition from a FOMT towards a SOMT.

### 6.3.3 Internal coordinates of Fe atom

In Figure 6.6, a shift in the internal coordinates of the *96i* Wyckoff position $(0, y, z)$ within the unit cell across $T_C$ is observed. The *96i* site is preferentially occupied by Fe, Si and Co. For Co content $b = 0.25$ a significant discontinuous shift is observed in both $y$ and $z$ upon heating. With increasing Co content, the jumps become smaller. Around $T_C$ there is a bump for each sample, as the uncertainties in the Rietveld refinement increase in the coexistence region of the ferromagnetic (FM) and paramagnetic (PM) phase which leads to a substantial peak overlap and a reduced phase fraction. The bump around 420 K for the $LaFe_{9.47}Co_{1.13}Si_{1.2}$ sample is due to the decrease in intensity of the X-ray pattern, related to reduced beam intensity.
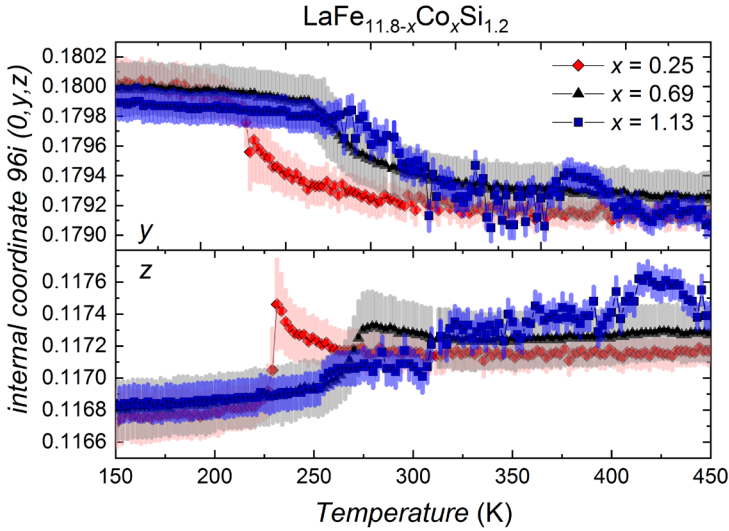
***Figure 6.6:*** Temperature dependence of the internal coordinates of the *96i* atoms $(0, y, z)$ for $LaFe_{11.8-x}Co_xSi_{1.2}$ ($x = 0.25$, $0.69$ and $1.13$) compounds across $T_C$ upon heating.

The bond length can be calculated based on the relative atom coordinate of the site and the lattice parameter *a*. In $LaFe_{11.8-x}Co_xSi_{1.2}$ ($x = 0.25$, $0.69$ and $1.13$) compounds the relative bond length of the *8a-8a*, *8b-8b* and *8a-8b* bonds $d_{aa}/a$, $d_{ab}/a$ and $d_{bb}/a$ are fixed ($1/2$, $1/2\sqrt{3}$ and $1/2$ respectively) due to their fixed internal coordinate position. However, some of the relative bond lengths change as a result of the temperature variation in the internal coordinates *y* and *z* of the *96i* site. According to the Wyckoff position of the unit cell and the atoms internal coordinates, the relative bond length with at least one atom on a *96i* site can be described as follows:

$$8a - 96i: \frac{d_{ai}}{a} = \sqrt{(\frac{1}{4} - y)^2 + (\frac{1}{4} - z)^2 + (\frac{1}{4})^2}$$

$$8b - 96i: \frac{d_{bi}}{a} = \sqrt{y^2 + z^2}$$

$$96i - 96i: \frac{d_{ii1}}{a} = \sqrt{(z - y)^2 + \left(\frac{1}{2} - y - z\right)^2} \; ; \frac{d_{ii2}}{a} = 2y; \frac{d_{ii3}}{a} = 2z$$
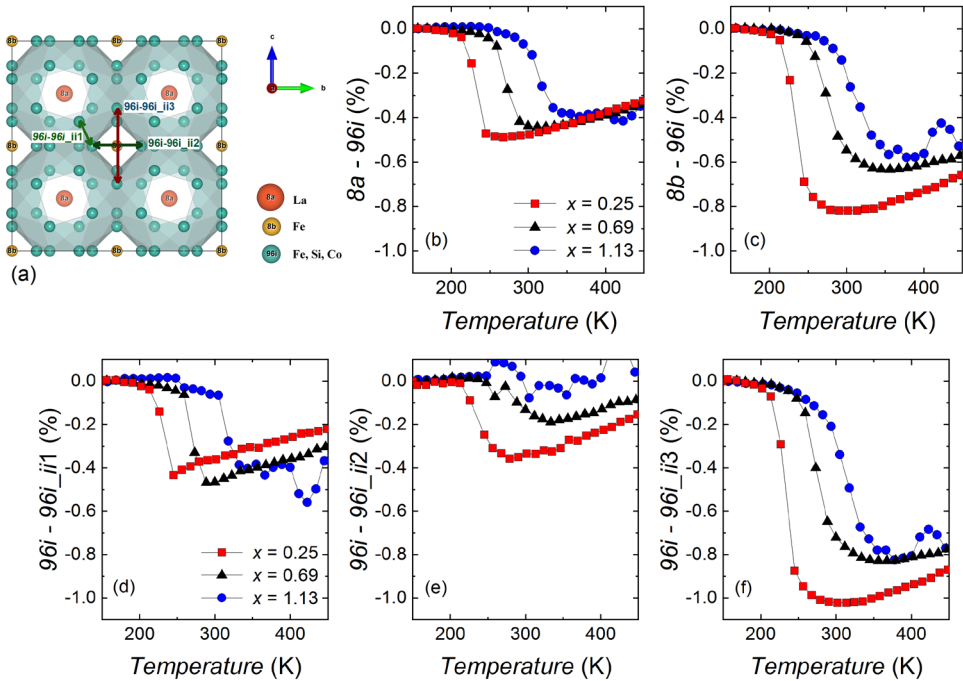
**6**

***Figure 6.7:*** (a) Schematic diagram of the atomic structure for La(Fe,Co,Si)$_{13}$. (b-f) Change in bond length for the different bonds as a function of temperature (see text).

The estimated bond lengths are shown in Fig 6.7 (b-f). Figure 6.7 (a) shows a schematic diagram of the atomic structure for La(Fe, Co, Si)$_{13,}$ where the relative bond lengths of d$_{ii1}$ /a, d$_{ii2}$ /a and d$_{ii3}$ /a are indicated. All bond lengths are

normalised and compared with the data at 150 K. From Figure 6.7 we can conclude that the most pronounced change in bond length is found for the *8b-96i* bond ($d_{bi}$) and for the third *96i-96i* bond ($d_{ii3}$).

The angular rotation of the cage formed by the *96i* atoms with respect to the cubic unit cell can be calculated by:

$$\varphi = tan^{-1}\left(\frac{z}{y}\right)$$

The angle is 32.98$^{o}$, 32.95$^{o}$ and 32.96$^{o}$ for the LaFe$_{11.8-x}$Co$_x$Si$_{1.2}$ ($x$ = 0.25, 0.69 and 1.13) samples at 150 K, respectively. There is an around 0.15$^{o}$ angular change for all three samples. Unlikely the lattice parameter change, There is no obvious
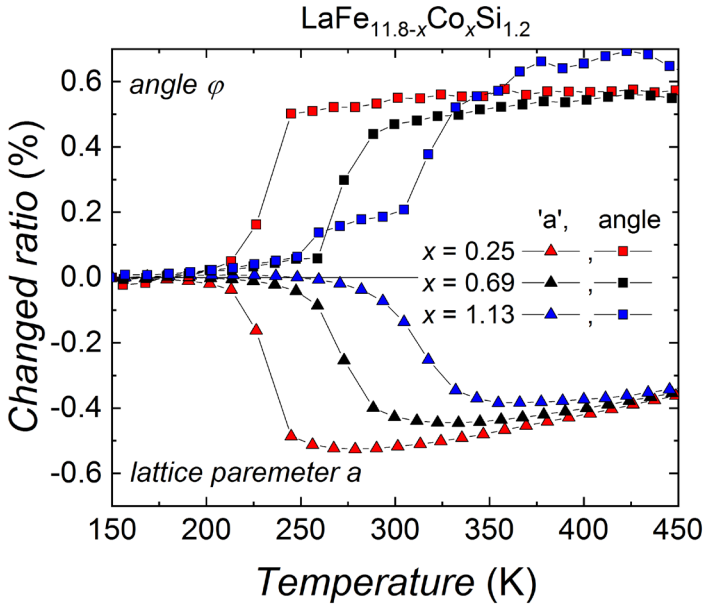
**Figure 6.8:** Comparison the relative change in the cage rotation angle $\varphi$ and the lattice parameter $a$ for the LaFe$_{11.8-x}$Co$_x$Si$_{1.2}$ ($x$ = 0.25, 0.69 and 1.13) compounds.

**6**

difference for FOMT and SOMT sample for the change of the cage rotation. All three samples have a step in cage rotation angle change around $Tc$.

The change in cage orientation angle-angle $\varphi$ as a function of temperature is compared with the change in lattice parameter $a$ in Figure 6.8. The La(Fe, Si)$_{13}$ compounds are famous for their negative thermal expansion, which is clearly observed in the temperature evolution of the lattice parameter. The rotation angle of the cage is found to show a mirror image of the change in lattice parameter with roughly the same relative change of about 0.5% for all three samples.

### 6.3.4 Electronic structure

The high-resolution X-ray diffraction data can be used to extract the electron densities from the structure factors obtained from the refinement. The difference in electron density across the transition is obtained by subtracting the paramagnetic from the ferromagnetic state to emphasise the change. In Figure 6.9, the PM and FM states correspond to positive (red) and negative (blue) values, respectively. The same method has been successfully applied in our previous investigation [3, 11, 12]. From the bond lengths, we can conclude that the most pronounced change in bond

length is for the *8b-96i* bond ($d_{bi}$) and the third *96i-96i* bond ($d_{ii3}$). For the electron density study, the most interesting parts are in the vicinity of these bonds.

The 112 atoms in the unit cell ($Z = 8$) of Figure 6.1 are equivalently represented by the 14 atoms in the primitive cell of Figure 6.1 (b). The projection of the primitive cell is shown in Figure 6.9 (a-c) for $LaFe_{11.8-x}Co_xSi_{1.2}$ ($x = 0.25$, 0.69 and 1.13) compounds, respectively. From the projection, we can see that the biggest changes in the electron density of the primitive cell are found for the FOMT ($b = 0.25$) sample and the weak FOMT ($b = 0.69$) sample, while the electron density difference in the SOMT ($b = 1.13$) sample is reduced to about half of the value observed for the other two samples.

The integration from $z = -0.05 - 0.05$ (layer I) and $z = 0.45 - 0.55$ (layer II) in the primitive cell is shown in Figure 6.9 (d-f) and (g-i). The four dipoles in every graph represent the four *96i* atoms in the cell. The blue contribution represents a negative value, which means FM state and the red represent the PM state. With the angle variance and dipoles, we can observe the rotation of the cage represented by the square with four *96i* atoms. The arrows in Figure 6.9 (d and g) indicate how atoms move.
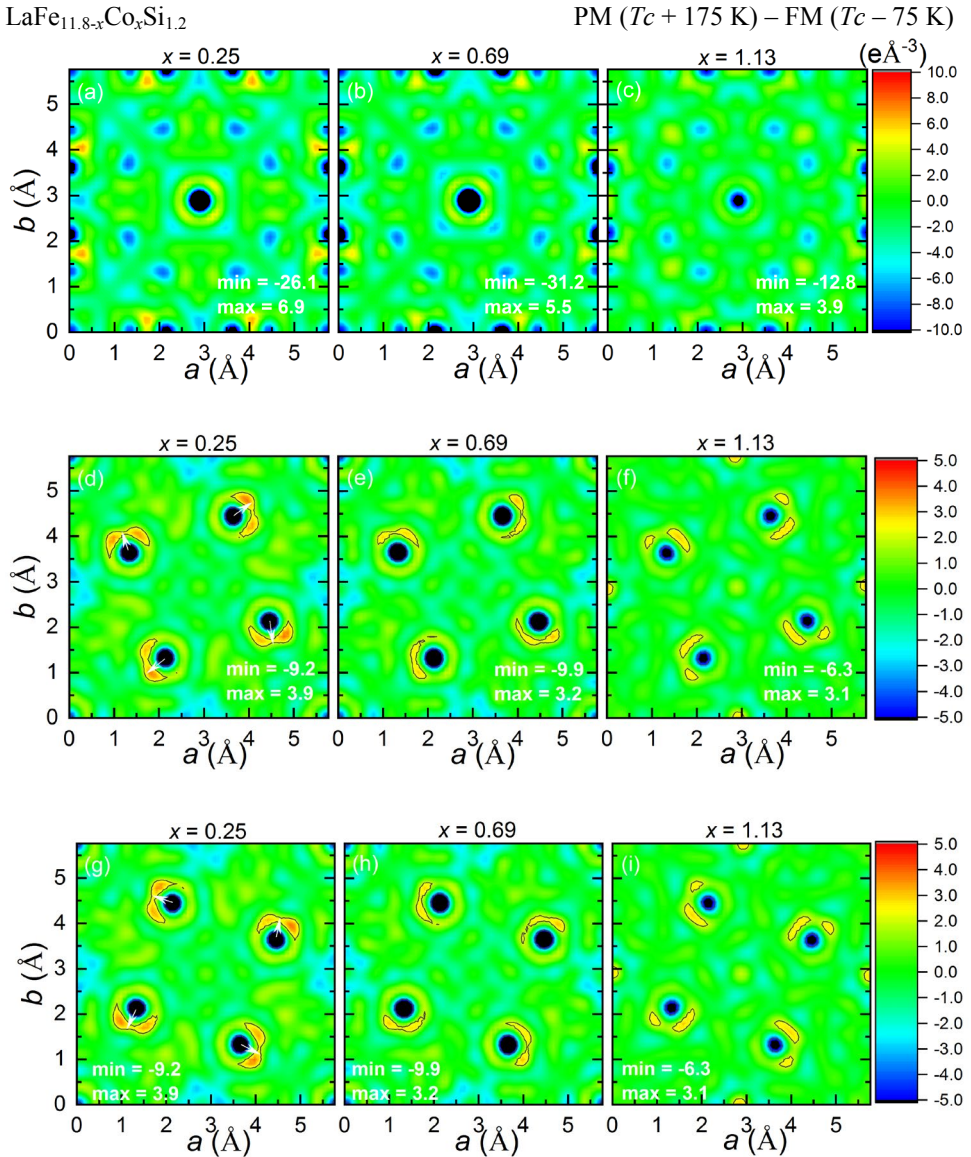
**6**

**Figure 6.9:** Electron density difference plots between paramagnetic ($T_C + 175$ K) and ferromagnetic ($T_C - 75$ K) phase in the local environment of the *8a* site for LaFe$_{11.8-x}$Co$_x$Si$_{1.2}$ ($x = 0.25$, $0.69$ and $1.13$) compounds. The electron densities were integrated from $z = 0 - 0.5$ (a, b, c), from $z = -0.05 - 0.05$ (d, e, f) and from $z = 0.45 - 0.55$ (g, h, i). The color-coded scale is given in e/Å$^3$. To emphasize the graph, the contour line is drawn in the position of -4 and +2 e/Å$^3$
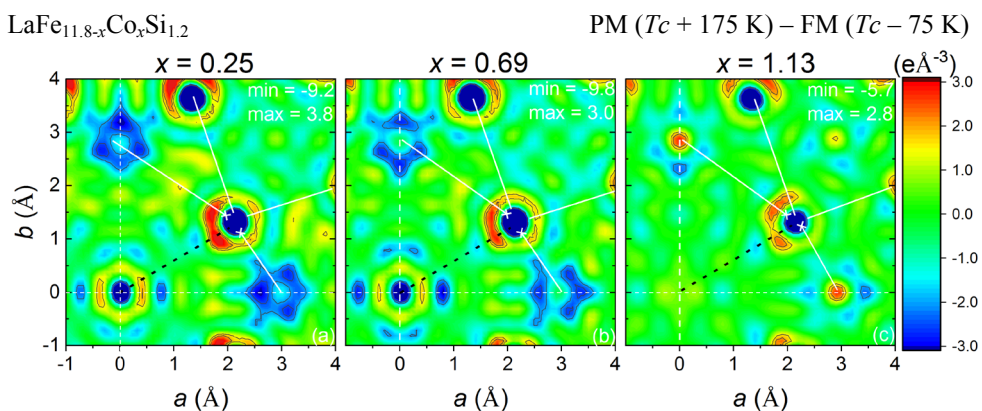
**Figure 6.10:** Electron density difference plots between paramagnetic ($T_C$ + 175 K) and ferromagnetic ($T_C$ − 75 K) phase in the local environment of the *96i* site for LaFe$_{11.8-x}$Co$_x$Si$_{1.2}$ ($x$ = 0.25, 0.69 and 1.13) compounds. The electron densities were integrated from $z$ = -0.05 – 0.05. The colour-coded scale is given in e/Å$^3$. To emphasise the graph, the contour line is drawn in the position of -2.5, -2, +1.5, +2 e/Å$^3$. White solid line indicates the centre 96i atom to the nearest *96i* atom. The line with a cross at the end indicate two atoms are not in the same plane. Black dot line indicates centre *96i* to *8b* atom.

Figure 6.10 shows the projections of the electron density map to select one of the *96i* atom in the cage as a centre and compensate for the shift of the atom. The internal coordinate of *8b* site is (0, 0, 0) which can be found in the corresponding coordinates in Figure 6.10 (crossing of the white dash line).

The substituion of Co and the associated reduction of the number of electrons on the *8b* site seem to strongly suppress the electronic changes across the transitions. The same phenomenon can also be found in the *96i* site but less pronounced than the *8b* site.

In the unit cell, the most significant change in bond lengths occurs between the *8b* and *96i* sites. The electron density map was drawn using the *8b* site as a centre to study the charge redistribution around this atom. The selected area is shown in Figure 6.11 (1-3). The unit was cut into a slice to study the single layer atom behaviour. Slice $z$ = 0.05 - 0.1 and slice $z$ = 0.20 – 0.25 is not included as it contains no relevant atoms on the layer.

It is clear that the electron density change is more pronounced in the FOMT sample than in the SOMT sample.
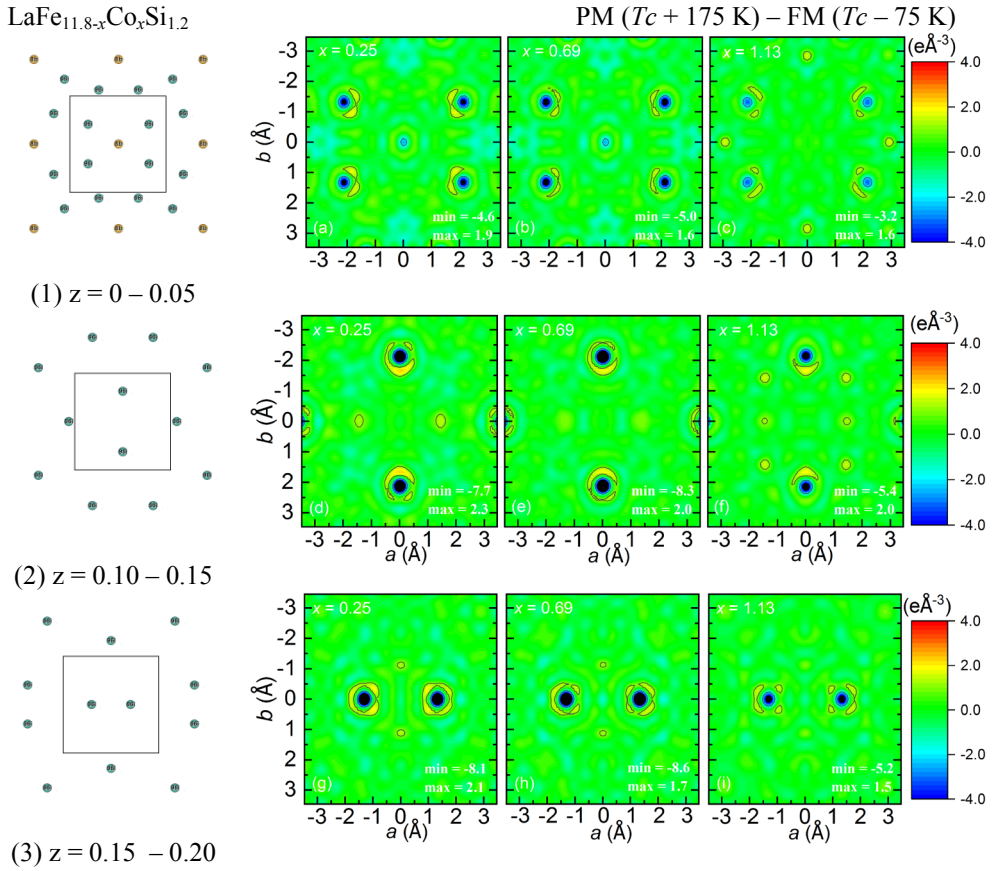
**Figure 6.11:** Electron density difference plots between paramagnetic ($T_C$ + 175 K) and ferromagnetic ($T_C$ − 75 K) phase in the local environment of the *8b* site for LaFe$_{11.8-x}$Co$_x$Si$_{1.2}$ ($x$ = 0.25, 0.69 and 1.13) compounds. The electron densities were integrated from $z$ = 0 − 0.05 (a, b, c), from $z$ = 0.1 − 0.15 (d, e, f) and from $z$ = 0.15 − 0.2 (g, h, i). The color-coded scale is given in e/Å$^3$. To emphasize the graph, the contour line is drawn in the position of -2 and +1 e/Å$^3$. Schematic diagram of the atomic structure in the layer for La(Fe,Co,Si)$_{13}$ is shown in the column on the left (1-3).

## 6.4 Conclusions

The structural, magnetic and electronic properties of LaFe$_{11.8-x}$Co$_x$Si$_{1.2}$ ($x$ = 0.25, 0.69 and 1.13) compounds are studied. With increasing Co content, the material is tuned from a FOMT towards a SOMT, $T_C$ increases and the thermal hysteresis remains negligible. In the unit cell, the most remarkable change in bond length is between the *8b* and *96i* sites and for one of the bonds between two neighbouring *96i* sites. The negative thermal expansion correlates with the angle change in the

orientation of the cage formed by the 96i atoms within the cubic unit cell across the transition. In the electron density map, we revealed how the *96i* cage rotates within the cubic primitive cell. The samples with a smaller Co content show a larger variation in the electron density compared to the Co-rich sample.

## References

1. Fujita, A., et al., *Large magnetovolume effects and band structure of itinerant-electron metamagneticLa(Fe$_x$Si$_{1-x}$)$_{13}$compounds*. Physical Review B, 2003. **68**(10).

2. Gruner, M.E., et al., *Element-resolved thermodynamics of magnetocaloric LaFe$_{(13-x)}$Si$_{(x)}$*. Phys Rev Lett, 2015. **114**(5): p. 057202.

3. Boeije, M.F.J., et al., *Efficient Room-Temperature Cooling with Magnets*. Chemistry of Materials, 2016. **28**(14): p. 4901-4905.

4. Rodriguez-Carvajal, J., *Abstract Satelite Meeting on Powder Diffraction*. Congr. Int. Union of Crystallography. Toulouse: France, 1990.

5. Momma, K. and F. Izumi, *VESTA 3 for three-dimensional visualisation of crystal, volumetric and morphology data*. Journal of applied crystallography, 2011. **44**(6): p. 1272-1276.

6. Palstra, T.T., et al., *Mictomagnetic, ferromagnetic, and antiferromagnetic transitions in La(Fe$_x$Al$_{1-x}$)$_{13}$ intermetallic compounds*. Phys Rev B Condens Matter, 1985. **31**(7): p. 4622-4632.

7. Liu, X.B. and Z. Altounian, *Effect of Co content on magnetic entropy change and structure of La(Fe$_{1-x}$Co$_x$)$_{11.4}$Si$_{1.6}$*. Journal of Magnetism and Magnetic Materials, 2003. **264**(2-3): p. 209-213.

8. Huang, R., et al., *Giant negative thermal expansion in NaZn$_{13}$-type La(Fe,Si,Co)$_{13}$ compounds*. J Am Chem Soc, 2013. **135**(31): p. 11469-72.

9. Liu, J., et al., *Exploring La(Fe,Si)$_{13}$-based magnetic refrigerants towards application*. Scripta Materialia, 2012. **67**(6): p. 584-589.

10. Liu, J., et al., *Systematic study of the microstructure, entropy change and adiabatic temperature change in optimised La–Fe–Si alloys*. Acta Materialia, 2011. **59**(9): p. 3602-3611.

11. Boeije, M.F.J., et al., *Mixed magnetism in magnetocaloric materials with first-order and second-order magnetoelastic transitions*. Journal of Physics D: Applied Physics, 2017. **50**(17): p. 174002.

12. Maschek, M., et al., *Charge redistribution and the magnetoelastic transition across the first-order magnetic transition in (Mn,Fe)$_2$(P,Si,B).* Physical Review B, 2018. **98**(22).

**6**

# BALL MILLING SYNTHESIS OF MAGNETOCALORIC Ni–Mn–Sn HEUSLER COMPOUNDS

**7**



| ● | ○ | □ | ⬤ |
|---|---|---|---|
| Ni | Ni | Mn | Sn |
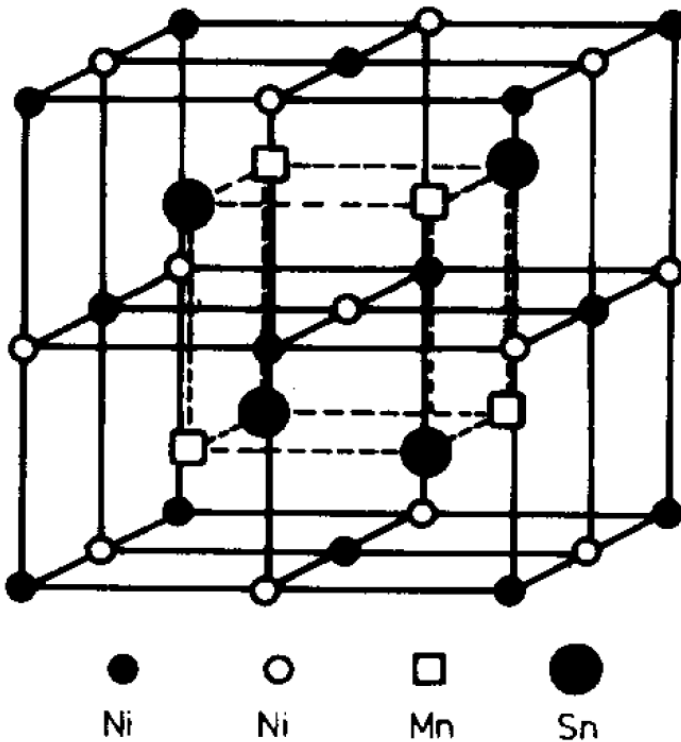
## 7.1 Introduction

Heusler alloys are a vast collection of more than 1000 compounds with the composition $Cu_2MnAl$ that behave like a ferromagnet, although none of its constituent elements is magnetic by itself.[1, 2] These materials display different functional properties such as shape memory, super elastic, barocaloric and magnetocaloric effects.

A thermomagnetic motor (TMM) prototype, built by Swiss Blue Energy, shows the possibility of converting low-temperature waste heat into electrical or mechanical energy.[3] In order to get a high efficiency, appropriate magnetocaloric materials should be used. In contrast to magnetic refrigeration, a higher Curie temperature needs to be selected for the magnetocaloric materials (MCM).

In the last decades, a lot of studies focused on Ni-Mn based materials as promising candidates for magnetic energy conversion applications, as they are made of non-toxic and earth-abundant materials with a tunable transition temperature, have a sizeable magnetocaloric effect and demonstrate a good mechanical behaviour[4-7]. These materials are also sensitive to the applied magnetic field and can be used in applications with small driving fields.

The widely used fabrication methods for Ni-Mn based Heusler alloys are arc melting, induction melting and melt spinning follow with a long-time heat treatment to achieve product homogeneity. In this work, different fabrication methods and heat treatments are compared. Based on the optimised synthesis method, the Mn:Sn ration was adjusted to maximise the magnetisation change for the TMM application. Substituting elements like Co[8] and Al[9] have an effect of increasing the total magnetisation.

## 7.2 Experimental

Samples of Ni-Mn based materials have been prepared by different fabrication methods: melt-spinning (MS), arc melting (AM) and ball milling (BM) followed by heat treatment with different annealing (ANN) temperatures and times.

As-cast tablets were prepared by ball milling using starting materials of Ni(99.8%), Mn (99.7%), Co( 99.8%) and Al (99.97%) powder and Sn shots (8 – 20 mesh, 99.8%). After 10 hours of ball milling with a rotation speed at 190 rounds per minute (rpm), the samples were pressed into tablets followed by different fabrication methods. The arc-melting (AM) samples were prepared by arc melting

under a protective Ar atmosphere. The melt-spinning (MS) samples were prepared using the as-cast tablets. The samples were induction melted under Ar atmosphere ($\approx 800$ mbar). By applying a pressure difference, the molten metal liquid is ejected through the nozzle onto the polished surface of the rotating Cu wheel. The as-prepared samples were sealed under Ar atmosphere in quartz ampoules, sintered and then quenched into water.

Powder diffraction patterns were collected in a PANalytical X-pert Pro diffractometer with Cu $K_\alpha$ radiation. The magnetic properties were measured in a Quantum Design SQUID (Superconducting Quantum Interference Device) magnetometer using the RSO mode in the low-temperature range (5 - 370 K).

## 7.3 Results and discussion

### 7.3.1 Effect of the fabrication method on the magnetisation

Different fabrication methods for $Ni_{48}Mn_{37}Sn_{15}$ samples are applied and compared. The sample name and its fabrication method with magnetisation and XRD information are summarised in Table 7.1.

***Table 7.1:*** Magnetisation and XRD information of different fabrication methods for $Ni_{48}Mn_{37}Sn_{15}$

| samples | Fabrication method | $T_c$* (K) | $M_{max}$* (Am$^2$/kg) | $|dM/dT|_{max}$* (Am$^2$/kgK) | FWHM ** (deg) |
|---------|--------------------|------------|------------------------|-------------------------------|----------------|
| SH1 | BM + AM | 321 | 40 | 0.5 | 0.694(7) |
| SH2 | BM + MS | 333 | 61 | 0.8 | 0.528(7) |
| SH3 | BM + ANN | 329 | 70 | 0.9 | 0.554(7) |
| SH4 | BM + MS +ANN | 332 | 72 | 1.0 | 0.443(7) |

\* The values are determined from M versus T curves under an external field $\mu_0 H = 1$ T.
\*\* The values are obtained from a fit for the (220) peak.

Figure 7.1(a) illustrates the temperature-dependent magnetisation in a magnetic field of $\mu_0 H = 1$ T for Heusler compounds synthesised by ball milling, melt spinning and annealing in comparison to gadolinium. From the graph and Table 7.1, it is clear that the Curie temperatures for both fabrication methods are in the desired working temperature range. The SH1 sample shows the lowest maximum magnetisation in an applied field of 1 T. The $|dM/dT|$ value (Table 7.1), the

derivative of the *M-T* curve, shows the sharpness of the transition. The SH3 and SH4 samples show almost the same trend in the temperature dependence of magnetisation and the |*dM/dT*| value is close to each other. The SH4 sample has the largest total magnetisation value and also the sharpest transition. The result for SH3 sample is comparable to the SH4 sample.

Figure 7.1(b) shows the X-ray pattern for $Ni_{48}Mn_{37}Sn_{15}$ synthesised by ball milling, melt spinning and annealing. The inset shows a comparison of the (220) peak for different fabrication methods. The XRD patterns show that the SH2 and SH4 samples show a lower impurity contribution, whereas, the SH1 and SH3 sample show a higher impurity content. According to the Scherrer equation[10], the increase in peak full width at half maximum (FWHM) is proportional to the mean size of the crystalline domain. The SH1 sample shows the widest peak among all the fabrication method ( see Table 7.1), which is an indication that the sample is not well crystallised. This correlates well with the lowest magnetisation value in *M-T* curves. For the other three fabrication methods, the FWHM is almost the same. The $L2_1$ Heusler phase is well-formed for all fabrication methods.
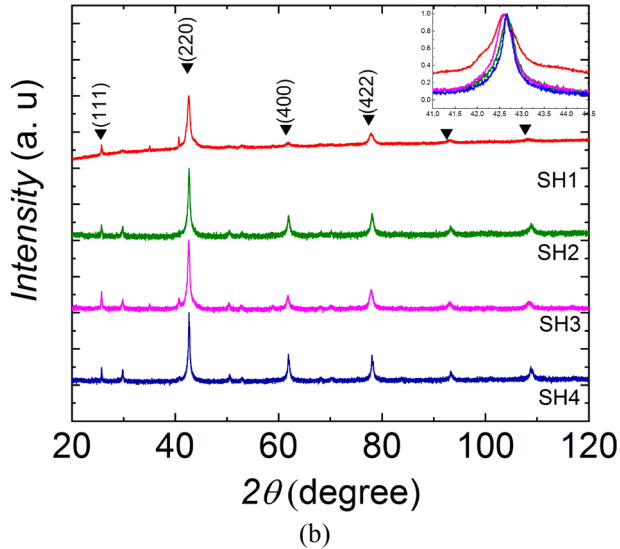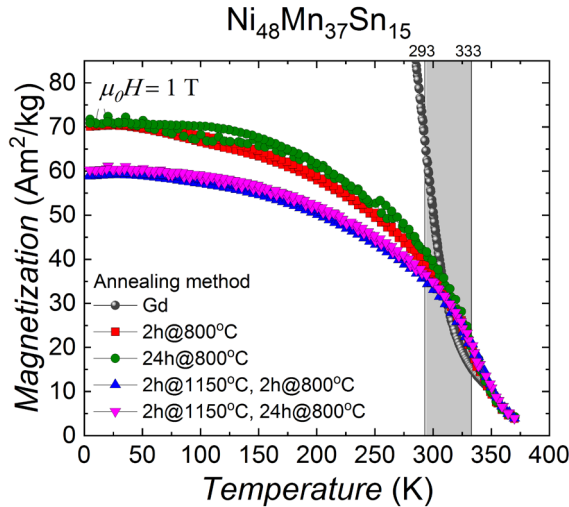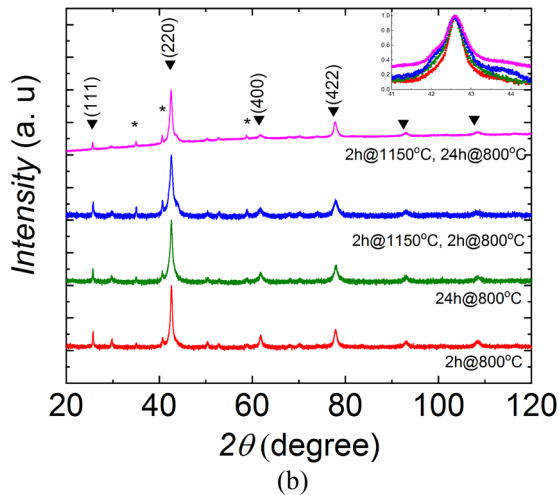


(a)

(b)
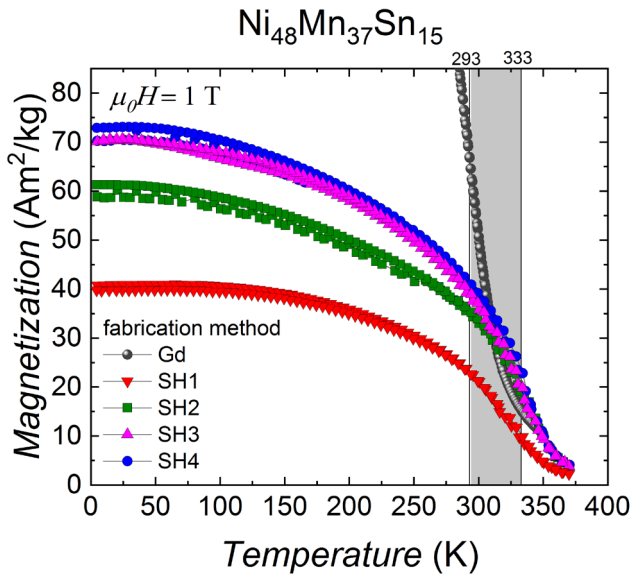
***Figure 7.1:*** (a) Temperature dependence of magnetisation of $Ni_{48}Mn_{37}Sn_{15}$ with different fabrication methods measured at $\mu_0 H = 1$ T. Gd is shown as a reference. The grey area is the suitable temperature range for the thermomagnetic motor (TMM). (b) X-ray powder diffraction pattern of $Ni_{48}Mn_{37}Sn_{15}$ the Heusler alloys with different fabrication methods collected at room temperature. The indexed peaks correspond to the *L2₁* Heusler phase. The * peaks correspond to the MnO phase. The inset shows the most significant (220) peak.

Based on the X-ray patterns, it is clear the best way to synthesis $Ni_{48}Mn_{37}Sn_{15}$ is the SH4 sample: which is ball milling, melt spinning followed by annealing. It results in the highest maximum magnetisation value and the lowest impurity phase. The SH3 sample, with ball milling and annealing, shows comparable results, but with a higher impurity fraction. For the energy-saving and sustainable aspect, the ball milling followed by annealing procedure (SH3) is chosen in the following.
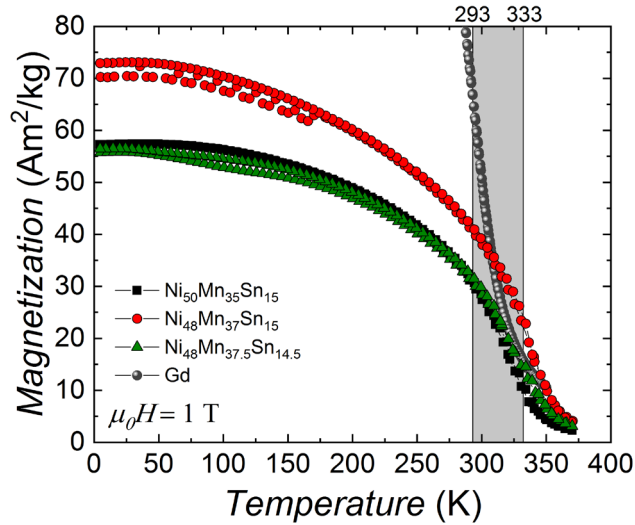
### 7.3.2 Effect of heat treatment on the magnetisation

$$Ni_{48}Mn_{37}Sn_{15}$$



(a)



(b)

***Figure 7.2:*** (a) Temperature dependence of magnetisation of $Ni_{48}Mn_{37}Sn_{15}$ with different heat treatments measured at $\mu_0H = 1$ T. Gd is shown as a reference. The grey area is the suitable temperature range for the thermomagnetic motor (TMM). (b) X-ray powder diffraction pattern of $Ni_{48}Mn_{37}Sn_{15}$ Heusler alloys with different heat treatments collected at room temperature. The indexed peaks correspond to the $L2_1$ Heusler phase[11, 12]. The * peaks correspond to the MnO phase. The inset shows the most significant peak (220)

We observed pronounced differences in the magnetisation curve by changing the annealing temperature and time (see Figure 7.2(a)). The most promising results with the largest magnetisation values were observed in the ball-milled sample, followed by annealing at 800°C for 2 and 24 hours. This observation is in a good agreement with the X-ray patterns. In the X-ray patterns (Figure 7.2(b)), the samples annealed at 800°C for 2 and 24 hours show a less impurity content. The sample annealed at 800°C for 2 hours has the lowest FWHM, which indicates it was nicely crystalised. The following samples will be heat treated at 800°C for 2 hours.

### 7.3.3 Methods to maximise the magnetisation

We started our investigation in $Ni_{50}Mn_{50-x}Sn_x$ alloys with $x = 15$, which showed the largest magnetisation value within this series [5]. Figure 7.3(a) illustrates the temperature-dependent magnetisation in a magnetic field of $\mu_0 H = 1$ T for Heusler compounds synthesised by ball milling annealed at 800°C for 2 hours. We synthesised $Ni_{50}Mn_{35}Sn_{15}$ samples with a Curie temperature of $T_C = 319$ K and a maximal magnetisation of $M = 57$ Am$^2$/kg at $\mu_0 H = 1$ T. By adjusting the Ni/Mn ratio we were able to increase the maximal magnetisation at 5 K by 28 % in $Ni_{48}Mn_{37}Sn_{15}$ to $M = 72$ Am$^2$/kg in an applied field of 1 T. Simultaneously, we observe an increase in the Curie temperature to $T_C = 332$ K, which is about 4 % higher compared to $Ni_{50}Mn_{35}Sn_{15}$. Adjusting the Mn/Sn ratio by replacing Sn by Mn shows a decrease in maximum magnetisation, which is a promising approach for TMM applications.

By replacing Ni with 5 % of Co, the magnetisation of $Ni_{43}Co_5Mn_{37}Sn_{15}$ reached a maximum of $M = 89$ Am$^2$/kg at $T = 5$ K in a magnetic field of $\mu_0 H = 1$ T (Figure 7.3(b)). In this sample the magnetic transition occurs at $T_C \approx 365$ K. By replacing Sn with 1 % of Al, the magnetisation of $Ni_{43}Co_5Mn_{37}Sn_{14}Al$ reached a maximum of $M = 102$ Am$^2$/kg at $T = 5$ K in a magnetic field of $\mu_0 H = 1$ T, while $T_C \approx 370$ K Figure 7.3(b). A precise determination of $T_C$ via the magnetisation measurements was not possible in this case, due to the limited operating range of the SQUID to a maximum temperature of $T = 370$ K.

**7**

(a)
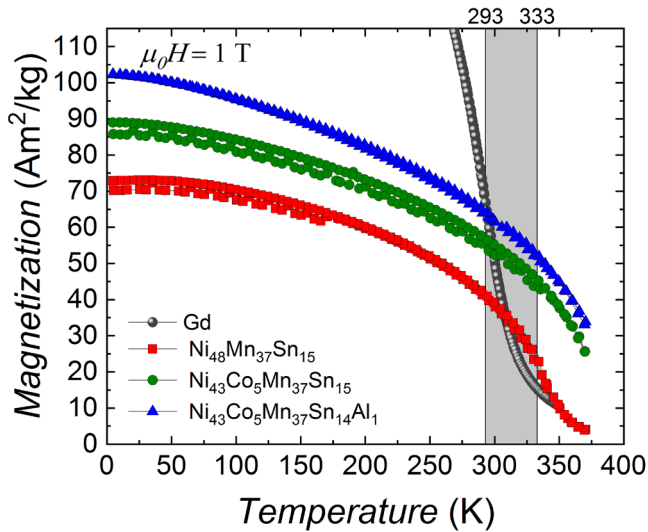


(b)

**Figure 7.3:** (a) Temperature dependence of magnetisation of $Ni_{48}Mn_{37+x}Sn_{15-x}$ measured at $\mu_0H = 1$ T. (b) Temperature dependence of magnetisation of $Ni_{48}Mn_{37}Sn_{15}$ with Co and Al as a substitution measured at $\mu_0H = 1$ T. Gd is shown as a reference. The grey area is the suitable temperature range for the thermomagnetic motor (TMM).

## 7.4 Conclusions

It has been shown that aside from the regular melt spinning or arc melting, ball milling is a possible way to synthesis Ni-Mn-Sn alloys. The advantage of ball milling is that the annealing time can be shortened. Based on the optimised sample fabrication, the maximum magnetisation can be tuned by adjusting the Ni:Mn, and the Mn:Sn ratios. The total magnetisation can be significantly improved by substituting Ni by cobalt (Co) or by substituting Sn by small amounts of aluminium (Al).

## References

1. Heusler, F.F.F., Verh DPG, 1903. **5**.
2. Graf, T., C. Felser, and S.S.P. Parkin, *Simple rules for the understanding of Heusler compounds.* Progress in Solid State Chemistry, 2011. **39**: p. 1-50.
3. *http://www.swiss-blue-energy.ch/.*
4. Kitanovski, A., et al., *Magnetocaloric Energy Conversion.* 2015: Springer International Publishing.
5. Liu, J., et al., *Giant magnetocaloric effect driven by structural transitions.* Nature Materials, 2012. **11**.
6. Trombi, L., et al., *Rapid microwave synthesis of magnetocaloric Ni–Mn–Sn Heusler compounds.* Scripta Materialia, 2020. **176**: p. 63-66.
7. Porcari, G., et al., *Influence of thermal conductivity on the dynamic response of magnetocaloric materials.* International Journal of Refrigeration, 2015. **59**: p. 29-36.
8. Uhl, E., *The ferromagnetic and paramagnetic properties of heusler alloys $(Ni_{1-x}Co_x)_2MnSn$.* Journal of Solid State Chemistry, 1982. **43**: p. 354-358.
9. Chen, J., et al., *The influence of Al substitution on the phase transitions and magnetocaloric effect in $Ni_{43}Mn_{46}Sn_{11-x}Al_x$ alloys.* Journal of Magnetism and Magnetic Materials, 2011. **323**: p. 248-251.
10. Patterson, A.L., *The Scherrer Formula for X-Ray Particle Size Determination.* Physical Review, 1939. **56**: p. 978-982.
11. Buschow, K.H.J., P.G. van Engen, and D.B. de Mooij, *Magnetic and Magneto-optical properties of Heusler alloys of the type $Ni_{3-x}Mn_xSn$.* Journal of Magnetism and Magnetic Materials, 1984. **40**: p. 339-347.

**7**

12. Helmholdt, R.B. and K.H.J. Buschow, *Crystallographic and magnetic structure of Ni₂MnSn and NiMn₂Sn.* Journal of the Less Common Metals, 1987. **128**: p. 167-171.

**7**

# CONCLUSION AND RECOMMENDATIONS

# 8

Truth seems to come with its final word; and the final word gives.

-Stray Birds by Rabindranath Tagore

真理仿佛带来了它的结论而来；而那结论却产生了它的第二个。

–泰戈尔《飞鸟集》

In the introduction (Chapter 1), the procedure of designing a proper magnetocaloric material (MCM) is described using a flow chart (Fig 1.4). This lead to four research questions:

**Question 1**: How to experimentally obtain a phase diagram and how to use the phase diagram to design a proper MCM for applications?

**Question 2**: How to classify the order of the magnetic phase transition. Is there any universal rule to classify, a first order magnetic phase transition (FOMT), a second-order magnetic phase transition (SOMT) and the critical point (CP) at the boundary?

**Question 3**: How does the structure change when the MCM crosses the magnetic transition? Does the charge show a redistribution when the sample crosses the transition?

**Question 4**: How to choose the best route to synthesis designed material? The synthesis route can be adjusted to the desired properties by changing the heat treatment, adjusting the elemental composition or by introducing a new element. In this thesis, some examples are given to demonstrate how do the optimisation procedure works.

In the following paragraphs, I will summarise my work by answering the questions above.

## 8.1 Conclusions

Magnetocaloric materials show great potential for utilisation in magnetic refrigeration and magnetic energy conversion. Some magnetocaloric effect (MCE) materials, such as Mn-Fe-P based, La-Fe-Si based, and Ni-Mn based materials, were widely studied for their giant MCE near room temperature.

In order to find suitable compositions for applications, the phase diagram of the $Mn_xFe_{2-x}P_{1-y}Si_y$ system was investigated in a wide range of compositions (for a Mn fraction of $0.3 \leq x \leq 2$ and a Si fraction of $0.33 \leq y \leq 0.60$). A large number of samples were synthesised, analysed and summarised in compositional diagrams for the relevant physical properties. In the phase diagram of $Mn_xFe_{2-x}P_{1-y}Si_y$ ($x = 0.3 - 2$ and $y = 0.33 - 0.60$), the highest transition temperature is found for high Fe and Si contents, while the lowest is found for low Fe and Si contents. The largest hysteresis was found when Fe:Mn = 1:1. Both Mn-rich and Fe-rich samples with a low Si concentration were found to show a low hysteresis, and can, therefore, form promising candidate materials for applications in a thermomagnetic motor. Based

on the desired working temperature range, contour lines can be drawn in the compositional diagram for $T_C$. These contour lines can then be duplicated at the same positions in the compositional diagram for the thermal hysteresis. With the preliminary information on $T_C$ and thermal hysteresis as a function of composition, a summarised graph can be drawn to estimate the optimal composition. Three samples ($Mn_{0.5}Fe_{1.5}P_{0.6}Si_{0.4}$, $Mn_{1.1}Fe_{0.9}P_{0.5}Si_{0.5}$, $Mn_{1.3}Fe_{0.7}P_{0.4}Si_{0.6}$) were prepared using the guidance of these diagrams. The results confirm that the transition temperature is in the desired range. The thermal hysteresis can be further optimised by optimising the stoichiometry. (*answer to question 1, details are presented in chapter 3*)

The currently used methods to classify FOMT and SOMT materials were applied and compared by studying a series of $Mn_{1.3}Fe_{0.7}P_{1-y}Si_y$ ($y$ = 0.4, 0.5 and 0.6) samples. The Si0.4 and Si0.5 samples clearly classify as FOMT samples. For the Si0.6 sample, different criteria give a different conclusion. From the latent heat, the Si0.6 sample is predicted to undergo a FOMT. From the XRD data and the field dependence of $T_C$, the Si0.6 sample is right on the CP. However, based on the Arrott plots, the gradual field dependence for the entropy change and the newly proposed field exponent $n$, the sample is a SOMT material (but in close proximity to the CP). (*answer to question 2, details are presented in chapter 4*)

The La(Fe, Si)₁₃ class of materials exhibits a giant MCE. When heating these materials above the ferromagnetic transition temperature, the cubic structure undergoes a volume change. The origin of the volume change is attributed to a change in the size of the magnetic moments across the transition. In this paper, the structural, magnetic and electronic properties of $LaFe_{11.8-b}Co_bSi_{1.2}$ ($b$ = 0.25, 0.69 and 1.13) compounds are studied. With increasing Co content, the material is tuned from a FOMT towards a SOMT, $T_C$ increases and the thermal hysteresis remains negligible. In the unit cell, the most remarkable change in bond length is between the *8b* and *96i* sites and for one of the bonds between two neighbouring *96i* sites. The negative thermal expansion correlates with an angle change in the orientation of the cage formed by the *96i* atoms within the cubic unit cell across the transition. In the electron density map, it is revealed how the *96i* cage rotates within the cubic primitive cell. The samples with a smaller Co content show a larger variation in the electron density compared to the Co-rich sample. (*answer to question 3, details are presented in chapter 6*)

**8**

Ni-Mn based materials are promising candidates for magnetic energy conversion applications, as they are made of non-toxic and earth-abundant materials with a tuneable transition temperature, have a sizeable magnetocaloric effect and demonstrate good mechanical behaviour. These materials are sensitive to the applied magnetic field and can be used in applications with small driving fields. The most widely used fabrication methods for Ni-Mn based Heusler alloys are arc melting, induction melting and melt spinning, followed by a long-time heat treatment to achieve product homogeneity. Aside from the regular melt spinning or arc melting, ball milling is a possible way to synthesise Ni-Mn-Sn alloys. The advantage of ball milling is that the annealing time can be shortened.

The heat treatment is a procedure to alloy and to homogenise materials. The optimal heat treatment is different for different compounds. The optimised heat treatment for $Fe_2P$ compounds is 1100 $^{\circ}$C for 25 hours, and for Ni-Mn based Heusler alloys is 800 °C for 2 hours. The main effect of optimised heat treatment is to reduce the amount of impurity phases. As a result, both $T_C$ and the order of the magnetic phase transition can be affected by heat treatment.

Introducing a new element can significantly change physical properties. Small amounts of cobalt (Co) and aluminium (Al) lead to a significant increase in the total magnetisation of Ni-Mn based Heusler alloys. The effect of V substitution for Fe is investigating in the $Mn_{0.7}Fe_{x-y}V_yP_{0.6}Si_{0.4}$ alloys. For an increasing V content the *a* axis expands and the *c* axis shrinks (together with the *c/a* ratio), whereas the unit-cell volume stays about the same. The ferromagnetic transition temperature $T_C$ decreases with an increasing V content. In the $Mn_{0.7}Fe_{1.18}V_{0.03}P_{0.6}Si_{0.4}$ compound, 93% of the saturation magnetisation at 5 K was reached in an applied magnetic field of 0.5 T, which makes this compound a promising candidate for low-field applications. (*answer to question 4, details are presented in chapter 2, 5 and 7*)
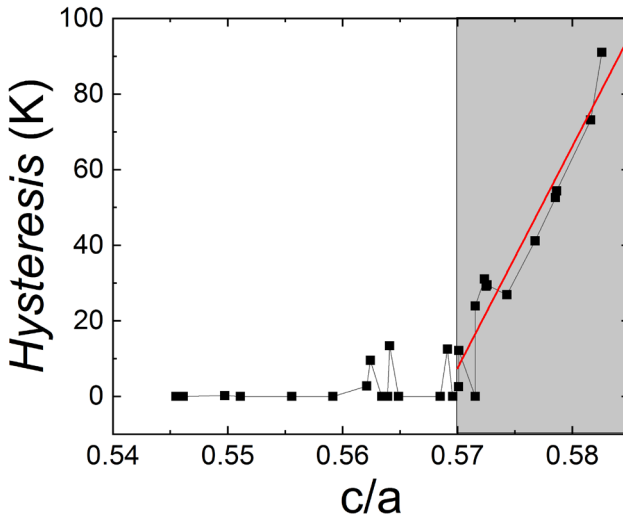
**8**

**Figure 8.1:** Thermal hysteresis as a function of *c/a* ratio of the lattice parameters for the Fe$_2$P type hexagonal main phase in the Mn$_x$Fe$_{2-x}$P$_{1-y}$Si$_y$ system. The red line is a linear fit to the experimental data.

## 8.2 Recommendations

### 8.2.1 The relationship between structure and hysteresis

When the thermal hysteresis is compared to the *c/a* ratio of the lattice parameters for the Fe$_2$P type hexagonal main phase of the Mn$_x$Fe$_{2-x}$P$_{1-y}$Si$_y$ system, a clear correlation is observed. As shown in Figure 8.1, the lowest *c/a* ratio starts from 0.5455 (Mn$_{0.5}$Fe$_{1.5}$P$_{0.4}$Si$_{0.6}$) and ends at 0.5826 (Mn$_{0.9}$Fe$_{1.1}$P$_{0.67}$Si$_{0.33}$). Most of the sample is a SOMT sample when *c/*a ratio is smaller than 0.57. For instance, sample Mn$_{1.5}$Fe$_{0.5}$P$_{0.6}$Si$_{0.4}$ is a SOMT sample without thermal hysteresis (*c/a* = 0.5696) and sample Mn$_{0.5}$Fe$_{1.5}$P$_{0.6}$Si$_{0.4}$ is also a SOMT sample with a 2.6 K thermal hysteresis (*c/a* = 0.5701). The hysteresis increases with an increasing *c/a* ratio in the grey region when *c/a* ratio is larger than 0.57. For instance, sample Mn$_{0.7}$Fe$_{1.3}$P$_{0.5}$Si$_{0.5}$ is a FOMT sample with a 12.13 K thermal hysteresis (*c/a* = 0.5701). The red line is a linear fit to the data.

In general, thermal hysteresis is controlled by the phase nucleation, which is a kinetic process, and the *c/a* ratio is a parameter of the crystal structure. The reason
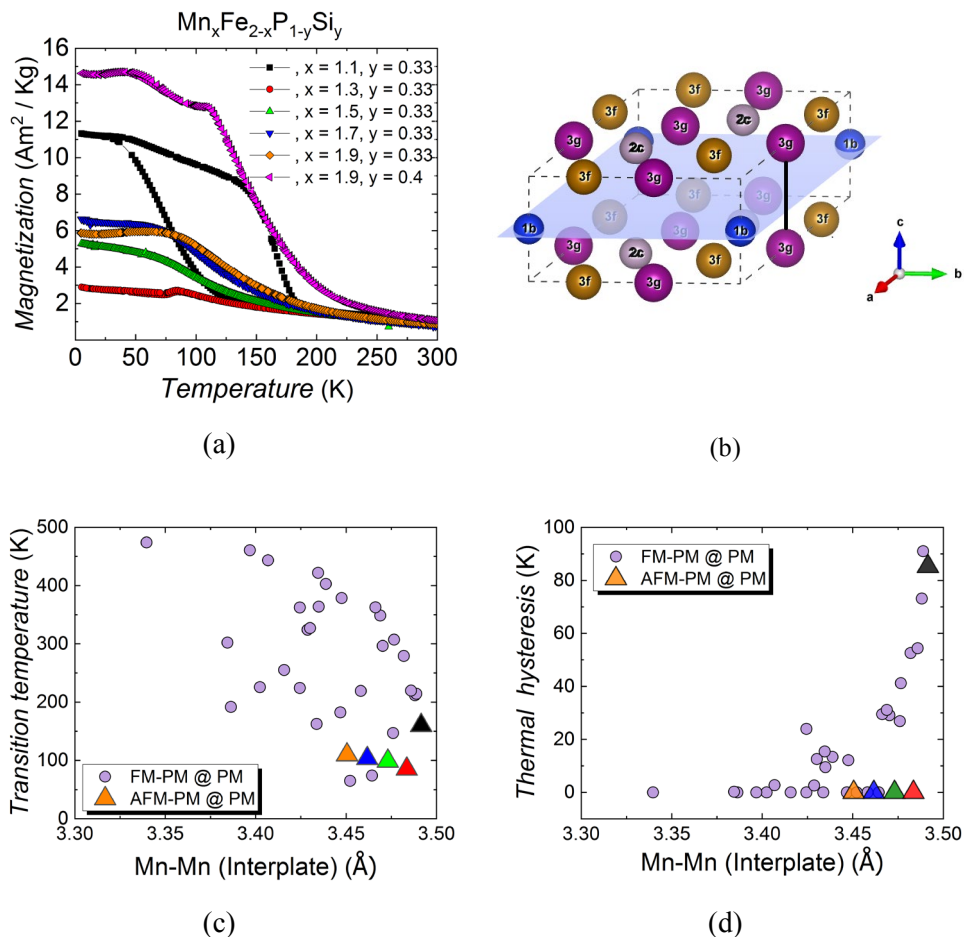
**8**

**Figure 8.2:** (a) Magnetisation as a function of temperature for $Mn_xFe_{2-x}P_{1-y}Si_y$ samples in the 'unstable' zone (measured in an applied magnetic field of 1 T). (b) Schematic diagram of the atomic structure for $(Mn,Fe)_2(P,Si)$ system with the unit cell. The transition temperature (c) and the thermal hysteresis (d) as a function of the distance between Mn and Mn atoms (interplain. The purple cycles indicate the ferromagnetic(FM) to paramagnetic (PM) transition (PM); the triangles indicate the antiferromagnetic (AFM) to paramagnetic (PM) phase transition. The colour code in the triangles in (c, d) is the same as in (a).

Why these two parameters correlated is not directly obvious. It could be that the hysteresis is related to the unit-cell distortion when the transition is crossed. This interesting experimental relationship between thermal hysteresis and the *c/a* ratio deserves further study.

### 8.2.2 Phase stability in the (Mn,Fe)$_2$(P,Si) quaternary system

In the phase diagram presented in chapter 3, there is an unstable area that mainly demonstrates an antiferromagnetic (AFM) to paramagnetic (PM) transition  In the phase diagram of transition temperature and thermal hysteresis (see Figure 3.4), it is clear that there is a boundary composition for the observation of the AFM to PM phase transition. This is illustrated in Figure 8.2 (a). The Mn atom has a preference to sit on *3g* site (Figure 8.2 (b) purple balls). The intraplane Mn-Mn distance can be calculated by the lattice parameter *a* and the internal coordinate of the Mn atom, which needs long time or high-resolution X-ray diffraction measurement. The interplane Mn-Mn distance (Figure 8.2(b) solid line) equals the lattice parameter *c*. The boundary compositions can be characterised by their unit-cell parameters. The transition temperature (see Figure 8.2 (c)) and the thermal hysteresis (see Figure 8.2 (d)) is investigated as a function of the distance between Mn and Mn atoms. There is no clear critical interplane Mn-Mn distance observed to distinguish the AFM-to-PM and FM-to-PM transitions, although the AFM to PM transition is only found beyond a minimum Mn-Mn distance of 3.45 Å. Therefore, it is useful to find a critical parameter that can be used to distinguish the appearance of these two types of magnetic phase transitions. More insight into the stability of the magnetic order will give a better understanding of the (Mn,Fe)$_2$(P,Si ) quaternary system.

### 8.2.3 Criterion to distinguish CP and SOMT

In chapter 4, the criteria to distinguish the nature of the phase transition were compared. The presence of a FOMT is usually clear. However, CP and SOMT are not always easy to distinguish. The desired MCMs should be positioned in the vicinity of the critical point, in order to show a large magnetisation change, a large entropy change and a small latent heat and no hysteresis. It would be a significant progress if an easy way to classify the phase transition could be found that does not require time consuming experiments.

**8**

### 8.2.4 Efficient composition selection

The practice to estimate the compositions with desired properties is based on references or on using phase diagrams. If we can apply new technology like machine learning, using data mining in the references from a database, I believe compositions with the desired properties can be selected more efficiently.

### 8.2.5 Explore new compounds

To find new improved functional materials is the dream of every material scientist. With the help of computer screening, we have a chance to mine the most promising candidates in a vast database of materials. With additional physical input from references and compositional optimisation, hopefully, we can find promising new materials other than the famous MCMs families listed in chapter 1.

8

# ACKNOWLEDGEMENTS

All happy families resemble one another; each PhD candidate is unhappy in its own way. I must admit that my PhD study is a tough time. During the first 30 years in my life, I stayed in the same city studying, working, falling in love and getting married. For the first time ever, I moved to a new city which is more than 10000 km away from my home town. As a former chemistry teacher working at a high school, I am currently working with a group of physicists. Besides, my family experienced a significant change. I lost my beloved grandfather and my father-in-law. Nevertheless, coronavirus is even a more formidable challenge not only for me but also for all people around the world. Needless to say, it is inconceivable to face these challenges alone. There are too many people I feel grateful for their help. Every experience I've had and every person I've met have all been imprinted in my life. When you read this dissertation, perhaps, some of you, this is the only part you want to read, to find out how I describe you. Here we go.

First and foremost, I would like to express gratitude to my supervisor and promoter, Prof. dr. Ekkes Brück, for having accepted me as a PhD candidate in the Fundamental Aspects of Materials and Energy (FAME) group, and for his excellent guidance on my PhD career. His door is always open to the student in need of help. Whenever I raise a "silly question", he always responds by saying "there is no silly question during research". Most importantly, he always guides me in the right way.

I feel genuinely appreciated for the guidance provided by my supervisor and promoter, Dr. ir. Niels van Dijk. Up to now, I am amazed by his remarkable expertise in solid-state physics and material science. He always provides me with insight into a science-related question, which cultivates a new-generation scientist. Thank you for guiding me towards the goal of becoming a better me. Without you, I would not have completed this dissertation. Thank you for instructing me to deduct formula and correcting my manuscript each time. I will preserve the manuscript you have corrected for life, which is a unique and unforgettable memory. I also appreciate you for translating the summary of my thesis into Dutch. It is also really pleasing to hear the funny and exotic stories about science and culture as shared with us.

with positive energy when I feel frustrated. He is also a good teacher willing to share his knowledge me. Bowei is the one who has always been sharing his knowledge with me unreservedly in the group meeting. My special thank goes to Yibole. It is really a pleasant time to share an office with you. You helped me a lot in both study and private life during my stay in the Netherlands. Thanks to Xuefei and Fengjiao, as you are always so warm-hearted organize parties in Delft and Nanjing. You are appreciated for the help in refinement and every aspect. Thanks to Jiawei Lai, everything is beyond words. I am also thankful to all the colleagues (or former colleagues) in the FAME group including, Lian Zhang, Luana Caron, Dũng, Dimitrios Bessas, Thang, Jose, Zhiqiang Ou, Dung, Maurits Boeije, Ivan Batashev, Jun Liu, Hamutu, Shen Qi, Fengqi Zhang, Anika Kiecana,

It is delightful to spend the lunchtime with all my Chinese colleagues in RID. My thanks go to Bei and Yifan as my best friends in RID. It is genuinely pleasant to conduct a (non)work-related discussion. I also feel especially appreciated to Yifan for helping me with the SEM experiment. My thanks also go to Zhaolong. Although you are rare to speak out, you really helped me a lot with work. My gratitude is extended to Beien, who is always passionate about making and sharing delicious food. I also appreciate Huanhuan for taking a positive attitude and filling our lives with laughter. It is so lovely to travel with you to east Europe. Yuanyuan, I truly admire you for your calmness and elegance. Apart from the people above, I would also like to acknowledge Zhouzhou, Haixing Fang, Tiantian, Wenqin, Guorui Zheng, Ming Liu, with whom I spent a lovely lunchtime with.

Needless to say, my favourite Dutch social activities are coffee break and Birthday cake. It is terrific talking to each other from different culture backgrounds. Violetta, your laughter has the power to dispel clouds. Ankit, it is a pleasant journey to attend the summer school with you. Lars, thanks for your advice and comments on every single aspect (I mean fashion and style). Besides, I would like to thank all PhD or postdoc fellows at the RID: Evgenii Velichko, Alexandros Vasileiadis, Eveline van de Maas, Hanan Al-Kutubi, Jurrian Bakker, Maxim Ariëns, Remco van der Jagt, Tammo Schwietert, Tomas Verhallen, with whom I have spent excellent coffee time with.

My dearest Chinese friends in the Netherlands always fill my life with laughter and pleasure. My special thanks go to Shan and Ulaş (sorry Ulaş, to classify you in my Chinese friend). We started our PhD almost at the same time. We shared our happiness sadness, and loneliness. Thanks also to Xue, we three encouraged each

other to move forward. I feel like being blessed by knowing you. It is unlikely for me to survive the first year of study without your support. I am also immensely grateful to Shan for helping me with coding. By the way, I am looking forward to your Qu talk! Sorry, Ulaş we always forget to say English when we hang out. In the future, we can try to speak Dutch together. I also need to thank Jiao and Fei. We became the best friend after knowing each other in ACSSNL. Thank you for inviting us during every Chinese festival like the Spring festival and Drogen boat festival, which allows me to develop so many noodle-making skills that make me feel like I was a local in Shaanxi. Thanks to Ding as well. We have plenty of nice time playing mahjong and Guandan together. Thanks to Hong and Dongbin for hiking and inviting me to their place. I also thank Dong for taking care of photography during my defence. Thanks to Xiuxiu, despite that we have known each other for just months. We performed many activities together, such as basketball and e-game. My thanks also go to Tian, Coach Chang and Yun, Boling, Meng Wang for hanging out together. We shared a lot of fun time. Thanks to Xiang for regarding me from time to time and helping me improve my skills required to find employment. Thanks to three ladies in the margarita club (Anna, Rui, Yuanyuan), as we always find shared interest in the group. It is so enjoyable talking to you. My special thanks go to Yuanyuan. It is such a wonderful experience to meet a high school classmate 10000 Km away from hometown. Thank you for always thinking of me at the time of traditional Chinese festivals. Thanks to Lisa and Maomao. It is nice to discuss the start-up plan with you.

It is my honour to join the Association of Chinese students and scholars (ACSSNL) in the Netherlands. I am extremely grateful to the Chinese Embassy in the Netherlands for inviting me to participate in the New Year receptions and other beautiful events. Thanks to ACSSNL, which made me familiar with many Chinese fellows, including Meng Wang, Jiakun Gong, Jiao and Fei. As the deputy leader of ACSSNL-Delft branch between 2016 and 2017, thanks to Ding Ding, the leader of ACSSNL, it is enjoyable to collaborate with you. Thanks to my Chinese fellows including Pingping Wen (finally I remember your name), Mingzhao, Yuying, Yishan, Hai Gong, Zhi Hong, Zongchen Li, Bing Huang, and Zhizheng Wangand for our memorable experience in organizing various events.

It is also an incredible journey at the Chinese School Delft, where I met up with so many lovely people. Thanks to the headmaster Hongyan Wang and Teacher Pang. You both set a moral model for me. Besides, thank you for the support in Chinese

teaching and the valuable advice offered. Thanks to Wei Huang for your heart-warming home town accent and passionate dancing training. Thanks to Xiaoling Wang and Junru Wu for organizing various hotpot parties and also for referring me to a job. Despite some difficulties encountered in our first project, I have faith that we will have a chance to collaboration one day in the future. Thanks to Hui Qi and Lao Xu for the most delicious Chinese dishes and BBQ.

Thanks to the book reading club, and to Yuan Qiu for organizing this club. Thanks also to Hui Shen for your encouraging words that made me gain self-confidence. Thanks for all the members in the booking reading club, including Yan Yan, Hui Shen, Zhuoyu Wang, etc. I take enjoyment from reading and sharing books with you guys. Inspired by you, I start to organize a PhD booking reading club. Thanks to you guys again.

My thanks also go to all the members of HeFeng Media. I appreciate Taoping Wan and Old Ye for your advice and the Mantou you made. Thanks to Xin Li, Old Tian and my little Dutch teacher for sharing the experience of food delivery, Tian's talk show and also the correction of my Dutch. Thanks to Kan Ji and Teacher Wang as well. I was always amazed by your beautiful words. It is so inspiring to watch you guys working together.

I would also like to extend my sincere gratitude to my former teacher, Prof. dr. Zhigang Zhao at Nanjing Tech University for his constant support. Thanks to the Nanjing Tech University alumni Association for your support amid the COVID-19 pandemic.

I want to thank all of my old friends in China for your unconditional support at all times. Thanks to Derong Ning for supporting us in such an exceptional circumstance. Thanks to Yu Wang and Siwen Gu. It is always nice talking to you even on the phone. Thanks also to Guoguo and Old Dai for treating me as a family member.

Thanks to my lovely neighbours, and to Shana for teaching me one Dutch word each time we meet. Thanks also to Ton, my language buddy, for your patient explanation on Dutch language and encouragement.

Last but not least, I would like to express my heartfelt gratitude to my parents and parents-in-law for their selfless love and support. Thanks also to my husband Qian for your tolerance of my bad temper, patience and faith in me.

# LIST OF PUBLICATIONS

12. **X. You**, M. Maschek, J. Lai, J. Liu, B. Huang, N.H. van Dijk and E. Brück, *First and Second-Order Phase Transitions in (Mn,Fe)$_2$(P,Si) alloys,* in preparation.

11. **X. You**, M. Maschek, J. Lai, J. Liu, B. Huang, N.H. van Dijk and E. Brück, *Phase Diagram of the Mn$_x$Fe$_{2-x}$P$_{1-y}$Si$_y$ system,* in preparation.

10. **X. You**, M. Maschek, M.F.J. Boeije, D. Chernyshov, A Barcza, N.H. van Dijk and E. Brück, *Synchrotron X-ray diffraction on the charge distribution in La(Fe,Co,Si)$_{13}$ compounds,* in preparation.

9. J. Liu, Y. You, I. Batashev, Y. Gong, **X. You**, B. Huang, F. Zhang, X.F. Miao, F, Xu, N.H. van Dijk and E. Brück, *Design of Reversible Low-Field Magnetocaloric Effect at Room Temperature in Hexagonal MnMX Ferromagnets.* Physical Review Applied, 2020. 13: p. 054003.

8. J. Lai, **X. You**, I. Dugulan, B. Huang, J. Liu, M. Maschek, L. van Eijck, N.H. van Dijk and E. Brück, *Tuning the magneto-elastic transition of (Mn,Fe,V)$_2$(P,Si) alloys to low magnetic field applications.* Journal of Alloys and Compounds, 2020. 821: p. 153451.

7. J. Liu, **X. You**, B. Huang, I. Batashev, M. Maschek, Y. Gong, F. Xu, N.H. van Dijk and E. Brück, *Reversible low-field magnetocaloric effect in Ni-Mn-In-based Heusler alloys.* Physical Review Materials, 2019. 3(8): p. 084409.

6. J. Liu, Y. You, Y. Gong, **X. You**, B. Huang, X.F. Miao, G. Xu, F, Xu, E. Brück, *Giant reversible magnetocaloric effect in MnNiGe-based materials: Minimizing thermal hysteresis via crystallographic compatibility modulation.* Acta Materialia, 2019. 174: p. 450-458.

5. J. Lai, B. Huang, X.F. Miao, N. van Thang, **X. You**, M. Maschek, L. van Eijck, D. Zeng, N.H. van Dijk and E. Brück, *Combined effect of annealing temperature and vanadium substitution for mangetocaloric Mn$_{1.2-x}$V$_x$Fe$_{0.75}$P$_{0.5}$Si$_{0.5}$ alloys.* Journal of Alloys and Compounds, 2019. 803: p. 671-677.

4. M. Maschek, **X. You**, M.F.J. Boeije, D. Chernyshov, N.H. van Dijk and E. Brück, *Charge redistribution and the magnetoelastic transition across the first-order magnetic transition in (Mn,Fe)$_2$(P,Si,B).* Physical Review B, 2018. 98.

3. J. Lai, B. Huang, D. Bessas, **X. You**, M. Maschek, D. Zeng, L. Zhang, L. N.H. van Dijk and E. Brück, *Ultra-low Hysteresis in Giant Magnetocaloric Mn$_{1-x}$V$_x$Fe(P, Si,B)* Compounds. arXiv preprint arXiv:1810.09902, 2018.

2. E. Xu, H. Li, **X. You,** C. Ma, L. Zhang, Q. Wang, Z. Zhao, *Influence of micro-amount O$_2$ or N$_2$ on the hydrogenation/dehydrogenation kinetics of hydrogen-storage material MgH$_2$.* International Journal of Hydrogen Energy, 2017. 42(12): p. 8057-8062.

1. Y. Zhu, **X. You,** J. Ren, Z. Zhao, L. Ge, *Self-healing polyelectrolyte multilayered coating for anticorrosion on carbon paper.* J Colloid Interface Sci, 2017. 493: p. 342-348.

# INTERNATIONAL ACTIVITIES

7. Synchrotron X-ray diffraction on the charge distribution in La(Fe,Co,Si)$_{13}$ compounds, Delft Days on magnetocalorics, 2019, Delft, Netherlands *(Invited talk)*

6. Guidance of Synthesis (Mn, Fe)$_2$ (P, Si)$_1$ Sample, Physics at Veldhoven, 2019, Veldhoven, Netherlands *(Oral presentation)*

5. The phase diagram of Mn$_x$Fe$_{2-x}$P$_{1-y}$Si$_y$, Thermag VIII, 2018, Darmstadt, Germany *(Poster presentation)*

4. Structure, magnetism of Mn$_x$Fe$_{2-x}$P$_{0.6}$Si$_{0.4}$ compounds, 9$^{th}$ Joint European Magnetic Symposia (JEMS), 2018, Mainz, Germany *(Oral presentation)*

3. The partial phase diagram of Mn$_x$Fe$_{2-x}$P$_{1-y}$Si$_y$, 21$^{st}$ International Conference on Magnetism (ICM), 2018, San Francisco, USA *(Oral presentation)*

2. Phase diagram of (Mn,Fe)$_2$(P,Si)$_1$ system for thermomagnetic motor, Structure and Magnetism of Mn$_x$Fe$_{2-x}$P$_{2/3}$Si$_{1/3}$ Compounds, Materials Research Society 2018 Spring meeting, 2018, Phoenix, USA *(Oral presentation)*

1. The phase diagram of hexagonal Fe$_2$P-type materials, Danish Days on Caloric Materials and Devices, 2017, Risø, Denmark *(Poster presentation)*

# Curriculum Vitæ

## You, Xinmin
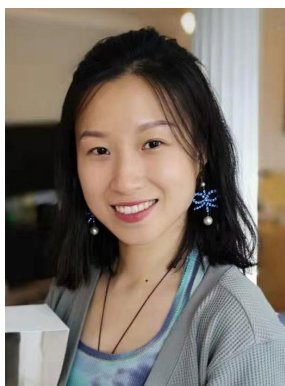
Xinmin was born on 17 October 1982 in Nanjing, Jiangsu, China. After attaining her bachelor's degree in education, she spent 5 years working as a chemistry teacher at a high school. She is keen on confronting challenges. She achieved her second bachelor degree in integrated Chinese and western medicine at the Nanjing University of Chinese Medicine.

Back in 2009, she attended Nanjing Tech University as a postgraduate student and majored in Material Science and Engineering. Her interests in renewable energy are reflected in the subject of her research report. She conducted a study on hydrogen fuel cell while undertaking her master project. She also took enjoyment from the learning of new techniques in relation to renewable energy and was a part-time inquire engineer who issued originality statement.

Her ambition is to put the technology into practical applications and finally commercialize it. After graduation, she joined the Jiangsu provincial hydrogen Fuel Cell R&D centre, where she was able to apply her knowledge in practice. She applied and established new project centres in different cities.

In 2015, she embarked on her study for PhD at the Reactor Insititute Delft under the supervision of Ekkes Brück and Niels van Dijk, where she learned about renewable energy-related magnetocaloric materials. A variety of experimental techniques were applied to improve the understanding of the magnetocaloric compounds. She conducted research on the material families NiMnSn, $La(Fe,Si)_{13}$, and $(Mn,Fe)_2(P,Si)$ system. In the meantime, she paid particular attention to the practical applications and created phase diagrams as guidance for experimentation. The results of this research are presented in the thesis entitled "Design of efficient magnetocaloric materials for energy conversion".